8-11-2017

# Investigation and Mitigation of Anode and Cathode Impurities to Improve Polymer Electrolyte Fuel Cell Performance

Mehmet Ozan Ozdemir
*University of Connecticut*, mehmet.vzdemir@uconn.edu

# Investigation and Mitigation of Anode and Cathode Impurities to Improve Polymer Electrolyte Fuel Cell Performance

Mehmet Ozan Ozdemir, PhD

University of Connecticut, 2017

Due to an increasing demand for environment-friendly power production, polymer electrolyte fuel cells (PEFCs) are promising devices with their low operation temperature, zero-emission, high efficiency and smaller sizes. However, some challenges still exist in commercial applications. One of the issues is impurities in hydrogen (anode fuel) and air (cathode oxidant).

The first objective of this thesis is to investigate the carbon monoxide (CO) poisoning and a mitigation method of high-level CO (1,000 and 10,000 ppm) in a platinum (Pt) catalyst layer using hydrogen ($H_2$)/CO mixture as the inlet fuel. A one-dimensional transient model is developed including the species diffusion, the conservation of adsorbed species, and ionic and electronic charges. Oscillations in overpotential and coverage of adsorbed species are observed for 1,000 ppm CO level, while they are not detected for 10,000 ppm CO. Hence, behavior of oscillations throughout the catalyst layer thickness, and the reasons are explored for the lower concentration case. For 10,000 ppm CO, current density is pulsed from 0.1 to 2.5 A/cm$^2$ for the CO removal from Pt sites. It is concluded that up to 92% of CO within the catalyst layer can be removed, and 70% of the catalyst layer length is CO-free following the current pulsing.

In addition to CO poisoning, regular cleaning of pipeline and hardware is also significant in fuel cell operation to avoid the corrosion of components. An experimental and analytical study is implemented to select the appropriate cleaning agents in PEFCs.

Screening tests for several cleansers are performed during the injection of samples into the cathode inlet. One proper agent has shown a fully recoverable and minimal effect on the performance and as such is determined as the best candidate. PEFC can still operate at ~0.4 V at constant current (1 $A/cm^2$) even with a considerable flow rate (250 µl/min) of the selected cleanser. Detailed analysis of this cleanser is provided by curve fitting the electrochemical impedance spectroscopy data, and evaluation of binary gas diffusion coefficients. It is indicated that performance loss during sample exposure is mainly due to its adsorption on active Pt sites and increase in mass transfer resistance.

# Investigation and Mitigation of Anode and Cathode Impurities to Improve Polymer Electrolyte Fuel Cell Performance

Mehmet Ozan Ozdemir

B.S., Middle East Technical University, 2007

M.S, Middle East Technical University, 2009

A Dissertation

Submitted in Partial Fulfillment of the

Requirements for the Degree of

Doctor of Philosophy

at the

University of Connecticut

2017

**APPROVAL PAGE**

Doctor of Philosophy Dissertation

**Investigation and Mitigation of Anode and Cathode Impurities to Improve Polymer Electrolyte Fuel Cell Performance**

Presented by

Mehmet Ozan Ozdemir, M.S.

Major Advisor_____

Dr. Ugur Pasaogullari

Associate Advisor_____

Dr. Trent Molter

Associate Advisor_____

Dr. Prabhakar Singh

Associate Advisor_____

Dr. Michael T. Pettes

Associate Advisor_____

Dr. Mustafa F. Serincan

University of Connecticut

2017

To my parents and my lovely wife

# Acknowledgments

I would like to thank my supervisor, Dr. Ugur Pasaogullari, for his support, useful recommendations and comments during my PhD education. I am very grateful to him for encouraging me to finish my studies successfully. I would also like to appreciate the guidance from my committee members and associate advisors, Dr. Trent Molter, Dr. Prabhakar Singh, Dr. Michael Pettes and Dr. Mustafa Fazil Serincan.

I wish to thank Dr. Brice Cassenti, Mr. Leonard Bonville and Mr. William Collins for their technical suggestions about the projects and experiments. In addition, I am very fortunate to be a part of a great team during my PhD. Thanks to my colleagues and group members: Dr. Richard Fu, Dr. Phillip Baker, Dr. Xiaofeng Wang, Dr. Jaehyung Park, Dr. Md. Aman Uddin, Dr. Selvarani Ganesan, Dr. Jing Qi, Harsha Mallipalli, Christian Julian Ayala, Joshua Preston, Charles Banas and Eric Leamon for their helpful discussions and moral supports.

I extend my gratitude to the staff members in Center for Clean Energy Engineering: Terry Barber-Tournaud, Sheila Ciccone, Amy Smith, Peter Menard, Garry Barnes and Mark Biron for their administrative and technical support.

I would like to acknowledge the financial support of US Department of Energy. I would also like to express my gratitude to Dr. Daniel Hussey for his help during the experiments in NIST Center for Neutron Research.

I specifically thank my best friend and another PhD candidate, Huseyin Yer, for helping me in all circumstances. His strong support and suggestions constituted a path for

me to successfully perform my research studies. I sincerely wish him best of luck and success for his life and career in the future.

During my PhD, I had the chance to make great friendships. I need to express my appreciation to my friends, Dr. Altug Poyraz, Dr. Ozgur Oksuz and Ahmet Cevdet Cirkin, for giving me patience and moral strength. Furthermore, I feel very grateful to all people I met at UConn or in Storrs for motivating me.

I would also like to thank my parents for supporting and encouraging me all the time. I feel very fortunate to be motivated by my parents whenever I need strength and determination.

Lastly, I would like to express my gratitude and love to my precious wife, Samantha, for being a part of my life. It would have been very difficult for me without her love and continuous support.

# Table of Contents

# Nomenclature

| | |
|---|---|
| $A_v$ | Specific electroactive area of catalyst layer (CL), [$m^{-1}$] |
| $C_j$ | Concentration of species j; j: Carbon monoxide (CO), Hydrogen ($H_2$), or Water vapor (w) [$mol.m^{-3}$] |
| CL | Catalyst Layer |
| CO | Carbon monoxide |
| $CO_2$ | Carbon dioxide |
| $C_t$ | Molar area density of catalyst layer per $m^2$ platinum surface, [$mol.m^{-2}$] |
| $D_{AB}$ | Binary diffusion coefficient for the mixture of gas species A and B, [$cm^2.s^{-1}$] |
| $D_j^{eff}$ | Effective diffusion coefficient of species j; j: Carbon monoxide (CO) or Hydrogen ($H_2$), [$m^2.s^{-1}$] |
| $D_{j,o}$ | Standard (at reference temperature and pressure) diffusion coefficient of species j; j: Carbon monoxide (CO) or Hydrogen ($H_2$), [$m^2.s^{-1}$] |
| $E_{cell}$ | Actual fuel cell voltage, [V] |
| $E^0$ | Equilibrium cell voltage, [V] |
| $E_{th}$ | Maximum thermal cell voltage, [V] |
| $e^-$ | Electron |
| F | Faraday's constant, 96,485 [$A.s.mol^{-1}$] |
| G | Gibbs free energy, [$kJ.mol^{-1}$] |
| GDL | Gas Diffusion Layer |
| H | Enthalpy, [$kJ.mol^{-1}$] |
| $H^+$ | Proton |
| $H_2$ | Hydrogen |
| $H_2O$ | Water |
| i | Current, [A] |
| J | Current density, [$A.m^{-2}$] |
| $k_{h,a}$ | Rate constant of hydrogen adsorption over platinum times 2F, [$A.m^{-2}.atm^{-1}$] |
| $k_{co,a}$ | Rate constant of carbon monoxide adsorption over platinum times F, [$A.m^{-2}.atm^{-1}$] |
| $k_{w,a}$ | Rate constant of hydroxyl adsorption over platinum times F, [$A.m^{-2}$] |
| $k_{h,d}$ | Hydrogen desorption equilibrium constant, [atm] |
| $k_{co,d}$ | Carbon monoxide desorption equilibrium constant, [atm] |

| | |
|---|---|
| $k_{w,d}$ | Rate constant of hydroxyl desorption over platinum times F, [$A.m^{-2}$] |
| $k_{h,ox}$ | Rate constant of hydrogen electro-oxidation, [$A.m^{-2}$] |
| $k_{co,ox}$ | Rate constant of carbon monoxide electro-oxidation, [$A.m^{-2}$] |
| $l_c$ | Length of the catalyst layer, [m] |
| M | Molecular weight, [$g.mol^{-1}$] |
| $m_{pt}$ | Platinum loading of the catalyst layer, [$mg.cm^{-2}$] |
| n | Number of electrons |
| OH | Hydroxyl ion/molecule |
| $P_a$ | Anode pressure, [atm] |
| $P_c$ | Critical Pressure, [atm] |
| $P_{cathode}$ | Total pressure at cathode, [atm] |
| PEM | Polymer Electrolyte Membrane |
| $P_{ref}$ | Reference pressure, [atm] |
| $P_{sat}$ | Saturation pressure at cell temperature (T), [atm] |
| Q | Constant phase element due to the double layer capacity through the porous structure of electrodes, [$F/cm^2.s^{(a-1)}$ Pt], where a is an empirical constant ($0 < a < 1$) |
| $Q_{des}$ | Charge density required for atomic hydrogen desorption, [$mC.cm^{-2}$ Pt] |
| $Q_{des, ref}$ | Reference charge density required to remove a monolayer of proton on Pt, 0.21 $mC.cm^{-2}$ Pt |
| R | Resistance, [$\Omega.cm^2$] |
| $R_u$ | Universal gas constant, 8.314 [$J.mol^{-1}.K^{-1}$] |
| $r_{j,a}$ | Net adsorption rate of species, j, over platinum; j: Carbon monoxide (CO), Hydrogen ($H_2$) or Hydroxyl (OH), [$A.m^{-2}$] |
| $r_{j,ox}$ | Net electro-oxidation rate of species, j; j: Carbon monoxide (CO) or Hydrogen ($H_2$), [$A.m^{-2}$] |
| S | Specific gravity of naphtha at 16 °C |
| t | Time, [s] |
| T | Cell temperature, [K] |
| $T_b$ | Average boiling point of naphtha, [K] |
| $T_c$ | Critical temperature, [K] |
| $T_{ref}$ | Reference temperature, [K] |
| $V_i$ | Ionic phase potential within catalyst layer, [V] |

| | |
|---|---|
| $V_s$ | Solid phase (Electronic) potential within catalyst layer, [V] |
| w | Water vapor |
| x | Through-plane coordinate across the length of the catalyst layer, [m] |
| X | A physical property of naphtha |
| $y_{w,i}$ | Molar fraction of water vapor at the inlet |
| $y_{CO,i}$ | Molar fraction of carbon monoxide at the inlet, [ppm] |
| Z | Impedance, [$\Omega.cm^2$] |
| Z' | Real component of impedance data, [$\Omega.cm^2$] |
| Z'' | Imaginary component of impedance data, [$\Omega.cm^2$] |
| $\Delta H$ | Enthalpy difference for an electrochemical reaction, [$kJ.mol^{-1}$] |
| $\Delta G$ | Gibbs free energy difference for an electrochemical reaction, [$kJ.mol^{-1}$] |
| $\Delta G_f$ | Gibbs free energy of formation, [$kJ.mol^{-1}$] |
| $\Delta H_f$ | Enthalpy of formation, [$kJ.mol^{-1}$] |
| $\Delta S$ | Entropy difference, [$J.K^{-1}$] |
| $\alpha$ | Transfer coefficient |
| $\beta$ | Fuel cell efficiency |
| $\varepsilon_c$ | Porosity of catalyst layer |
| $\gamma$ | Catalyst layer surface roughness factor |
| $\phi_a$ | Relative humidity at the anode inlet |
| $\eta_a$ | Anode overpotential, [V] |
| $\theta_j$ | Surface coverages of adsorbed species j; j: Carbon monoxide (CO), Hydrogen ($H_2$) or Hydroxyl (OH) |
| $\sigma_s^{eff}$ | Effective electronic (solid phase) conductivity of catalyst layer, [$S.m^{-1}$] |
| $\sigma_i^{eff}$ | Effective ionic phase conductivity of catalyst layer, [$S.m^{-1}$] |
| $\eta_a$ | Activation overpotential loss, [V] |
| $\eta_m$ | Concentration (mass transfer) overpotential loss, [V] |
| $\eta_{ohmic}$ | Ohmic overpotential loss, [V] |
| $\eta_x$ | Mixed overpotential losses, [V] |
| $\xi$ | Fuel utilization factor |

# Chapter 1 Introduction

## 1.1 Brief overview of fuel cells

There is an increasing demand for alternative sources of energy in the world due to the large growth of industry and population, and limited availability of fossil fuels. U.S. Energy Information Administration predicts up to 11% increase in total energy consumption from 2016 to 2040 in the USA [1]. Transportation has a significant share in US energy consumption, and petroleum is the main source of energy in transportation. Although 91.5% of transportation-related energy demand is obtained from petroleum, 24% of US petroleum consumption is imported from other countries [2]. In addition, oil and natural gas prices are forecasted to increase in the near- and long-term projections [1].

Natural gas, petroleum, coal and the traditional methods for energy production (e.g. internal combustion engines) suffer high greenhouse gas emissions and lower energy efficiencies. According to US Department of Energy, about half of Americans live in areas where level of air pollution is critical to the environment and public health [3]. For instance, total carbon dioxide ($CO_2$) emission throughout the USA is reported to be 5.5 billion metric tons in 2015, and 41% of this value is caused by the oil consumption [2].

Due to issues mentioned above, renewable energy sources have been the main focus of research for nearly two centuries. Among different energy sources, fuel cells are one of the most promising devices since they have higher power efficiency, very low emission, no moving parts, easy refueling mechanism and potential for high power (>1 MW) generation [4]. Furthermore, fuel cell operation is not limited by Carnot cycle efficiency.

While internal combustion engines generate electricity with 30-40% efficiency, fuel cell power plants can reach up to 60-70% efficiency with cogeneration.

Fuel cells convert chemical energy of a fuel into electricity via electrochemical reactions, just like a battery. Unlike batteries, it does not need to be recharged since electricity is continuously produced as long as the fuel and oxidant are provided. Hydrogen, or a hydrogen-rich fluid, flows as a fuel through anode inlet. Oxygen, or air, is provided through cathode inlet. Fuel is dissociated into protons and electrons at the anode electrode. As the electrons are transferred to the cathode side through an external circuit, positively or negatively charged ions are transported from one electrode to another through an electrolyte. After a series of electrochemical reactions, electricity is generated and some byproducts, such as heat, water or carbon dioxide ($CO_2$), are produced.

Fuel cells are commonly used for the energy production in portable, stationary and transport applications. In some cases, they are also considered for both heat and power generation, e.g. heating of residential areas or the operation of combined heat and power (CHP) plants [5,6]. There are different types of fuel cells, significantly classified based on their electrolytes. Polymer electrolyte fuel cells (PEFC), alkaline fuel cells (AFC), phosphoric acid fuel cells (PAFC), molten carbonate fuel cells (MCFC) and solid oxide fuel cells (SOFC) are the most popular ones. Table 1.1 lists those along with their electrolytes, charge carriers, operating temperatures, applications and advantages.

**1.2 History of fuel cells** [7,8]

The origins of fuel cells come from the beginning of $19^{th}$ century with William Nicholson and Anthony Carlisle, who invented the water electrolysis (decomposition of water into

hydrogen and oxygen using electricity) [9]. William R. Grove revealed first basics of hydrogen fuel cells, named as “Grove cell”, in 1838. He observed the current flow after he immersed two platinum (Pt) electrodes on their one ends into a solution of sulfuric acid, and the other two ends into separate containers of hydrogen and oxygen. Next, he realized that several sets of Pt electrodes could be used in series to get water and electricity and named his cell “gas battery” [10], which would be called to be “fuel cell” in late 19$^{th}$ century. In 1896, William W. Jacques developed first applicable fuel cell in lab environment, “carbon battery”, in which air is injected into an alkali electrolyte [11].

Although research on fuel cell development began in early 1800s, fuel cells could not compete with hydro-electricity, steam plants and batteries for a long time due to their higher cost and complexity. Fuel cell research was accelerated after the mid-20$^{th}$ century. To begin with, Emil Baur performed experiments for high temperature fuel cells, and outlined the fundamentals of MCFCs in 1921 as he used molten silver electrolyte. Baur also discovered the idea of SOFCs with his studies on solid oxide electrolytes at high temperatures in 1930s [7].

Thomas F. Bacon developed the first industrially applicable fuel cell in 1933, producing electricity with hydrogen and air after a series of electrochemical reactions. Consequently, he started the research for alkaline fuel cells with nickel electrodes, and developed a fuel cell to be used in submarines during World War II. In his alkaline fuel cells, he considered KOH as electrolyte, which has more resistant to corrosion, instead of acid electrolytes. Bacon’s fuel cell was presented to Britain’s National Research Development Corporation in 1958, and then was proved to be reliable enough to be installed in Apollo spacecraft by Pratt & Whitney [8].

In 1960, G.H.J. Broers and J.A.A. Ketelaar reported the first continuous (6 month) operation of a complete MCFC using an electrolyte mixture of lithium carbonate, sodium and potassium at cell temperature 650 ºC [12,13]. Five years later than their invention, various MCFCs were tested by U.S. Army Engineer Research and Development Laboratory in Virginia. Meanwhile in 1961, the first PAFC was introduced by G.V. Elmore and H.A. Tanner with their work entitled "Intermediate Temperature Fuel Cells" [7].

In 1950, Teflon (polytetrafluoroethylene or PTFE) was started to be produced, which is a turning point in fuel cell research. PTFE has been a vital material for the development of the current aqueous electrolyte fuel cells. After the availability of PTFE, attention was focused on the PEFCs. In 1950s and `60s, General Electric Company (GE) worked on PEFCs through the works of Thomas Grubb and Leonard Niedrach. Thomas Grubb considered an electrolyte membrane made of ion-exchange polystyrene sulfonated for his fuel cell designs in 1955. Leonard Niedrach improved Grubb's fuel cells by depositing Pt on the ion-exchange membrane. In this way, Pt would act as a catalyst for the reactions of hydrogen oxidation and oxygen reduction. In the 1960s, GE developed the first PEFC technology through a program with the U.S. Navy's Bureau of Ships and the U.S. Army Signal Corps. Their cells were compact and portable, however their Pt catalysts were expensive. Another important PEFC research by GE is performed in collaboration with NASA and McDonnell Aircraft during the Gemini program in 1960 and `70s [7,8].

In mid-1970s, GE continued its research in PEFC technology, and developed electrolysis support with polymer electrolyte membrane for U.S. Navy Oxygen Generating Plant. This technology is then adapted by British Royal Navy in early 1980s. Progress in

PEFC field continued with the development of a cell operated with methanol, instead of pure hydrogen, by the Jet Propulsion Laboratory of NASA in 1990 [7,8].

Nowadays, fuel cells are considered in several fields, including stationary [14-16], transport [8,17,18], portable [19] and micro power applications [20]. Honda's fuel cell vehicles have been available for consumers since 2008 [8,21]. Moreover, Hyundai and Toyota have recently announced their fuel cell electric vehicles (FCEVs) in automotive sector [21]. Along with those tremendous advances, the revenues in fuel cell industry reached to $2.2 billion worldwide with the production of 50,000 new fuel cells (180 MW total capacity) in 2014 [22].

### 1.3 Introduction to polymer electrolyte fuel cells (PEFCs)

As mentioned earlier, PEFCs are one of the most popular fuel cells due to their low temperature operation, reduced electrolyte corrosion and quick start-up (Table 1.1). Figure 1.1 introduces the basic operation and a schematic of a typical PEFC [23]. As seen from this figure, they use hydrogen (or hydrogen-rich fluid) as a fuel at the anode side, oxygen (or air) at the cathode side and perfluorosulfonic acid membrane as an electrolyte. The catalyst layers (CLs) are composed of the pure Pt or carbon supported Pt/Pt-alloy electrodes in most PEFC designs.

Basic operation of a PEFC is very simple and easy, as in Figure 1.1. Humidified hydrogen and oxygen (or air) are continuously supplied at anode and cathode flow fields of a PEFC, respectively. Hydrogen is dissociated into protons and electrons at the anode CL, and protons are carried to the cathode CL through the ion-exchange membrane. Electrons are also transferred to the cathode CL with the help of an external circuit

(Figure 1.1). Oxygen, protons and electron meet at the cathode electrode in order to generate water, heat and electricity.

### 1.3.1 Materials, components and their basic properties in PEFC design

Materials and components included in PEFC operation can be classified into two categories: i) cell components and ii) system or balance of plant (BOP) components. Principle cell components are presented in Figure 1.2 [24], which includes catalyst coated membrane (CCM), gas diffusion layers (GDLs), gaskets, graphite flow blocks (or bipolar plates), current collectors and end plates. The CCM is an essential part of a cell, and it is composed of an electrolyte sandwiched with electrodes on both anode and cathode sides.

In a typical PEFC, electrolytes are the solid ion-exchange membranes, which are generally made of perfluorosulfonic acid (PFSA) with polytetrafluoroethylene (Teflon®) backbone. The main functions of the ion-exchange membrane are to conduct protons from anode to cathode, and to separate the reactant gases. Proton conductivity of PEFC electrolyte is a function of membrane water content, i.e. higher water content leads to better proton conduction. Therefore, it is critical to operate the fuel cell with well humidified gases, however it should also be noted that excess water causes cell flooding which decreases the performance. For this reason, water management across the membrane and adjustment of cell temperature are the vital issues in PEFCs. In membrane structure, Teflon® is hydrophobic (water repellent) and PFSA is hydrophilic (having an affinity for water) to adequately deliver the protons and manage the water transport. In addition, ion-exchange membranes should maintain a good electrical insulation, good durability, chemical resistance and low gas permeability (to prevent the crossover of reactants).

Electro-catalysts, or CLs in Figures 1.1 and 1.2, are critical components where the electrochemical reactions take place. They have to effectively transport reactants, products, ions and electrons. Furthermore, their electrochemically active surface area (ECSA) should be high enough to achieve better durability and performance. In order to attain these properties, the main component of CLs is either pure Pt, carbon supported Pt or Pt-alloys. They are also manufactured with a porous structure with a fraction of ionomer (~30%) and PTFE content (for water removal) [25]. The electro-catalysts are usually applied onto the membrane surface by hot pressing the catalyst-ionomer mixture.

GDLs are located between the flow field and the CL (Figure 1.2). Their most significant functions are: i) electron conduction to and from the CLs, ii) transport of reactants and products, iii) dissipation of the generated heat from CL to current collector and iv) the mechanical support for the CCM structure. They are generally made up of carbon paper. However, some manufacturers implement hydrophobic micro-porous layers (MPLs) into the carbon support for better gas transport and water removal. MPL also provides enhanced electrical conductivity between the GDL and the CL. During the process of fuel cell assembling, GDL is compressed between the bipolar plates and the CL, and the amount/level of compression should be considered carefully to maintain optimum PEFC performance.

Bipolar plates provide the flow fields for the anode and cathode gases, and they need to be electrically conductive to transfer electrons from GDLs to current collectors. Besides, their material has to be resistant to corrosion to avoid any particle leaching and performance degradation. For these reasons, bipolar plates are commonly manufactured as graphite blocks with flow fields, even if the machining cost is high [26,27].

Gaskets, current collectors and end plates are the other PEFC components (Figure 1.2). Gaskets, which are incompressible, are usually produced with Teflon®, and they are used to seal gases (to avoid leakage) and control the pressure in GDL compression during cell assembly. Current collectors help to conduct electrons from anode to cathode through external circuit. End plates are designed to have the inlet and outlet ports for the fuel and oxidant besides their function to distribute the axial load evenly during assembly.

System or BOP components are the items which are not included in PEFC stack, however are required to operate the fuel cell power plants. Compressors, pumps, humidifiers, cooling systems, power conditioning/control, start-up power systems and hydrogen reformers (if liquid hydrocarbon or alcohol is used) are the most common BOP components [5,25].

### 1.3.2 Reaction kinetics, thermodynamics and overpotential losses

Anode and cathode reactions in a PEFC are, respectively, given as follows:

$$H_2 \rightarrow 2H^+ + 2e^- \qquad \Delta H_1 = 0 \text{ kJ/mol} \tag{1}$$

$$\tfrac{1}{2}O_2 + 2H^+ + 2e^- \rightarrow H_2O_{(l)} \qquad \Delta H_2 = -286 \text{ kJ/mol} \tag{2}$$

where $\Delta H_1$ and $\Delta H_2$ are the enthalpy differences (heat released) when the product water is in liquid form. Hence, the overall reaction and enthalpy difference (total heat released) are expressed as:

$$H_2 + \tfrac{1}{2}O_2 \rightarrow H_2O_{(l)} \qquad \Delta H_f = \Delta H_1 + \Delta H_2 = -286 \text{ kJ/mol} \tag{3}$$

Note that thermal cell potential, $E_{th}$, corresponding to $\Delta H_f$ for reaction (3) is calculated by:

$$E_{th} = \Delta H_f / nF = 1.48 \text{ V} \quad (4)$$

which is the maximum potential a PEFC can achieve. The terms n and F are the number of electrons (=2 from reaction (1)) and the Faraday's constant (=96485.3 C/mol), respectively. $E_{th}$ can be obtained if there are assumed to be no losses and fuel cell is operated with hydrogen, pure oxygen and byproduct of liquid water. Nevertheless, some portion of the total heat in reaction (3) cannot become the useful energy due to the entropy change ($T\Delta S$) and reversible losses. The maximum useful energy, $\Delta G_f$, can be evaluated from the Gibbs free energy change in reaction (3) as shown:

$$\Delta G_f = \Delta G_{H_2O_{(l)}} - (\Delta G_{H_2} + \Delta G_{O_2}) = -237 \text{ kJ/mol} \quad (5)$$

which is defined at standard cell temperature, 298 K, and standard pressure, 1 atm.

Next, one can calculate the maximum thermodynamic efficiency of a fuel cell, $\beta_{ideal}$, and equilibrium potential at standard temperature and pressure, $E_{st}^0$:

$$\beta_{ideal} = \Delta G_f / \Delta H_f = 0.83 \quad (6)$$

$$E_{st}^0 = \Delta G_f / nF = 1.229 \text{ V} \quad (7)$$

when the product of water is in liquid phase. Therefore, Nernst equation presents the equilibrium potential, $E^0$, at any cell temperature, T, and pressure, P, as:

$$E^0 = 1.229 \text{ V} + \frac{RT}{nF} \ln(P_{H_2} P_{O_2}^{1/2}) \quad (8)$$

where R is the universal gas constant (=8.314 J/mol.K), and $P_{H_2}$, $P_{O_2}$ and $P_{H_2O}$ are the partial pressures of hydrogen, oxygen and water, respectively.

Actual fuel cell efficiency can also be determined by the following relation [5,28]:

$$\beta_{\text{actual}} = \xi \frac{Useful\ Energy}{\Delta H_f} = \xi \frac{Useful\ Power}{\Delta G_f / 0.83} = 0.83\xi \frac{E_{cell}.Current}{E^0_{st}.Current} = 0.675\xi\, E_{cell} \qquad (9)$$

where $E_{cell}$ is the actual cell voltage taking into account all potential losses, and $\xi$ is the fuel utilization factor (fraction of the total inlet fuel, which is depleted). Actual fuel cell performance is commonly assessed by the polarization curve, which demonstrates actual cell voltage versus current density in Figure 1.3 [25]. As seen from this figure, there are five types of overpotential losses in PEFC operation, represented with regions I-V.

Region I in Figure 1.3 shows the region which is dominated by the "activation overpotential". These losses are observed due to the energy barrier to overcome the activation of the electrode reactions, and they mostly depend on the CL material/structure and reactants [5]. Both anode and cathode reactions in a PEFC contribute to the activation overpotential, $\eta_{a,a}$ (anode overpotential) and $\eta_{a,c}$ (cathode overpotential). However, its significant portion stems from the cathode electrode owing to the sluggish kinetics of the oxygen reduction reaction (ORR).

"Ohmic overpotential" dominates the region II, as in Figure 1.3. Ohmic losses originate from the ionic resistance in the membrane and CL ($R_{ionic}$), electronic resistances in the CL, GDL and current collectors ($R_{electric}$), and contact resistances between the cell components ($R_{contact}$). It depends on the current density, stack geometry, temperature and material selection [5]. Overpotential due to ohmic resistances can simply evaluated by:

$$\eta_{ohmic} = iR_{ohmic} = i(R_{ionic} + R_{electric} + R_{contact}) \qquad (10)$$

where i is the cell current and $R_{ohmic}$ is the total ohmic resistance.

At higher current densities (more than around 1 $A/cm^2$), region III in Figure 1.3, "concentration overpotential" gives a significant contribution to the total potential losses. As the fuel cells operate at higher current densities, consumption rates of fuel and oxidant becomes faster and reactant surface concentrations are reduced. Hence, concentration overpotential is caused by the mass transport limitations of the anode and cathode reactants. Similar to activation losses, total concentration overpotential is the sum of anodic, $\eta_{m,a}$, and cathodic, $\eta_{m,c}$, mass transport losses. Applied current density, reactant activity (utilization) and electrode structure affect the mass transport in a PEFC [5]. At this point, it should be emphasized that activation, ohmic and concentration losses exist throughout the entire current range in Figure 1.3. Regions I-III are the sections where each of them dominates the total overpotential.

In Figure 1.3, open circuit voltage (OCV) of a fuel cell is actually lower than the equilibrium potential, $E^0$ (from equation (8)), with the losses in region IV, namely "mixed potential losses". These losses may arise from the conditions such as, reactant crossover through the electrolyte, possible platinum oxide formations at the electrodes, electrical shorts in the PEFC stack, using air as oxidant (instead of pure oxygen) and contaminants in the fuel or oxidant streams.

Finally, region V (Figure 1.3) indicates the reversible thermodynamic losses due to entropy change and not using standard operating temperature and pressures. It is simply the difference between the maximum thermal cell potential, $E_{th}$, and equilibrium potential, $E^0$, which is already mentioned earlier (recall equations (4), (7) and (8)).

When all overpotential losses are taken into account, actual cell voltage is given by:

$$E_{cell} = E^0 - (\eta_{a,a}+\eta_{a,c}) - \eta_{ohmic} - (\eta_{m,a}+\eta_{m,c}) - \eta_x \quad (11)$$

where $\eta_x$ is the mixed potential losses.

### 1.3.3 Advantages of PEFCs

As discussed earlier, PEFCs are becoming more popular day by day in portable power, stationary and automotive applications compared to other types of fuel cells. The advantages below [8] play an important role in PEFC's popularity:

- ✓ Their sizes and operations can be adjusted to generate high power density.
- ✓ Their mechanical design is simple, compact and robust.
- ✓ Their materials are resistant to corrosion.
- ✓ They can work at pressures lower than 2-3 atm, and have a tolerance to pressure difference between anode/cathode inlet and outlets.
- ✓ Solid polymer membrane is considered as their electrolyte. Therefore, design concerns such as handling, assembly and tightness of fuel cell stack are easily managed.
- ✓ They have a high $CO_2$ tolerance.

### 1.3.4 Challenges and commercialization barriers

In contrast to their advantages above, some disadvantages of PEFCs can be listed as follows [8,29]:

- ✓ Their tolerance to fuel impurities such as CO and sulfur is low. According to SAE Fuel Cell Standards Committee [30], CO tolerance is only 0.2 ppm and total sulfur tolerance is 0.004 ppm for fuel cells in automotive applications. For this reason,

complex and efficient reformer systems may be required to obtain high purity hydrogen, if pure hydrogen is not used as the fuel source.

- ✓ The materials in their CL, which are mostly platinum group metals (PGM) are expensive.
- ✓ Longer lifetime needs to be established, along with more stable catalysts and membranes, in PEFC power plants.
- ✓ They require humidifiers as an additional BOP component.
- ✓ The total cost of PEFC power plants, including PEFC stack and BOP component costs, is expensive. More research should be conducted to decrease the cost.

Note that essential factors influencing the disadvantages above can be grouped into three: i) cost, ii) durability and iii) performance issues. These three issues are the main commercialization barriers in PEFC industry, and are to be separately described in this section. Table 1.2 demonstrates the U.S. DOE targets for a hydrogen fuel cell, based on 80 kW (net) energy-producing transportation fuel cell power system [21]. As in Table 1.2, there is an important gap between the 2015 status and set targets, especially, for the cost and durability of a PEFC system. Hence, there should be significant efforts to decrease the cost and increase the durability of the current technology.

***Cost***

In Figure 1.4, one can observe the trend in PEFC system cost (based on 80 kW (net) energy generation in transportation fuel cell power system and total production of 500,000 systems/year) from 2006 to 2015. U.S. DOE 2020 and ultimate targets are also presented in the same figure [31]. It is very apparent that cost is a significant challenge, and should be seriously considered in PEFC system design.

According to the published studies about automotive industry [21], BOP components constitute more than half of the PEFC overall system cost. Meanwhile, electro-catalyst materials and their application on the membrane surface represent the most expensive component in an automotive PEFC stack design [21]. Table 1.3 gives the cost analysis of a PEFC system, stack and their separate components with the comparison of 2015 statuses and 2020 targets [31]. As seen in this table, BOP components (air compressor, humidifier system and humidifier membrane) covers an important part in the total cost. Nevertheless, the components in BOP structure of fuel cell power plants are mature in technology, and it is very difficult to reduce their price. Meanwhile in Table 1.3, membrane electrode assembly (MEA), which includes membrane, CLs, GDLs and gaskets, is the most expensive part for the stack development. Therefore, research is mostly focused on decreasing the BOP system requirements and the CL cost in fuel cell systems.

***Durability***

As already mentioned, durability is an important consideration in PEFC applications. PEFC systems, including the stack and BOP components, should be more durable in order to meet the U.S. DOE 2015 and ultimate targets [21]. Durability is affected by the chemical/mechanical of materials, impurities in the fuel and air streams, relative humidity, current load cycling, start-stop cycling and freezing operating conditions. As a common effect, fuel cell degradation is the main reason for the low-durable operation of PEFCs. Among all other degradations in fuel cell stacks, catalyst and membrane degradations are detrimental in fuel cell lifetime. Furthermore, durability in BOP components should also be taken into account. Studies [21] indicate that 90% of system failures in automotive fuel cell systems are as a result of the BOP related incidents.

Fuel cell degradation can be divided into two different modes: mechanical and chemical degradation. And these modes are then grouped into two another types; reversible and irreversible mechanical/chemical degradation [32]. Fuel cell degradation is extensively explained in Ref. [25]. Table 1.4 summarizes the study in Ref. [25] and presents all kinds of degradation modes with brief explanations.

There are ongoing efforts to increase the durability of PEFC systems. The significant challenge is that cost and durability are strongly related to each other. In other words, PEFC durability can be improved in exchange for the increase in PEFC system cost, or vice versa. Current research topics on PEFC degradation include [33]:

- ✓ ECSA loss after catalyst dissolution.
- ✓ Corrosion on bipolar plates.
- ✓ Activity loss by catalyst support corrosion.
- ✓ Membrane degradation by mechanical stresses and chemical attacks.
- ✓ Pt particle growth and agglomeration.
- ✓ Voltage loss by the contact resistance between components.
- ✓ CL and membrane performance loss due to contamination.

In this thesis, performance loss or degradation due to contamination is the main concern of research. Section 1.5 will give the details about PEFC degradation which is driven by CO, metallic impurities and foreign substances from system (BOP) components.

***Performance***

Performance loss in PEFCs also depends on the system durability since it is strongly affected by chemical and mechanical degradation of the components. In addition to the

degradation, water management inside the membrane, the quality of BOP components, and start-up/shutdown times influence their performance data [21].

### 1.4 Experimental tools for the analysis of PEFC performance

Performance and durability of PEFCs can be assessed by various methods and measurements. In the next two sections, the methods used in this thesis are going to be explained.

#### 1.4.1 Galvanostatic and potentiostatic tests

Long-term performances and realistic time history profiles can be determined by galvanostatic (current-hold) and potentiostatic tests of fuel cells. In galvanostatic tests, cell current is held constant, and cell voltage and resistance are monitored with time. On the other hand, cell voltage is constant, and current and resistance are recorded versus time in potentiostatic tests.

Figure 1.5 demonstrates the galvanostatic test for a simple PEFC test at 400 $mA/cm^2$ [34], and the operating conditions are given in the figure caption. Note that galvanostatic/potentiostatic tests may be useful in two cases:

- Lifetime/durability of fuel cells and their degradation rates (in μV/h) are determined under normal operating conditions (as in Figure 1.5). These tests can also be applied to report the durability under extreme or cycling operating conditions, such as accelerated stress tests (AST).
- Effects of contaminants/impurities on PEFC performance can be investigated by their injection into anode or cathode inlets at some periods of time during galvanostatic/potentiostatic tests. Cell voltage/current drop and resistance increase

are recorded with the contaminant injection. It is also possible to observe whether the cell recovery is achievable or not after the contaminant injection is stopped.

### 1.4.2 Diagnostic (Electrochemical) techniques

Diagnostic measurements are important tools providing helpful support for PEFC testing, in contribution to galvanostatic/potentiostatic tests. There are two basic types of diagnostic tool: electrochemical [35] and physical/chemical methods [36]. Electrochemical methods are employed in this thesis and are to be explained in this section.

Polarization (I-V) curves, cyclic voltammetry (CV), linear sweep voltammetry (LSV) and electrochemical impedance spectroscopy (EIS) are the most common electrochemical methods, which are considered in this thesis. Polarization curve is a type of curve, which gives information about the performance losses in PEFCs. It is also possible to make comments on the individual and combined effects of performance losses with the I-V data, which can be obtained by monitoring the cell voltage at several cell current densities. Polarization curves and overpotential losses have already been mentioned in detail with Figure 1.3 and in section 1.3.2.

CV is a tool to evaluate the ECSA of the membrane electrode assembly (MEA) in PEFCs. It is measured by sweeping the cell voltage back and forth between two limits and recording the associated cell current density. Hydrogen ($H_2$) and nitrogen ($N_2$) are used at the anode and cathode sides, respectively. Therefore, two peaks can be obtained, as in the representative CV [37] (Figure 1.6). The peak above the x-axis is driven by the hydrogen desorption, and the peak below the x-axis is due to the hydrogen adsorption in Figure 1.6.

The equations of hydrogen adsorption/desorption are given on the figure, and the operating conditions are presented in the figure caption.

In order to calculate the ECSA ($cm^2$ Pt/g Pt), the area under the hydrogen desorption peak (shaded area in Figure 1.6) is first integrated to find the total charge ($\mu C/cm^2$) for hydrogen desorption. Next, it is divided by the reference charge density, hydrogen desorption charge for a smooth Pt electrode (=210 $\mu C/cm^2$). Finally, the resulting value is divided by the total Pt loading at CL (g Pt/$cm^2$ Pt) to reveal the ECSA value for the MEA [38].

LSV is another electrochemical diagnostic tool which is used to find the amount of fuel crossover through electrolyte and to determine whether there are significant electrical shorts within the PEFC system. In both CV and LSV measurements, potentiostat/galvanostat is utilized with counter/reference electrode (CE/RE) as the fuel cell anode and working electrode (WE) as the cathode. Similar to CV, $H_2$ and $N_2$ flow, respectively, through anode and cathode sides during LSV. Unlike CV, cell voltage is swept just in forward direction (not back and forth), and current density is recorded. Figure 1.7 is a typical $H_2$ crossover curve, showing the results for three different cells [39]. The cells, operating at 35 and 75 ºC, have no shorts (constant current density after 0.2 V) and have fuel crossover at around 1 $mA/cm^2$. On the other hand, the degraded cell at 50 ºC (Figure 1.7) have internal short.

EIS is also a powerful tool, which is performed by a frequency response analyzer (FRA). A small AC voltage or current/perturbation signal (of known amplitude and frequency) is applied to the cell under open circuit voltage (OCV) condition or load. Next, FRA determines the fuel cell's response to this signal, with the impedance, phase angle

and frequency. Applied signal is generally swept from high (~10-20 kHz) to low (~0.1-0.2 kHz) frequency. In this way, activation, ohmic and mass transport losses on cell voltage can be separately assessed and quantified by EIS, using the measured data and its equivalent electrical circuit model. In other words, smooth lines are fitted to the EIS data with the help of an equivalent circuit, which consists of resistors and constant phase elements (CPE), as seen in Figures 1.8a-b [40,41]. Note that EIS and its interpretation as a diagnostic tool are to be explained in detail in section 5.

### 1.5 Durability and performance loss due to contamination in PEFCs

As previously mentioned in Table 1.4 and section 1.3.4, contamination is one of the main source of degradation, which leads to performance and durability loss in PEFCs [25,42,43]. Contaminants mostly originate from fuel/oxidant streams or PEFC system components, and significantly impact the PEFC operation by degrading the electrodes/electrolytes. Table 1.5 lists the possible contaminants and their sources, as reported in earlier studies [42,44-46].

#### 1.5.1 Anode carbon monoxide (CO) poisoning

There are storage issues with pure hydrogen as a PEFC anode fuel owing to its high volumetric density. For this reason, hydrogen is commonly produced from some hydrocarbon fuels (methanol, ethanol, gasoline, etc.) before supplying into anode inlet [47,48]. Reformation of these hydrocarbon fuels for hydrogen generation forms also 1-2% CO as a byproduct [49]. It should be noted that CO strongly binds onto Pt surface at anode CL, blocking the available sites for hydrogen adsorption and hence for hydrogen oxidation [42,50,51].

Steady state effects of CO poisoning can be observed in Figure 1.9a [42,52], which gives the comparison of PEFC polarization curves with pure and CO-contaminated (25-250 ppm) $H_2$ flows through anode inlet. It is clear from Figure 1.9a that even 25 ppm CO in $H_2$ notably deteriorates the I-V curve at steady state condition. Similar effect on PEFC polarization is also demonstrated in Figure 1.9b for 100 ppm CO in transient condition [42,52]. After 2 hours of 100 ppm CO-poisoned flow, cell performance drops to impractical values as in Figure 1.9b.

There are several methods to mitigate CO poisoning, such as oxygen bleeding into anode, using CO-tolerant catalysts, Preferential Oxidation (PROX) and Electrochemical Preferential Oxidation (ECPROX). The techniques to avoid CO poisoning can be reviewed in Refs. [42,43,53,54]. More detailed explanations on CO poisoning mechanism and its mitigation methods are to be presented in chapters 2 and 3.

### 1.5.2 Metallic and cationic impurities

Impure fuel/oxidant feeds, corroded metallic fuel cell or BOP components, fittings, tubings and undesired ions in the humidifier/coolant systems cause metallic impurities in PEFCs [55,56]. Foreign ions include the alkali metals ($Li^+$, $Na^+$, $K^+$, $Rb^+$, $Cs^+$), the alkaline earths ($Mg^{2+}$, $Ba^{2+}$, $Sr^{2+}$, $Ca^{2+}$), transition elements ($Ag^+$, $Cu^{2+}$, $Fe^{2+}$, $Mn^{2+}$, $Ni^{2+}$, $Zn^{2+}$, $Fe^{3+}$, $Cr^{3+}$) and $Al^{3+}$ [57]. The negative impacts of ionic contamination on PEFC operation can be listed as below:

- They may cause mechanical degradation, leading to pinhole formation or blocking the gas channels [5,25].

- They increase the chemical degradation rate of electrolytes by catalyzing the peroxide radical attacks and the subsequent fluoride losses [43,57].
- The sulphonic sites in Nafion® have higher affinity for foreign cations than for protons. Therefore, protons are displaced by the cationic impurities in the electrolyte membrane, which decreases the membrane protonic conductivity [57].
- Foreign cationic impurities also affect the mass transport within the membrane by decreasing the water diffusion coefficient and increasing the water transfer coefficient [57].

An example showing the effect of cationic contamination is given in Figure 1.10. In this figure, the polarization curves are presented for a PEFC operating with $H_2$/air flows at anode/cathode and $H_2/O_2$ flows at anode/cathode sides. The polarization data are compared for the cases of uncontaminated, 41% $Fe^{3+}$ contaminated membrane and 100% $Fe^{3+}$ contaminated membrane [58]. It is obvious from Figure 1.10 that cell performance is severely damaged with $Fe^{3+}$ impurity within the electrolyte. There is ~80 mV drop in cell voltage at 0.60 A/cm$^2$ (Figure 1.10) even for the best case scenario ($O_2$ cathode flow with 41% contaminated MEA) [58].

Although the impacts of foreign cations on PEFC performance are detrimental, there are very studies to mitigate their effects in literature [59-61]. Metallic impurities, their mechanisms and the mitigation strategies can be reviewed in Refs. [42,43,57].

### 1.5.3 Organic materials from system components

As BOP system occupy more than half of the total system cost in PEFCs, the possible reduction of cost by using cheaper BOP components becomes more obvious year by year

[21,31]. However, studies [45,46,62-65] indicate that organic leachates from components, such as structural plastics, lubricants, sealants, adhesives, greases and hoses, may damage the PEFC performance and durability. Moreover, the National Renewable Energy Laboratory (NREL), in collaboration with General Motors (GM) and the University of South Carolina, has implemented a simple diagram as "leaching index", which presents the cell voltage loss and amount of leaching versus material cost for BOP components [45,46]. It is proven from "leaching index" that as the material cost decreases, there is a general increasing trend in cell voltage loss and the organic leachates from components.

When the above concerns are considered, possible contaminants from BOP system components are detected by studies in Refs. [45,46]. Furthermore, impact of structural plastic leachates on fuel cell performance is reported by Yu et al. [64]. Their work [64] indicates that the leachants cause in loss of available Pt sites, decrease in membrane conductivity, and thus decrease in fuel cell voltage with only 61% recovery.

GM and NREL's study [63] on ECSA loss after contaminating the fuel cell with structural plastics like polyamides is given with the CV plots in Figure 1.11. ECSA is significantly lost and available Pt sites are considerably reduced with the contamination of structural plastics (Figure 1.11). In addition, Figure 1.12 gives the performance test of a PEFC with the injection of an epoxy adhesive through cathode inlet at constant current (0.2 $A/cm^2$) [65]. As indicated in Figure 1.12, epoxy adhesive poisons the cell with a vital decrease in cell voltage from 0.8 to 0.2 V. Although the epoxy injection is stopped at time, t=~21 hours, there is no improvement in cell voltage (self-induced recovery in Figure 1.12).

## 1.6 Research motivation and objectives

Although significant progress has been employed in PEFC research, further studies are still required to make it more commercialized and more competent with traditional combustion engines. The most important challenge is to reduce their cost while increasing their durability and performance to meet the established standards. Besides, durability and performance are strongly influenced by the fuel cell degradation due to the contamination. Therefore, it is very important to mitigate or eliminate the impact of contaminants in PEFC operation.

CO contaminant in $H_2$ fuel also exhibits the oscillative behavior in cell voltage. There is not a complete understanding about the oscillations in $H_2$/CO systems in literature. Existing numerical models to describe the oscillative mechanism are oversimplified and non-dimensional. Further understanding of this phenomenon is needed with more detailed reaction kinetics and surface coverage relations for the adsorbed species. In chapter 2, a one-dimensional transient numerical model is developed to explain the voltage and surface coverage oscillations for 1,000 ppm CO (in $H_2$) at Pt CL. Adsorbed $H_2$, CO and OH coverages on Pt surfaces are demonstrated with their oscillations along the CL thickness for the first time.

CO poisoning at fuel cell anode and the efforts to mitigate its impact on cell performance have been extensively studied. However, there is not yet a convincing numerical study to alleviate or remove the effect of high concentration CO poison in $H_2$ (>10,000 ppm) from catalyst surface. Most existing studies for high level of CO poisoning are experimental and suggest very complex mechanisms to remove the CO contamination from the Pt surface. Therefore, a simple numerical work is needed for the simulation of

high concentration CO poisoning mechanism and its mitigation, which may propose a straightforward setup for the removal of CO impurities in real-life applications. The numerical model, introduced in chapter 2, is extended for the simulation of 10,000 ppm CO poisoning on Pt surface in chapter 3. Moreover, a simple and robust method, “current pulsing” technique, is suggested and modelled (for the first time) to efficiently remove CO poison from the CL in chapter 3. Note that the method, results and findings in chapters 2 and 3 are published in Ref. [66].

Performance degradation in PEFCs is broadly addressed in literature when the cells are exposed to metallic impurities. Meanwhile, there is a new expanding study about the effect of organic impurities, originating from BOP components, in PEFC operation. However, there is not a well-known study to mitigate the performance loss after the exposure of metallic or organic contaminants to the fuel cell. There is, at least, a demand for an investigation to prevent the cationic impurity formation from fuel cell components and organic leachants from BOP system, which is not available in history. In this thesis, commercially available cleansing agents are proposed (for the first time) for the regular cleaning/maintenance of fuel cell and BOP system components in order to avoid the corrosion of metallic components and leaching of organic compounds. In chapter 4, several commercial cleansers are down selected, and then screened by injection into PEFC inlet whether they have negative effect on PEFC operation, or at least whether their effect is recoverable. A proper cleansing agent is selected, for the first time, with minimal and recoverable impact on the cell performance.

Chapter 5 presents the in-depth analysis of the result from the screening test of the selected cleansing agent (in Chapter 4). An equivalent electrical circuit model is fitted to

the EIS data from the test of the chosen cleanser, and individual resistances are compared with and without the cleanser injection. Furthermore, gas diffusion coefficient and mass transfer (concentration) losses at the PEFC cathode are analyzed with and without the cleanser contamination. The works in chapters 4 and 5 are submitted to be published under the title of "Experimental observation of performance in PEFCs with the injection of cleansing agents through cathode inlet".

Finally, overall conclusion from this thesis, some limitations and recommendations for future work are presented in chapter 6.

### 1.7 References

[1] U.S. Department of Energy; Energy Information Administration. Annual energy outlook 2017. https://www.eia.gov/outlooks/aeo/.

[2] Davis SC, Williams SE, Boundy RG. Transportation Energy Data Book: Edition 35. Oak Ridge, Tennessee: Department of Energy. 2016; http://cta.ornl.gov/data/spreadsheets.shtml.

[3] U.S. Department of Energy Hydrogen and Fuel Cells Program Record 8013. Air quality and population. November 2008; https://www.hydrogen.energy.gov/program_records.html.

[4] Mansor NB. Development of catalysts and catalyst supports for polymer electrolyte fuel cells. Ph.D. Thesis. University College London 2014.

[5] EG&G technical Services, Inc. Fuel cell handbook. 7th ed. U.S. Department of Energy; November 2004.

[6] Garraín D, Lechón Y, Rúa CDL. Polymer electrolyte membrane fuel cells (PEMFC) in automotive applications: environmental relevance of the manufacturing stage. Smart Grid and Renewable Energy 2011;2(2):68.

[7] Smithsonian National Museum of American History. Collecting the history of fuel cells. April 2016; http://americanhistory.si.edu/fuelcells/.

[8] Andújar JM, Segura F. Fuel cells: History and updating. A walk along two centuries. Renewable and sustainable energy reviews 2009;13(9):2309-22.

[9] Kahlbaum GWA, Darbishire FV (eds) (1899) The letters of Faraday and Schoenbein, 1836-1862. Swabe, Bale, Williams and Norgate, London. http://www.archive.org/stream/lettersoffaraday00fararich#page/n9/mode/2up.

[10] Grimes P. Historical pathways for fuel cells. The new electric century. Battery Conference on Applications and Advances, 2000. The Fifteenth Annual: IEEE; 2000.

[11] Appleby AJ. From Sir William Grove to today: fuel cells and the future. J Power Sources 1990;29(1-2):3-11.

[12] Selman JR. Molten-salt fuel cells—Technical and economic challenges. J Power Sources 2006;160(2):852-7.

[13] Dicks AL. Molten carbonate fuel cells. Current Opinion in Solid State and Materials Science 2004;8(5):379-83.

[14] Lee JH, Baek ST, Jung HJ, Kang HH, Chung JM, Suh IY. Development of a 250kW power conditioning system for molten carbonate fuel cell power generation system. Electrical Machines and Systems, 2007. ICEMS. International Conference on: IEEE; 2007.

[15] Segura F, Durán E, Andújar J. Design, building and testing of a stand alone fuel cell hybrid system. J Power Sources 2009;193(1):276-84.

[16] Williamson SS, Emadi A, Shahidehpour M. Distributed fuel cell generation in restructured power systems. Power Engineering Society General Meeting, 2004. IEEE: IEEE; 2004.

[17] Chen F, Fernandes TRC, Roche MY, Graça Carvalho Mda. Investigation of challenges to the utilization of fuel cell buses in the EU vs transition economies. Renewable and Sustainable Energy Reviews 2007;11(2):357-64.

[18] Andujar J, Segura F, Vasallo M. A suitable model plant for control of the set fuel cell−DC/DC converter. Renewable Energy 2008;33(4):813-26.

[19] Kim T, Kwon S. MEMS fuel cell system for portable power source: Integration of methanol reformer, PROX, and fuel cell. Proceedings of the Micro Electro Mechanical Systems, 2008. IEEE 21st International Conference on MEMS; 2008.

[20] Abdullah M, Gan Y. Feasibility study of a mini fuel cell to detect interference from a cellular phone. J Power Sources 2006;155(2):311-8.

[21] U.S. Department of Energy Fuel Cell Technologies Office. Multi-year research, development and demonstration plan, section 3.4 - fuel cells. June 2016. http://energy.gov/sites/prod/files/2016/06/f32/fcto_myrdd_fuel_cells_0.pdf.

[22] U.S. Department of Energy Fuel Cell Technologies Office. Fuel cell technologies market report 2014. https://energy.gov/sites/prod/files/2015/10/f27/fcto_2014_market_report.pdf.

[23] Jiao K, Li X. Water transport in polymer electrolyte membrane fuel cells. Progress in Energy and Combustion Science 2011;37(3):221-91.

[24] Wang X. Systematic study of materials and structures for optimizing performance of polymer electrolyte membrane fuel cells. Ph.D. Thesis. University of Connecticut 2014.

[25] Mench MM. Fuel cell engines. John Wiley & Sons, London, 2008.

[26] Turner JA, Wang H, Brady MP. Corrosion protection of metallic bipolar plates for fuel cells. DOE Hydrogen Program Review, 2005; http://www.nrel.gov/docs/fy05osti/38190.pdf.

[27] Weil KS, Kim JY, Xia G, Yang ZG, Chang S, Hardy M. Development of low-cost, clad metal bipolar plates for PEM fuel cells. 2005 Annual Progress Report, DOE Hydrogen, Fuel Cells, and Infrastructure Program, www.hydrogen.energy.gov/annual_progress05_fuelcells.html#d.

[28] Singhal SC, Kendall K. High-temperature solid oxide fuel cells: Fundamentals, design and applications. Elsevier, Oxford, New York, 2003.

[29] Liu D, Case S. Durability study of proton exchange membrane fuel cells under dynamic testing conditions with cyclic current profile. J Power Sources 2006;162(1):521-31.

[30] Fuel Cell Standards Committee. Information Report on the Development of a Hydrogen Quality Guideline for Fuel Cell Vehicles, SAE, J2719. International Organization for Standardization, Hydrogen Fuel–Product Specification–Part 2:14687-2.

[31] U.S. Department of Energy Hydrogen and Fuel Cells Program Record 15015. Fuel cell system cost - 2015. October 2015; https://www.hydrogen.energy.gov/program_records.html.

[32] Vielstich W, Lamm A, Gasteiger HA. Handbook of fuel cells: Fundamentals, technology and applications. Wiley, New York, 2003.

[33] USDRIVE. Fuel cell technical team roadmap. June 2013; https://energy.gov/sites/prod/files/2014/02/f8/fctt_roadmap_june2013.pdf.

[34] Uddin MA, Park J, Ganesan S, Pasaogullari U, Bonville L, Molter T. A cationic contamination in PEFC cathode: A cause and effect study. ECS Transactions 2015;66(24):29-36.

[35] Wu J, Yuan XZ, Wang H, Blanco M, Martin JJ, Zhang J. Diagnostic tools in PEM fuel cell research: Part I Electrochemical techniques. Int J Hydrogen Energy 2008;33(6):1735-46.

[36] Wu J, Yuan XZ, Wang H, Blanco M, Martin JJ, Zhang J. Diagnostic tools in PEM fuel cell research: Part II: Physical/chemical methods. Int J Hydrogen Energy 2008;33(6):1747-57.

[37] Cooper KR. In situ PEM fuel cell electrochemical surface area and catalyst utilization measurement. Fuel Cell Mag 2009:1-3.

[38] Ralph T, Hards G, Keating J, Campbell S, Wilkinson D, Davis M, et al. Low cost electrodes for proton exchange membrane fuel cells performance in single cells and Ballard stacks. J Electrochem Soc 1997;144(11):3845-57.

[39] Cooper KR. In situ PEMFC fuel crossover and electrical short circuit measurement. Fuel Cell Mag 2008:34-5.

[40] Han M, Xu J, Chan S, Jiang SP. Characterization of gas diffusion layers for PEMFC. Electrochim Acta 2008;53(16):5361-7.

[41] Arvay A, Yli-Rantala E, Liu CH, Peng XH, Koski P, Cindrella L, et al. Characterization techniques for gas diffusion layers for proton exchange membrane fuel cells–A review. J Power Sources 2012;213:317-37.

[42] Cheng X, Shi Z, Glass N, Zhang L, Zhang J, Song D, et al. A review of PEM hydrogen fuel cell contamination: Impacts, mechanisms, and mitigation. J Power Sources 2007;165(2):739-56.

[43] Zamel N, Li X. Effect of contaminants on polymer electrolyte membrane fuel cells. Progress in Energy and Combustion Science 2011;37(3):292-329.

[44] Liu W. Activated carbon fiber filter media for proton exchange membrane fuel cell. Ph.D. Thesis. Auburn University 2010.

[45] USDRIVE. Highlights of technical accomplishments 2014. March 2015; https://www.energy.gov/eere/vehicles/downloads/vehicle-technologies-office-us-drive-2014-technical-accomplishments-report.

[46] National Renewable Energy Laboratory (NREL). Making fuel cells cleaner, better and cheaper. Highlights in Research and Development. January 2015; http://www.nrel.gov/docs/fy15osti/63382.pdf.

[47] Bentley J, Barnett B, Hynek S. Multifuel reformer and on-board hydrogen storages. 1992 fuel cell seminar; 1992:455-60.

[48] Loftus P, Thijssen J, Bentley J. Development of a multi-fuel partial oxidation reformer for transportation applications. 1994 Fuel Cell Seminar; 1994:487-90.

[49] Divisek J, Oetjen H, Peinecke V, Schmidt V, Stimming U. Components for PEM fuel cell systems using hydrogen and CO containing fuels. Electrochim Acta 1998;43(24):3811-5.

[50] Baschuk J, Li X. Carbon monoxide poisoning of proton exchange membrane fuel cells. Int J Energy Res 2001;25(8):695-713.

[51] Vogel W, Lundquist L, Ross P, Stonehart P. Reaction pathways and poisons—II: The rate controlling step for electrochemical oxidation of hydrogen on Pt in acid and poisoning of the reaction by CO. Electrochim Acta 1975;20(1):79-93.

[52] Oetjen H, Schmidt V, Stimming U, Trila F. Performance data of a proton exchange membrane fuel cell using $H_2$/CO as fuel gas. J Electrochem Soc 1996;143(12):3838-42.

[53] Liu Z. Effects of fuel and air impurities on PEFC performance. Polymer Electrolyte Fuel Cells: Science, Applications, and Challenges 2013:427.

[54] Mehmood A, Scibioh MA, Prabhuram J, An M, Ha HY. A review on durability issues and restoration techniques in long-term operations of direct methanol fuel cells. J Power Sources 2015;297:224-41.

[55] Kundu S, Simon LC, Fowler M, Grot S. Mechanical properties of Nafion™ electrolyte membranes under hydrated conditions. Polymer 2005;46(25):11707-15.

[56] Kelly MJ, Fafilek G, Besenhard JO, Kronberger H, Nauer GE. Contaminant absorption and conductivity in polymer electrolyte membranes. J Power Sources 2005;145(2):249-52.

[57] Rama P, Chen R, Andrews J. A review of performance degradation and failure modes for hydrogen-fuelled polymer electrolyte fuel cells. Proc IMechE Part A: J Power Energy 2008;222(5):421-41.

[58] St-Pierre J, Wilkinson DP, Knights S, Bos ML. Relationships between water management, contamination and lifetime degradation in PEFC. J New Mater Electrochem Syst 2000;3(2):99-106.

[59] Trogadas P, Parrondo J, Ramani V. Degradation mitigation in polymer electrolyte membranes using cerium oxide as a regenerative free-radical scavenger. Electrochemical and Solid-State Letters 2008;11(7):B113-6.

[60] Coms FD, Liu H, Owejan JE. Mitigation of perfluorosulfonic acid membrane chemical degradation using cerium and manganese ions. ECS Transactions 2008;16(2):1735-47.

[61] Park J, Uddin MA, Ganesan S, Pasaogullari U, Bonville L, Molter T. Effects on wetting agents in cationic contamination and mitigation in PEFCs. ECS Transactions 2015;66(24):91-100.

[62] Das M. Understanding the effect of contaminants from BOP materials on PEMFC electrode: Ex-situ studies. Ph.D. Thesis. University of South Carolina 2013.

[63] O'Leary KA, Lakshmanan B, Budinski M. Methodologies for evaluating automotive PEM fuel cell system contaminants. Canada-US PEM Network Research Workshop February 16, 2009.

[64] Yu PT, Bonn EA, Lakshmanan B. Impact of structural plastics as balance of plant components on proton exchange membrane fuel cell performance. ECS Transactions 2013;58(1):665-80.

[65] Opu M, Bender G, Macomber CS, Van Zee JW, Dinh HN. Understanding the effects of PEMFC contamination from balance of plant assembly aids materials: In situ studies. J Electrochem Soc 2015;162(9):F1011-9.

[66] Ozdemir MO, Pasaogullari U. Modeling the oscillative behavior and carbon monoxide removal by current pulsing technique in $H_2$/CO mixtures for Pt catalyst layer. Int J Hydrogen Energy 2016;41(25):10854-69.

[67] U.S. Department of Energy. Fuel cell technologies office fuel cells fact sheet. November 2015. https://www.energy.gov/sites/prod/files/2015/11/f27/fcto_fuel_cells_fact_sheet.pdf.

[68] Sung W, Song Y, Yu K, Lim T. Recent advances in the development of Hyundai· Kia's fuel cell electric vehicles. SAE Int J Engines 2010;3(1):768-72.

**Table 1.1** Most common types of fuel cells and their properties [21,67].

| Type | Electrolyte/ Charge Carrier | Temperature ($^{o}$C) | Applications | Advantages |
|---|---|---|---|---|
| PEFC | Perfluorosulfonic acid / $H^+$ | <120 | • Backup and portable power<br>• On-site power generation<br>• Transportation and specialty vehicles | • Reduced corrosion and electrolyte management issues (solid electrolyte)<br>• Low temperature<br>• Quick start-up and loading |
| AFC | Aqueous KOH, or alkaline polymer membrane / $OH^-$ | <100 | • Backup power<br>• Transportation<br>• Military<br>• Space | • Lower cost components<br>• Low temperature<br>• Quick start-up |
| PAFC | $H_3PO_4$, or H3$PO_4$ in a polymer membrane / $H^+$ | 150-200 | • On-site power generation | • Suitable for combined heat and power (CHP)<br>• Tolerance to fuel impurities |
| MCFC | Molten lithium, sodium and potassium carbonates / $CO_3^{2-}$ | 600-700 | • Electric<br>• On-site power generation | • Fuel flexibility<br>• Suitable for CHP<br>• Hybrid/gas turbine cycle |
| SOFC | Yttria-stabilized zirconia / $O^{2-}$ | 500-1000 | • Electric<br>• Auxiliary<br>• On-site power generation | • Solid electrolyte<br>• Fuel flexibility<br>• Suitable for CHP<br>• Hybrid/gas turbine cycle |

**Table 1.2** Current status and U.S. DOE Targets for a hydrogen fuel cell (based on 80 kW (net) energy-producing transportation fuel cell power system) [21].

| **Characteristic** | **Unit** | **2015 Status** | **2020 Target** | **Ultimate Target** |
|---|---|---|---|---|
| Peak energy efficiency[a] | % | 60[b] | 65 | 70 |
| Cost[c] | $/kW$_{net}$ | 53 | 40 | 30 |
| Durability in automotive drive cycle[d] | hours | 3,900 | 5,000 | 8,000 |

[a] Ratio of DC output energy to the lower heating value of the hydrogen.

[b] From Ref. [68].

[c] Projected for the production of 500,000 systems/year.

[d] Based on 10% voltage degradation.

**Table 1.3** Comparison of 2015 costs and U.S. DOE 2020 targets for PEFC system, stack and their separate components[a,b] [31].

| Component | 2015 Status | 2020 Target |
|---|---|---|
| Overall PEFC System | 53 | 40 |
| PEFC stack | 26 | 20 |
| MEA[c] | 17 | 14 |
| Fuel cell membrane | 2.60 | 3.06 |
| Bipolar plates | 7 | 3 |
| Air compressor/expander/motor | 9.40 | 6.27 |
| Humidifier system | 1 | 1.23 |
| Humidifier membrane | 0.37 | 0.19 |

[a] Based on 80 kW (net) energy-producing transportation fuel cell power system.

[b] All units are in $\$/kW_{net}$.

[c] Membrane electrode assembly (MEA) includes membrane, CL, GDL and gaskets.

**Table 1.4** Types of PEFC degradation modes and their brief explanations (taken and organized from Ref. [25]).

| **Degradation modes** | **Mechanical** | **Chemical** |
|---|---|---|
| **Reversible** | • Tenting of GDL into the flow channels, causing poor electrical contact and more pressure drop.<br>• Flooding or dry-out due to bad water management.<br>• Fuel or oxidant starvation, causing voltage reversal.<br>• Dirt, sand or similar foreign materials in the air, blocking flow channels. | • Certain gas phase impurities (CO, dust, aerosols, alcohol vapors, $CO_2$, inert gases, hydrocarbon, nitrogen oxide, ammonia) absorb on the CL surface, reducing available Pt sites.<br>• Increase in the coolant conductivity by ionic impurities with time, causing electrical shorts. |
| **Irreversible** | • Plastic deformation of the GDL due to wrong/bad assembling.<br>• Electrolyte expansion or contraction with water content variation; then CL cracking.<br>• Electrolyte fracture with temperature or humidity cycling; causing hydrogen crossover.<br>• GDL hydrophobicity change, damaging water management.<br>• Pt sintering, dissolution and migration, Ostwald ripening, catalyst material oxidation, carbon corrosion, causing ECSA loss<br>• Pinhole formation on the electrolyte, leading to hydrogen crossover. | • Electrolyte loss by the peroxide radical attack [32], causing conductivity loss and pinhole formation.<br>• Pt dissolution and migration from PEFC cathode, resulting fewer active sites.<br>• Ionic impurities (e.g. $Ca^{2+}$, $Fe^{2+}$, $Cu^{2+}$, $Mg^{2+}$) from metallic components absorb on the membrane surface, reducing ionic conductivity and water transport.<br>• Oxidation of materials on the current collector, gaskets, hoses and fitting, damaging the proton conductivity, hydrophobicity and water management. |

**Table 1.5** Contaminants and their sources according to the literature [42,44-46].

| **Sources of contaminants** | **Contaminants** |
|---|---|
| Air (airborne contaminants) | $N_2$, $SO_2$, $SO_3$, NO, $NO_2$, $NH_3$ and $O_3$ |
| Hydrogen fuel source | CO, $CO_2$, $NH_3$, $CH_4$ and $H_2S$ |
| Battlefield | $SO_2$, $NO_2$, CO, HCN, CNCl, Sulfur Mustard, Sarin, benzene, propane |
| Compressor | Oils |
| Coolant | Si, Al, S, K, Cl, Cu, V, Cr and Fe |
| Sealing component | Si |
| Membranes (Nafion®) | $Na^+$, $Ca^{2+}$, $Cu^{2+}$, $Mg^{2+}$ and $Fe^{3+}$ |
| Bipolar plates (metallic) | $Cu^{2+}$, $Ni^{2+}$, $Cr^{3+}$ and $Fe^{3+}$ |
| System (BOP) components (structural plastics, lubricants, greases, sealants, adhesives and hoses) | Epoxy, silicone, urethane, and some polymers (fluoropolymers, polybutylene terephthalate (PBT), polyphthalamide (PPA), polyamide (PA), etc.) |

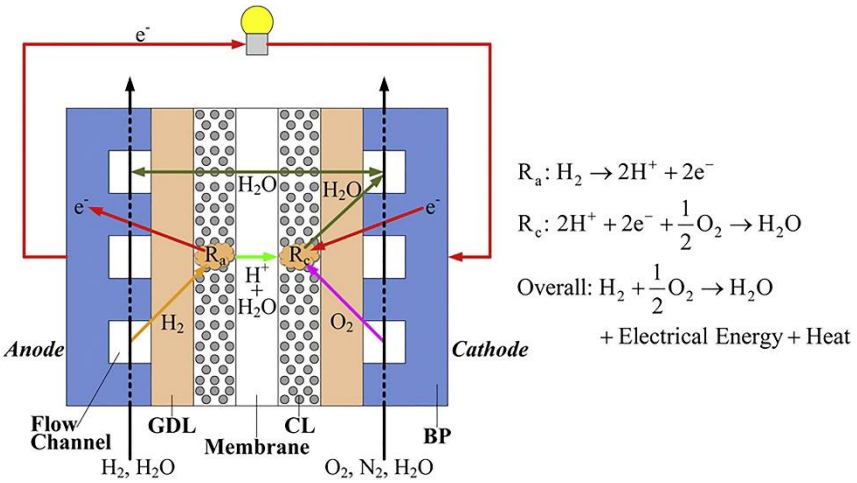


**Fig. 1.1** Schematic view for the operation and electrochemical reactions in a typical polymer electrolyte fuel cell (PEFC) ($R_a$, $R_c$: anode and cathode reactions, CL: catalyst layer, GDL: gas diffusion layer, BP: bipolar plates). From Ref. [23].

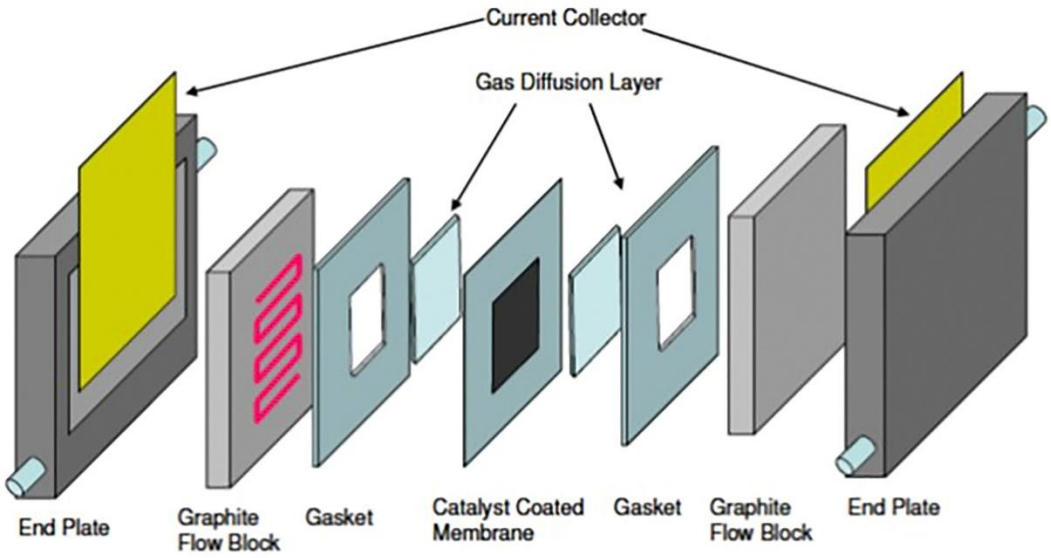


**Fig. 1.2** Components of a PEFC stack. From Ref. [24].

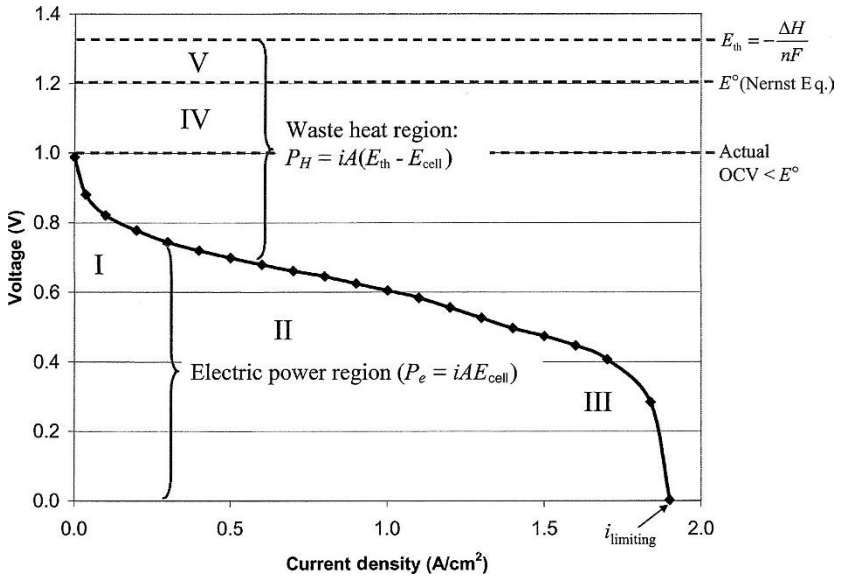


**Fig. 1.3** Typical polarization (I-V) curve for a PEFC. From Ref. [25].

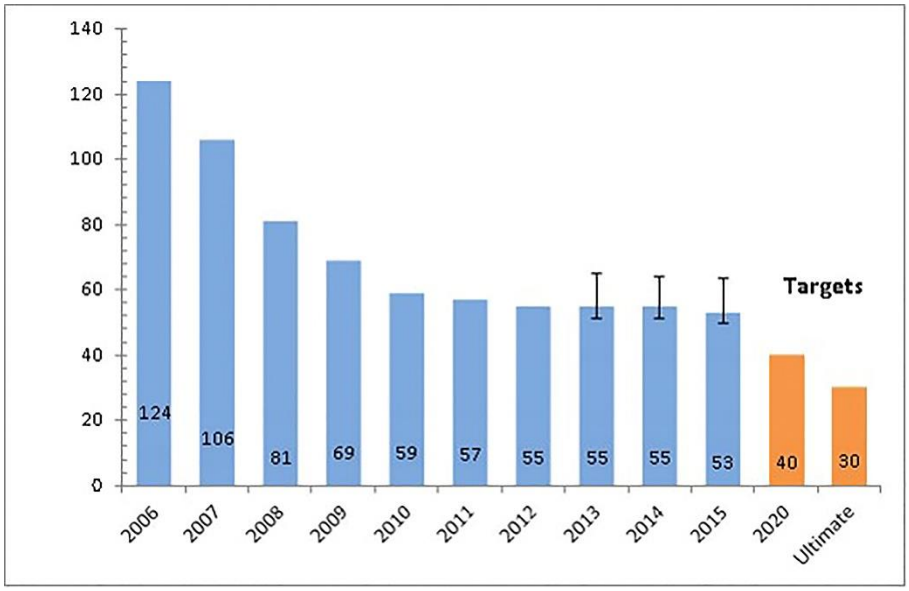


**Fig. 1.4** Trend in fuel cell system cost year by year with the 2020 and ultimate cost targets of U.S. Department of Energy (DOE). From Ref. [31].

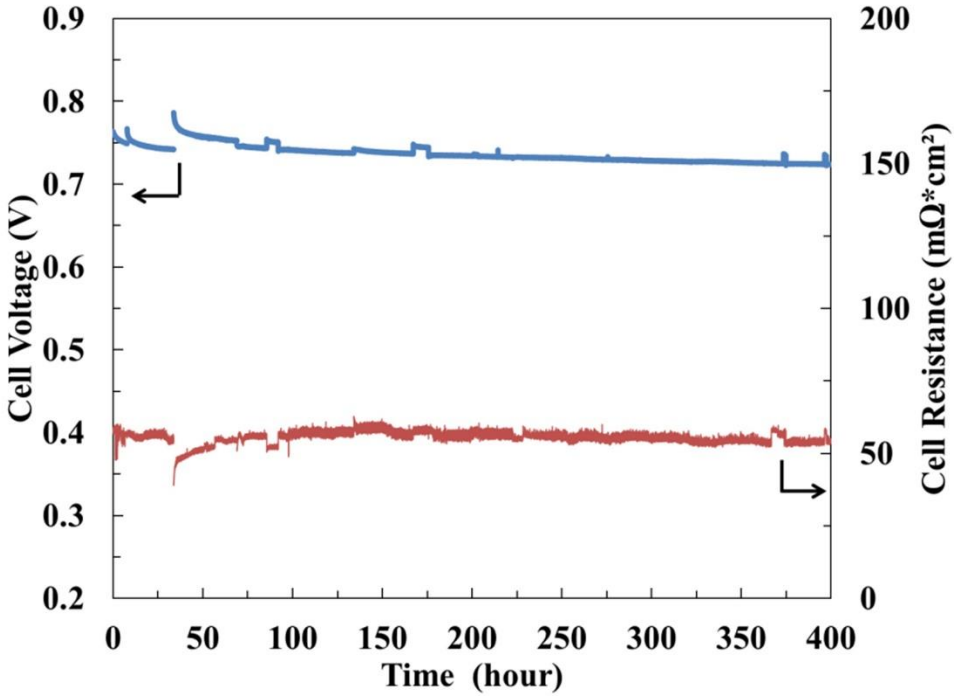


**Fig. 1.5** A typical galvanostatic test for a PEFC at 0.4 A/cm$^2$. Cell temperature: 80 ºC, $H_2$/air flow rate: 1.66/1.75 slpm, anode/cathode relative humidity: 25/125%, anode/cathode back pressure: 1.5/15 psig. From Ref. [34].

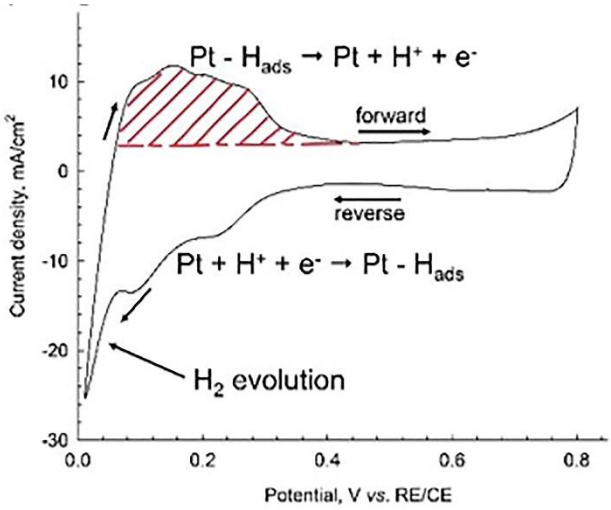


**Fig. 1.6** A typical cyclic voltammetry (CV) measurement for a PEFC. Scan rate: 40 mV/s, cell temperature: 35 ºC, anode/cathode relative humidity: 100/100%, anode/cathode pressure: 1/1 atm. Note that the shaded area is the total charge (μC/cm$^2$) for hydrogen desorption. Taken and modified from Ref. [37].

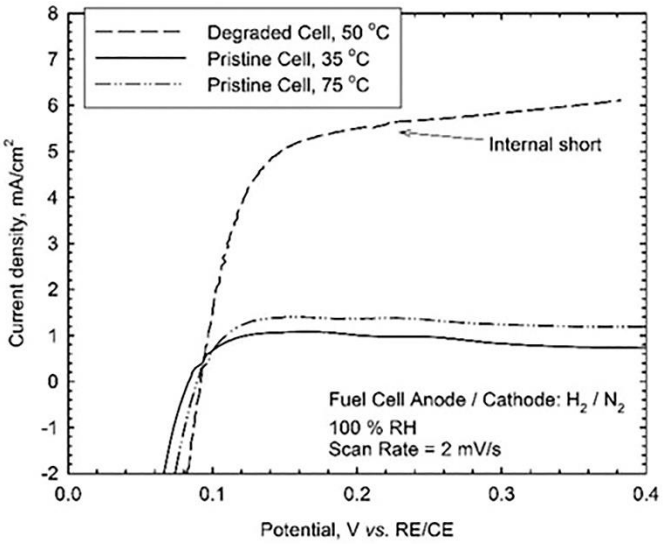


**Fig. 1.7** Linear sweep voltammetry (LSV) or $H_2$ crossover measurements for three cells, having different operating temperatures. Note that the degraded cell at 50 ºC exhibits the internal short. Taken from Ref. [39].

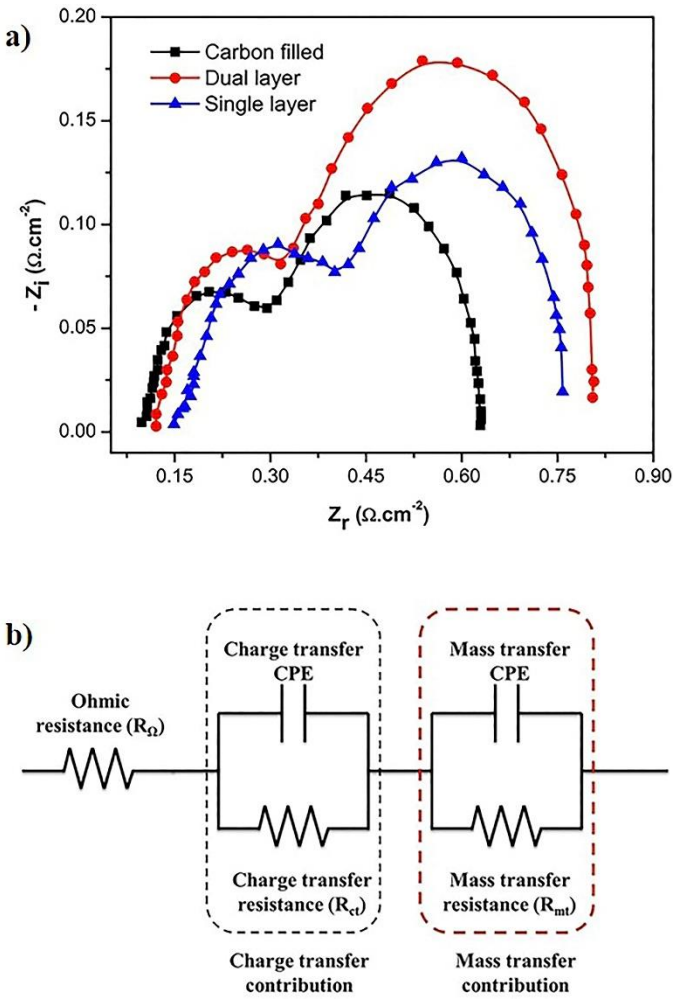


**Fig. 1.8 a)** Electrochemical impedance spectroscopy (EIS) measurement for a fuel cell with three different types of gas diffusion layers (GDLs). Anode/cathode flow: $H_2$/air, cell temperature: 60 ºC, anode/cathode relative humidity: 125/79%, anode/cathode pressure: 1.5/15 bar. From Refs. [40,41]. **b)** An equivalent electrical circuit model for the measurement in part a) or for typical EIS data in PEFCs [41].

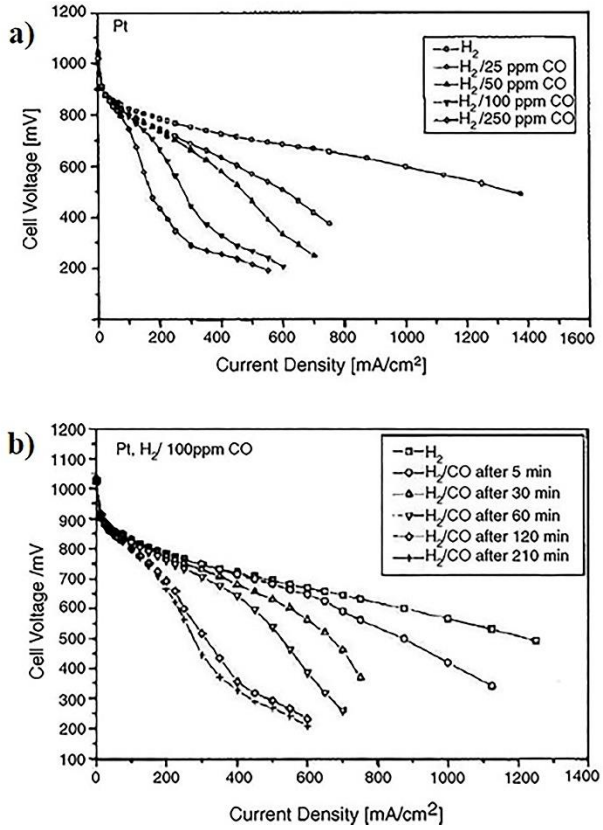


**Fig. 1.9 a)** Steady state effect of 0-250 ppm carbon monoxide (CO) for a PEFC operating with $H_2$ at anode and $CO/O_2$ mixture at cathode. **b)** Transient effect of carbon monoxide (CO) for a PEFC operating with $H_2$ at anode and 100 ppm $CO/O_2$ mixture at cathode. Cell temperature: 80 ºC, anode/cathode pressure: 0.22/0.24 MPa. Taken from Refs. [42,52].

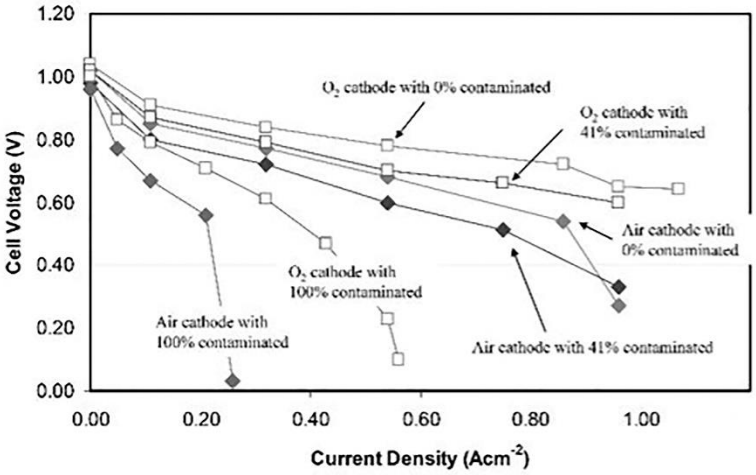


**Fig. 1.10** Effect of iron ($Fe^{3+}$) contamination on PEFC performance, which operates with $O_2$ or air at the cathode side. Anode (A)/cathode (C) stoichiometry: 2/1.5, A/C pressure: 3.04/3.04 atm, cell temperature: 80 ºC. Taken from Ref. [58].

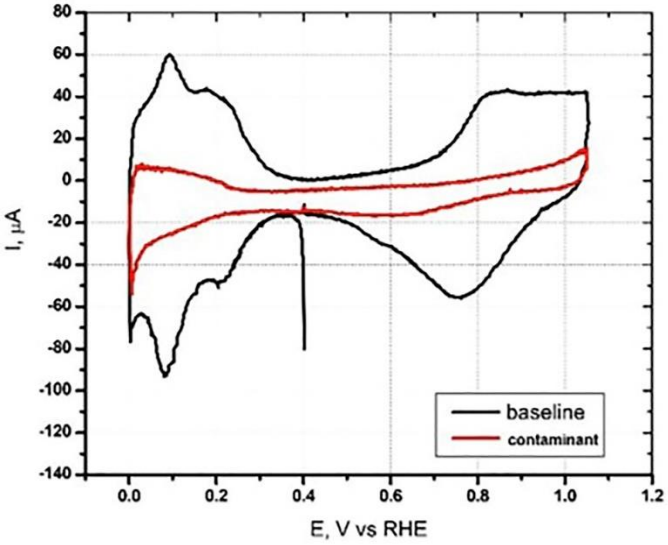


**Fig. 1.11** General Motors (GM) and National Renewable Energy Laboratory's (NREL) study [63] showing effect of BOP structural plastics on the Pt ECSA loss for a PEFC. From Ref. [62].

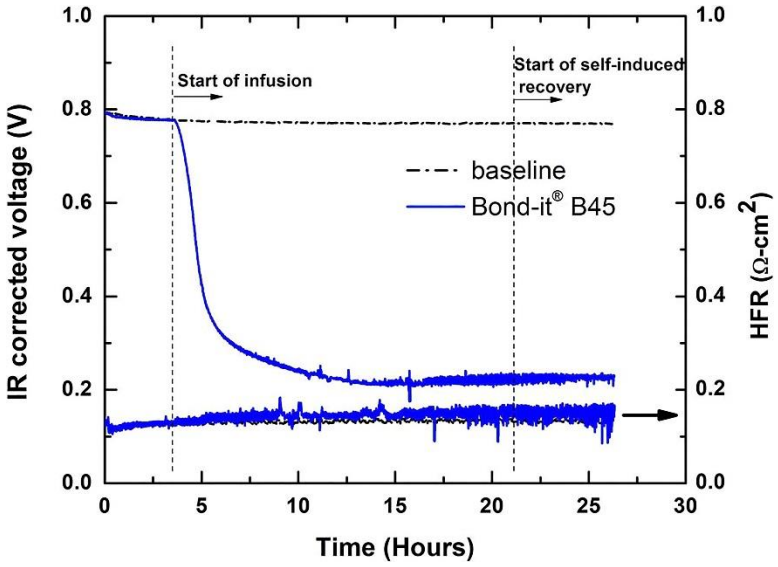


**Fig. 1.12** Current-hold test result to observe the effect of an epoxy leachate solution from Bond-it® B45 on PEFC performance. Contaminant solution is injected into the cathode inlet. Note that baseline condition means "no leachate solution", i.e. testing without any contamination. Cell temperature: 80 ºC, current density: 0.2 A/cm$^2$, A/C stoichiometry: 2/2, A/C pressure: 150/150 kPa, A/C relative humidity: 32/32%. From Ref. [65].

# Chapter 2 Investigation of Oscillative Behavior due to $H_2$/CO Mixtures in Pt Catalyst Layers (CLs)

## 2.1 Introduction

Hydrogen is an important fuel for several energy producing applications such as polymer electrolyte fuel cells (PEFCs). However, there are considerable challenges about storing and providing "pure" hydrogen as a fuel source due to its high volumetric density, very large space requirements and lack of natural source of "pure" hydrogen on earth [1]. For this reason, hydrogen is commonly generated with the process of steam reforming in practical applications, before it is fed into the fuel cell anode. However, impurities are usually present in this reformate either due to the feedstock or due to the process. It is indicated in earlier studies [2,3] that about 74% hydrogen ($H_2$), 25% carbon dioxide ($CO_2$), and 1-2 percent carbon monoxide (CO) are produced by the reformation of methanol, for example. Meanwhile, CO and $CO_2$ have been considered to be the impurities affecting PEFC operation and performance. Especially CO detrimentally affects the performance of PEFCs, and the mitigation techniques for this impurity have been studied in detail [4,5]. Tolerance limit of the fuel cell vehicles to the CO poisoning is determined to be at around 0.2 ppm level [6].

Besides the poisoning effect of CO, an interesting phenomenon is the oscillatory behavior of PEFCs operating with $H_2$/CO mixtures at the anode feed. Oscillations due to CO poisoning have been studied experimentally [7-22], numerically [18,20,21,23-32] and theoretically [19,33,34]. It has been discovered earlier that potential oscillations are triggered with $H_2$/CO mixtures on Pt and Pt/Ru surfaces [35-39]. CO is continuously adsorbed on the catalyst layer surface during the earlier stage of poisoning, and when the

cell is operated in constant current (galvanostatic) mode, anode overpotential increases in parallel due to increased CO coverage. When the anode potential reaches a critical value, OH forms on the catalyst surface [40]. Next, CO is electro-oxidized with the available OH species, consequently decreasing CO coverage and overpotential. As the overpotential is below certain value, OH cannot be formed on the surface and CO cannot be oxidized further. After this point, CO adsorption is again observed until overpotential is at the critical value. Repeat occurrence of this sequence in cycles is suggested to be the main reason for the oscillations at anode catalyst layer.

Most notable and preliminary studies about oscillations were carried out by Strasser et al. [8,26], and Zhang and Datta [25]. Strasser et al. [8,26] examined the potential oscillations during formic acid oxidation on Pt(100), Pt(110) and Pt(111) surfaces both experimentally [8] and numerically [26]. Their numerical method [26] considered only the kinetics of CO and OH adsorption and electro-oxidation on Pt particles, and did not include the PEFC environment and the catalyst layer. Moreover, the dynamics of oscillations in PEFC anode CL with Pt/Ru catalyst was numerically investigated by Zhang and Datta [25] in zero dimension without the diffusion of species. An interesting outcome from the corresponding efforts [8,25,26] is that the oscillations disappear when the electrode potential is kept constant, i.e. in potentiostatic mode. Several authors extended Zhang and Datta's model [25] in order to design of ECPROX [23,24], to investigate the oscillation patterns along the anode channel [28,29], and to observe the oscillation kinetics for non-alloyed Pt surfaces [30]. Malkhandi et al. [18] performed a non-dimensional mechanistic study to observe the effect of anions on the oscillative behavior during CO electro-oxidation. Only surface kinetics on Pt were included in their model [18]. Similarly, voltage

oscillations were also modeled for formic acid [20,32] and methanol [21] oxidation on Pt and Pt-alloys using non-dimensional surface kinetics. Other research efforts about the instabilities and the oscillations due to the presence of CO on CL surfaces can be reviewed elsewhere [37-39].

The review of the literature reveals that previous numerical models were significantly simplified, e.g. the diffusion of species through anode CL, and especially the distribution of surface coverages within the CL thickness during oscillations were not considered in any numerical model. In this chapter, a one-dimensional transient model has been developed to describe the CO poisoning mechanism in catalyst layer with Pt particles. Diffusion of $H_2$ and CO along the CL thickness has been considered, and special attention has been placed on prediction of the variation of adsorbed hydrogen, carbon monoxide and hydroxyl coverages within the CL. Voltage oscillations have been observed for 1,000 ppm CO level in the anode fuel, and explained in detail. In the next sections, the development of the model is described with details on reaction kinetics, followed by the discussion of results.

## 2.2 Model development

### 2.2.1 Reaction Kinetics

When $H_2$ and CO are provided together through the Pt catalyst layer, the overall reaction mechanism is simplified in four steps: $H_2$ adsorption, $H_2$ electro-oxidation, CO adsorption and CO electro-oxidation. Although the reactions appear to be simple, there has been a variation in how the electro-oxidation of CO is described. It has been assumed by many researchers [41-46] that CO can be simply oxidized with the water vapor, however at the

high CO concentrations (as high as 0.1-1%) considered in this study, high anode overpotentials are expected and adsorbed OH molecules can be observed on Pt surfaces at potentials above ~0.5 V [40,47]. Therefore, in this work we consider that CO is oxidized with adsorbed OH molecules.

$H_2$ adsorption and oxidation are defined, respectively, with the following reactions:

$$H_2 + 2Pt \underset{k_{h,d}}{\overset{k_{h,a}}{\rightleftharpoons}} 2\,(H - Pt) \tag{1}$$

$$H - Pt \overset{k_{h,ox}}{\rightharpoonup} Pt + H^+ + e^- \tag{2}$$

Meanwhile, adsorption/oxidation of CO can be illustrated as shown below [48-50]:

$$CO + Pt \underset{k_{co,d}}{\overset{k_{co,a}}{\rightleftharpoons}} CO - Pt \quad . \tag{3}$$

$$(CO - Pt) + (OH - Pt) \overset{k_{co,ox}}{\rightharpoonup} CO_2 + 2Pt + H^+ + e^- \tag{4}$$

where the adsorbed OH molecules, OH-Pt, are produced from the water adsorption on Pt [51,52]:

$$H_2O + Pt \underset{k_{w,d}}{\overset{k_{w,a}}{\rightleftharpoons}} (OH - Pt) + H^+ + e^- \tag{5}$$

Note that $k_{h,a}$, $k_{h,d}$ and $k_{h,ox}$ are, respectively, the adsorption and desorption rate constants, and electro-oxidation rate constant for hydrogen. Similarly, $k_{co,a}$, $k_{co,d}$ and $k_{co,ox}$ are, respectively, the adsorption and desorption rate constants, and electro-oxidation rate

constant for carbon monoxide. In addition, $k_{w,a}$ and $k_{w,d}$ are the adsorption and desorption rate constants for hydroxyl.

### 2.2.2 Model and governing equations

A schematic view of the modeling domain is shown in Figure 2.1. The coordinate, x-axis, through the catalyst layer, and the left (gas diffusion layer) and right (polymer electrolyte membrane) boundaries are clearly indicated in the corresponding figure.

Certain assumptions have been implemented in our numerical solution in order to simplify the procedure. Basic assumptions in the numerical calculations can be summarized as follows:

1) The model is one-dimensional, i.e. species and charge transports in-plane catalyst layer (y and z planes) have been neglected.
2) Diffusion is the only mechanism for the species transport in x-direction. Convection effects are not included.
3) Reaction (4) is assumed to be irreversible [25].
4) $H_2$ and CO concentrations at GDL-CL interface are assumed to be equal to those at the inlet fuel.
5) Water vapor concentration and ionomer water content are constant along the CL.
6) The modeling domain is isothermal and isobaric.

Mathematical description of the following physical phenomena are included in the model: i) surface kinetics of coverages, ii) species transport, and iii) balance of ionic and electronic charge.

### *2.2.2.1 Surface kinetics in CL (Balance of H, CO and OH coverages on Pt)*

Balance or the time evolution of the adsorbed molecules can be performed with adsorption/desorption and electro-oxidation rates for each species. Net adsorption rates for $H_2$, CO and water vapor on Pt catalyst can be explained, respectively, as below [25]:

$$r_{h,a} = k_{h,a}\, P_a\, \frac{C_H}{C_H+C_{CO}+C_w}\, (1 - \theta_h - \theta_{co} - \theta_{oh})^2 - k_{h,a}\, k_{h,d}\, {\theta_h}^2 \quad (6)$$

$$r_{co,a} = k_{co,a}\, P_a\, \frac{C_{CO}}{C_H+C_{CO}+C_w}\, (1 - \theta_h - \theta_{co} - \theta_{oh}) - k_{co,a}\, k_{co,d}\, \theta_{co} \quad (7)$$

$$r_{oh,a} = k_{w,a}\, (1 - \theta_h - \theta_{co} - \theta_{oh})\, \exp(\frac{\alpha F}{R_u T}\, \eta_a) - k_{w,d}\, \theta_{oh}\, \exp(-\frac{\alpha F}{R_u T}\, \eta_a) \quad (8)$$

where $P_a$ is the anode pressure, $\alpha$ is the transfer coefficient, T is the temperature, F is the Faraday's constant, $R_u$ is the universal gas constant, $\eta_a$ is the anode overpotential, $\theta_h$, $\theta_{co}$ and $\theta_{oh}$ are, respectively, surface coverages of adsorbed H, CO and OH, and $C_H$, $C_{CO}$ and $C_w$ are the species concentrations of $H_2$, CO and water vapor. Note that $C_w$ is equal to the inlet water vapor concentration, $C_{w,i}$, and calculated by:

$$C_w = C_{w,i} = \phi_a\, \frac{P_{sat}}{R_u T} \quad (9)$$

where $\phi_a$ is the anode relative humidity and $P_{sat}$ is the saturation pressure of water vapor at temperature, T.

In addition to the net adsorption rates given above, $H_2$ electro-oxidation, reaction (2), is assumed to have symmetric transfer coefficient in forward and reverse directions [25,41]. Meanwhile, Tafel kinetics is assumed for CO electro-oxidation, reaction (4) [25,26]. Thus, electro-oxidation rates of $H_2$ and CO can be defined, respectively, with the following expressions:

$$r_{h,ox} = 2\, k_{h,ox}\, \theta_h \sinh\left(\frac{\alpha F}{R_u T}\, \eta_a\right) \tag{10}$$

$$r_{co,ox} = k_{co,ox}\, \theta_{co}\, \theta_{oh} \exp\left(\frac{\alpha F}{R_u T}\, \eta_a\right) \tag{11}$$

Finally, balance of the coverages along the catalyst layer can be expressed with the equations below:

$$(F\gamma C_t)\, \frac{\partial \theta_h}{\partial t} = r_{h,a} - r_{h,ox} \tag{12}$$

$$(F\gamma C_t)\, \frac{\partial \theta_{co}}{\partial t} = r_{co,a} - r_{co,ox} \tag{13}$$

$$(F\gamma C_t)\, \frac{\partial \theta_{oh}}{\partial t} = r_{oh,a} - r_{co,ox} \tag{14}$$

for H, CO and OH, respectively. Note that $\gamma$ is the surface roughness factor, and $C_t$ is the molar area density of the catalyst layer.

#### *2.2.2.2 Species transport in CL*

The required equations for the species transports are given as:

$$\varepsilon_c\, \frac{\partial C_H}{\partial t} = D_H^{eff}\, \frac{\partial^2 C_H}{\partial x^2} - \frac{A_v}{2F}\, r_{h,a} \tag{15}$$

$$\varepsilon_c\, \frac{\partial C_{CO}}{\partial t} = D_{CO}^{eff}\, \frac{\partial^2 C_{CO}}{\partial x^2} - \frac{A_v}{F}\, r_{co,a} \tag{16}$$

where $\varepsilon_c$ is the porosity, and $A_v$ is the specific electro-active surface area of the CL. $D_H^{eff}$ and $D_{CO}^{eff}$ are the effective diffusion coefficients of $H_2$ and CO, respectively, which are expressed by [45,53,54]:

$$D_H^{eff} = D_{H,o} \, (\varepsilon_c)^{1.5} \left(\frac{T}{T_{ref}}\right)^{1.5} \left(\frac{P_{ref}}{P_a}\right) \quad (17)$$

$$D_{CO}^{eff} = D_{CO,o} \, (\varepsilon_c)^{1.5} \left(\frac{T}{T_{ref}}\right)^{1.5} \left(\frac{P_{ref}}{P_a}\right) \quad (18)$$

in which, $D_{H,o}$ and $D_{CO,o}$ are, in order, the diffusion coefficients of $H_2$ and CO at reference temperature, $T_{ref}$, and reference pressure, $P_{ref}$.

#### *2.2.2.3 Conservation of ionic and electronic charge*

Conservation of electronic and ionic charges within the CL thickness can be formulized with equations (19) and (20), respectively:

$$-\sigma_s^{eff} \frac{d^2V_s}{dx^2} = -A_v \left(r_{h,ox} + r_{co,ox} + r_{oh,a}\right) \quad (19)$$

$$-\sigma_i^{eff} \frac{d^2V_i}{dx^2} = A_v \left(r_{h,ox} + r_{co,ox} + r_{oh,a}\right) \quad (20)$$

where $\sigma_s^{eff}$ is the electronic (solid phase) conductivity, and $\sigma_i^{eff}$ is the ionic phase conductivity of the catalyst layer, which have been corrected for the porosity [54]. $V_s$ and $V_i$ are the solid and ionic phase potentials.

Overpotential along the CL, $\eta_a$, can be described by the following equation:

$$\eta_a = V_s - V_i \quad (21)$$

#### *2.2.2.4 Initial and boundary conditions*

It is required to define the initial and boundary conditions within the modeling domain, as illustrated in Figure 2.1, in order to solve the equations (6)-(21). While the initial conditions

are defined at time t=0, the boundary conditions are given at GDL-CL and CL-PEM interfaces.

The conditions at the GDL-CL boundary are considered to have a fixed species concentration (referred to assumption #4), and ground (zero) electronic potential. Moreover, the corresponding interface is ionically insulated; therefore, there is no flux of protons between GDL and CL. Coverages of adsorbed molecules are only defined in the catalyst layer. Hence, same condition (insulated or no flux) is also specified for the coverages at this interface. Consequently, boundary conditions at GDL-CL can be expressed with the equations below:

$$C_{CO}(x=0, t) = y_{CO,i} \frac{P_a}{R_u T} \tag{22}$$

$$C_H(x=0, t) = (1 - y_{CO,i} - y_{w,i}) \frac{P_a}{R_u T} \tag{23}$$

$$V_s(x=0, t) = 0 \tag{24}$$

$$\sigma_i^{eff} \left.\frac{dV_i}{dx}\right|_{x=0,t} = 0 \tag{25}$$

$$\left.\frac{\partial \theta_h}{\partial x}\right|_{x=0,t} = \left.\frac{\partial \theta_{co}}{\partial x}\right|_{x=0,t} = \left.\frac{\partial \theta_{oh}}{\partial x}\right|_{x=0,t} = 0 \tag{26}$$

where $y_{CO,i}$ and $y_{w,i}$ are the molar fractions of CO and water vapor at the inlet fuel. Molar fraction of CO at the inlet, $y_{CO,i}$, is given as an input in our model. It should also be mentioned that molar fraction of water vapor can be derived from the following relation:

$$y_{w,i} = \phi_a \frac{P_{sat}}{P_a} \tag{27}$$

CL-PEM interface is assumed not to permit the transport of non-adsorbed species. Similarly, no flux of electrons is considered at this interface. Meanwhile, flux of protons (ionic charge) is given as an input of fixed current density, J, through the plane between CL and PEM. In addition, it should be recalled that coverages of adsorbed species only exist at catalyst layer. Thus, the conditions at the right boundary of CL can be summarized as follows:

$$D_H^{eff} \left.\frac{\partial C_H}{\partial x}\right|_{x=l_c,t} = D_{CO}^{eff} \left.\frac{\partial C_{CO}}{\partial x}\right|_{x=l_c,t} = 0 \tag{28}$$

$$\sigma_s^{eff} \left.\frac{dV_s}{dx}\right|_{x=l_c,t} = 0 \tag{29}$$

$$-\sigma_i^{eff} \left.\frac{dV_i}{dx}\right|_{x=l_c,t} = J \tag{30}$$

$$\left.\frac{\partial \theta_h}{\partial x}\right|_{x=l_c,t} = \left.\frac{\partial \theta_{co}}{\partial x}\right|_{x=l_c,t} = \left.\frac{\partial \theta_{oh}}{\partial x}\right|_{x=l_c,t} = 0 \tag{31}$$

Finally, the initial values for adsorbed molecules and non-adsorbed species should be defined. The coverages of adsorbed molecules, θ, are assumed to be zero (no surface coverage) initially. Additionally, the concentrations of non-adsorbed species, C, are considered to be equal to those at the inlet or GDL-CL interface at t=0. The defined initial conditions can be numerically explained with the equations below:

$$C_{CO}(x, t=0) = y_{CO,i} \frac{P_a}{R_u T} \quad (32)$$

$$C_H(x, t=0) = (1 - y_{CO,i} - y_{w,i}) \frac{P_a}{R_u T} \quad (33)$$

$$\theta_h(x, t=0) = \theta_{co}(x, t=0) = \theta_{oh}(x, t=0) = 0 \quad (34)$$

### 2.3 Numerical method

Equations (6)-(21) have been solved with the software Comsol Multiphysics Version 4.3a [55] using the Galerkin finite element method (FEM) [56,57], which has improved stability in non-linear time-dependent equations. Time discretization is achieved by backward differentiation formula (BDF) [58-61]. While the time steps have been controlled and adapted by the software to stabilize the solution, maximum time steps have been set by the user. The initial stage of CO poisoning and period of oscillations have been observed with relatively smaller maximum time steps for improved accuracy and resolution. For the solution of 1,000 ppm CO contaminant, maximum time steps are 0.1 s, 1 ms, and 1 s at the initial stage of poisoning ($t < 30$ s), during the oscillations ($t > 124$ s), and at the intervening period, respectively. Mesh is refined with small elements along the domain for numerical consistency. Modeling domain, shown in Figure 2.1, has been discretized by 1,000 mesh elements. Element sizes are the same and constant throughout the CL thickness for simplicity; thickness of one grid is $l_{cl}/1000$. Finally, relative and absolute error tolerances are, respectively, $10^{-4}$ and $10^{-5}$ during the numerical solution.

### 2.4 Results and discussion

Diffusion coefficients, reaction rate constants, conductivities and other parameters in the numerical model are listed in Table 2.1. Diffusion coefficient of $H_2$ is corrected with a

simple analysis similar to the one in Farrell et al.'s study [62]. Anode overpotential vs. current density is calculated for two different cases in Figure 2.2, with and without species diffusion, using no CO contamination at the catalyst layer. There should not be any difference between two curves since there is no appreciable mass transfer effect until ~0.4 $A/cm^2$ in a PEFC operation. In fact, the two curves almost match each other, as indicated in Figure 2.2. Hence, the selected $H_2$ diffusivity is reasonable in our case. Moreover, studies in literature [41,45] indicate that CO diffusivity is around 3 times smaller than $H_2$ diffusivity. Thus, both diffusivities in Table 2.1 are listed accordingly.

All of the reaction rate constants except the adsorption rate constants are selected exactly as it is from the given references in Table 2.1. Adsorption rate constants are fitted during the model validation step in section 4.1, and determined to be very close to the parameters used in the reference papers in Table 2.1. Assumptions and the properties of our modeling domain (e.g. Pt catalyst) are considered at all stages.

Modeling results for the "1000 ppm CO contamination in $H_2$" are presented in two sections below. First, our model is validated for 100 ppm CO at the anode feed with the existing experimental data in literature. Next, results from 1,000 ppm CO poisoning are discussed in detail. Oscillations in the performance and the surface coverages were seen in the modeling for 1,000 ppm CO. Therefore, poisoning results are introduced with an in-depth explanation of oscillations. It should be noted at this point that current density is kept constant at J=0.1 $A/cm^2$, as already presented in Table 2.1.

### 2.4.1 Model validation

In this part, the numerical model is run with constant anode overpotential mode in order to avoid the oscillations. Accordingly, boundary condition (equation (30)) is modified to be $V_i = -\eta$, in which anode overpotential, $\eta$, is known and given as an input. Other initial and boundary conditions (equations (22)-(29) and (31)-(34)) are unchanged. In addition, cell temperature is maintained at 358 K. All parameters other than cell temperature remain the same as in Table 2.1. Along with the given conditions, the equations (6)-(21) have been solved for 100 ppm CO in $H_2$ ($y_{CO,i} = 0.0001$) for the validation. Transient (time dependent) solution is obtained for 100 ppm CO at different anode overpotentials until the steady state.

Comparison of the current model with the experimental data from Lee et al. [63], Pereira et al. [89] and Rocha et al. [90] can be seen in Figure 2.3. Anode overpotential versus the current density at steady state is shown for 100 ppm CO in the corresponding figure. It can be concluded from Figure 2.3 that the results from the current model appear to agree with Lee et al.'s data [63] except for the overpotential range of 0.2-0.4 V. As mentioned earlier, adsorbed OH molecules on Pt are expected to accumulate at the anode overpotential higher than ~0.5 V [40]. Hence, the electro-oxidation of CO with adsorbed OH can be anticipated above 0.5 V. However, CO on Pt may still be oxidized at some extent with water molecules below this potential. The corresponding reaction can be expressed as below:

$$(\mathrm{CO\text{ - }Pt}) + \mathrm{H_2O} \rightarrow \mathrm{CO_2} + \mathrm{Pt} + 2\mathrm{H^+} + 2\mathrm{e^-} \qquad (35)$$

In consequence, overpotential due to CO poisoning is diminished between 0.2-0.4 V with the oxidation above. The difference between the current model and the data from

Lee et al.'s study [63] at this region in Figure 2.3 can be attributed to reaction (35). It has been already indicated that reaction (4) is considered to be the only mechanism in the current approach for the CO electro-oxidization instead of the coupled impact of reactions (4) and (35). However, this assumption can be justified since the main purpose of this research is to investigate the effect of high levels of CO poisoning (up to 0.1-1% CO) by which the anode overpotential higher than 0.5 V is anticipated. Therefore, it is implied from Figure 2.3 that the suggested model is validated with the existing experimental results from Ref. [63] in the conditions of interest.

Besides the comparison with Lee et al.'s experiments [63], results from the current model are similar to the trend in overpotential data from Pereira et al. [64] and Rocha et al. [65] for 100 ppm CO level, as seen in Figure 2.3. Those data are not very close to our study since there are slight differences from Lee et al.'s experiments [63] in operating conditions and materials. For example, Pereira et al. [64] performed their study at 2 atm anode pressure (1 atm in Ref. [63]), and Rocha et al. [65] maintained the cell temperature at 353 K (358 K in Ref. [63]) with 0.5 mg/cm$^2$ Pt loading at anode catalyst layer (0.4 mg/cm$^2$ in Ref. [63]). Note higher anode pressure decreases the anode overpotential loss, and lower cell temperature increases the anode overpotential during CO poisoning [42].

### 2.4.2 Oscillatory behavior with 1,000 ppm CO poisoning

This section provides the solution of the governing equations (equations (6)-(21)) for 1,000 ppm CO in $H_2$ ($y_{CO,i}$ = 0.001) with Figures 2.4-2.8. Current density, J = 0.1 A/cm$^2$, is kept constant during the solution. To start with, CO and H coverages throughout the anode CL are shown in Figure 2.4. Initial coverages of adsorbed species are assumed to be zero at CL. For this reason, time scale in Figure 2.4 starts with 0.5 s for simplicity. Figure 2.4a

indicates that GDL-CL interface is covered by 97% carbon monoxide in less than 2 s. However, penetration of CO coverage towards the CL-PEM interface is observed to be slower due to the faster diffusion of hydrogen through the anode CL. Hence, surface close to the CL-PEM interface is initially covered with hydrogen, as illustrated in Figure 2.4b. As carbon monoxide diffuses through the CL, adsorbed hydrogen on Pt is replaced by the adsorbed carbon monoxide. At time t = ~125 s, 90% of the CL-PEM interface is covered by CO. Just after the corresponding time is reached, the oscillations in the species coverages commence. Even during the oscillations, the CO coverage at CL-PEM interface is shown to increase in Figure 2.4a. After 8-9 seconds, a steady-state oscillating condition is reached and maximum and minimum coverages during oscillations are fixed after time, t=~133 s.

It should be emphasized that OH coverage has not been included in Figure 2.4 since it is very low level (~$10^{-10}$) until time, t=125 s, where the high anode potential (~0.65 V, due to the complete CO coverage) is established. Accordingly, hydroxyl species start to be formed on Pt surface at this point, which is followed with the oscillations. As evidenced by Figure 2.5, an exponential increase in anode overpotential is noticed while the CL is covered with CO. However, the critical anode overpotential, 0.65 V, for 1,000 ppm CO is eventually achieved at t=125 s. Next, oscillations in overpotential between 0.18 and 0.65 V are detected, as presented in the detailed view of Figure 2.5.

In order to further understand the mechanism, coverages of species have been averaged along the catalyst layer length, and provided in Figure 2.6 during the oscillations. Figure 2.6c shows that a steep accumulation of adsorbed OH (OH-Pt) is reached at the critical potential, as mentioned previously in Figure 2.5. Subsequently, Reaction (4),

electro-oxidation of CO is anticipated, by which CO and OH coverages are reduced in Figures 2.6a and 2.6c. Therefore, a sharp sudden increase in hydrogen coverage is seen in Figure 2.6b. The decrease in anode overpotential from 0.65 V to 0.18 V, in Figure 2.5, can also be interpreted with the same phenomenon. Nevertheless, following the consumption of adsorbed OH with reaction (4), adsorbed CO (CO-Pt) is replenished in the catalyst layer. Therefore, adsorbed H is again replaced with the carbon monoxide, which leads to the loss in H coverage, as witnessed in Figure 2.6b. As a consequence, anode overpotential increases again to 0.65 V in Figure 2.5. Oscillative behavior is revealed as the repeated occurrence of this whole mechanism. At this point, there is another interesting fact that the change in surface coverages is only minimal while the voltage oscillations occur within a considerable interval. This means that oscillations in surface coverages should be more related to current density instead of the cell voltage. This phenomenon can also be supported in Figure 2.8, later in this study.

As referred previously, oscillations in the overpotential and the coverages have been found to begin at t = 125 s, and steady oscillations have been achieved at around t = 133 s. One-dimensional views, indicating the maximum point of surface coverages during oscillations along the anode CL length, are presented, in order, for CO, H and OH in Figures 2.7a-c. Three data points of time have been selected in these figures; representing the beginning, steady state point of oscillations, and a transition point from the beginning and steady state condition. An interesting outcome from Figure 2.7a is that while there is an increase in CO coverage close to the CL-PEM interface, a decreasing behavior in adsorbed CO can be seen in the middle region of CL, and close to the GDL-CL interface. On the contrary, the opposite trend can be concluded for H and OH coverages from Figures

2.7b-c. The main reason for this condition is that the CO diffusion through CL and the penetration of adsorbed CO, as already known from Figure 2.4a, are still continuing and are incomplete near the PEM interface at the beginning of oscillations. Hence, the overpotential is high enough to overcome the diffusion effect, and to oxidize the small amount of adsorbed CO near the GDL interface. In contrast, the diffusion of CO is more dominant over the anode overpotential near the PEM interface. Thus, even during the oscillations, there is still an increase in the CO coverage near the CL-PEM interface. Similar situation to Figure 2.7, and not shown here, has also been observed for the minimum points during coverage oscillations. In addition, the maximum and minimum CO coverages throughout the CL at steady state are shown in Figure 2.7d. It can be demonstrated in this figure that anode CL is eventually covered with ~99% and ~94% adsorbed CO at GDL and PEM interfaces, respectively.

Current densities due to the proton ($H^+$) generation from each electrochemical oxidation and hydroxyl adsorption reaction are given in Figure 2.8. As seen in Figures 2.8a and 2.8b, a decrease in $H_2$ current density ($H^+$ generation from reaction (2)) is observed as the adsorbed OH (reaction (5)) is formed on Pt surface, hence a higher OH current density can be achieved, followed by an increase in CO current density generation from reaction (4) as adsorbed OH is available. However, CO electro-oxidation rate is much slower below ~0.5 V, required for the formation of adsorbed OH. Meanwhile, decrease in OH current density (reaction (5)) is sharper than that in CO current density (reaction (4)) due to the fact that negligible adsorbed hydroxyl ($10^{-10}$) remains on Pt surface at potentials less than 0.5 V. Another interesting fact is that unused adsorbed OH in the CL is instantaneously converted to water by desorption (recall reaction (5)), as the anode

overpotential becomes lower than the certain limit. As a consequence, a negative OH current density, i.e. $H^+$ consumption, cannot be avoided at the region of decreasing anode overpotential during oscillations. Accordingly, CO oxidation has a peak at ~20 $A/m^2$ in Figure 2.8b, and then starts to decrease due to the rapid consumption of adsorbed OH within the CL. In the meantime, $H_2$ current density becomes higher than 0.1 $A/cm^2$, as the total current density, 0.1 $A/cm^2$, is still maintained. Finally, while $H_2$ current density is again lowered to 0.1 $A/cm^2$, CO and OH current densities are seen to approach to zero at the end of a single oscillation.

## 2.5 Conclusion

One-dimensional kinetics of 1,000 ppm CO poisoning at Pt catalyst layer with the fuel of $H_2$/CO mixture have been analyzed numerically. Oscillations in anode overpotential and species coverages are detected, and examined in detail across the length of the catalyst layer. It has been shown that the oscillations are mainly caused by the formation of the adsorbed OH molecules on Pt sites, CO electro-oxidization with the formed OH molecules, and the diffusion of species from GDL to PEM interface.

## 2.6 References

[1] Aceves SM, Berry GD. Thermodynamics of insulated pressure vessels for vehicular hydrogen storage. Journal of energy resources technology 1998;120(2):137-42.

[2] Brown LF. A comparative study of fuels for on-board hydrogen production for fuel-cell-powered automobiles. Int J Hydrogen Energy 2001;26(4):381-97.

[3] Divisek J, Oetjen H, Peinecke V, Schmidt V, Stimming U. Components for PEM fuel cell systems using hydrogen and CO containing fuels. Electrochim Acta 1998;43(24):3811-5.

[4] Zamel N, Li X. Effect of contaminants on polymer electrolyte membrane fuel cells. Progress in Energy and Combustion Science 2011;37(3):292-329.

[5] Liu Z. Effects of fuel and air impurities on PEFC performance. Polymer Electrolyte Fuel Cells: Science, Applications, and Challenges 2013:427.

[6] Fuel Cell Standards Committee. Information Report on the Development of a Hydrogen Quality Guideline for Fuel Cell Vehicles, SAE, J2719. International Organization for Standardization, Hydrogen Fuel–Product Specification–Part 2:14687-2.

[7] Zhang J, Datta R. Electrochemical preferential oxidation of CO in reformate. J Electrochem Soc. 2005;152(6):A1180-7.

[8] Strasser P, Lübke M, Raspel F, Eiswirth M, Ertl G. Oscillatory instabilities during formic acid oxidation on Pt (100), Pt (110) and Pt (111) under potentiostatic control. I. Experimental. J Chem Phys 1997;107(3):979-90.

[9] Zhang J, Datta R. Higher power output in a PEMFC operating under autonomous oscillatory conditions in the presence of CO. Electrochemical and solid-state letters 2004;7(3):A37-40.

[10] Tingelöf T, Hedström L, Holmström N, Alvfors P, Lindbergh G. The influence of CO2, CO and air bleed on the current distribution of a polymer electrolyte fuel cell. Int J Hydrogen Energy 2008;33(8):2064-72.

[11] Lu H, Rihko-Struckmann L, Hanke-Rauschenbach R, Sundmacher K. Dynamic behavior of a PEM fuel cell during electrochemical CO oxidation on a PtRu anode. Topics in Catalysis 2008;51(1-4):89-97.

[12] Mota A, Lopes P, Ticianelli E, Gonzalez E, Varela H. Complex oscillatory response of a PEM fuel cell fed with H2/CO and oxygen. J Electrochem Soc 2010;157(9):B1301-4.

[13] Lopes PP, Ticianelli EA. The CO tolerance pathways on the Pt–Ru electrocatalytic system. J Electroanal Chem 2010;644(2):110-6.

[14] Lopes PP, Ticianelli EA, Varela H. Potential oscillations in a proton exchange membrane fuel cell with a Pd–Pt/C anode. J Power Sources 2011;196(1):84-9.

[15] Lu H, Rihko-Struckmann L, Sundmacher K. Spontaneous oscillations of cell voltage, power density, and anode exit CO concentration in a PEM fuel cell. Physical Chemistry Chemical Physics 2011;13(40):18179-85.

[16] Chen C, Lai W, Yan W, Chen C, Hsu S. Effects of nitrogen and carbon monoxide concentrations on performance of proton exchange membrane fuel cells with Pt–Ru anodic catalyst. J Power Sources 2013;243:138-46.

[17] Kirsch S, Hanke-Rauschenbach R, Stein B, Kraume R, Sundmacher K. The electro-oxidation of H2, CO in a model PEM fuel cell: Oscillations, chaos, pulses. J Electrochem Soc 2013;160(4):F436-46.

[18] Malkhandi S, Bauer P, Bonnefont A, Krischer K. Mechanistic aspects of oscillations during CO electrooxidation on Pt in the presence of anions: Experiments and simulations. Catalysis Today 2013;202:144-53.

[19] Mota A, Eiswirth M, Gonzalez ER. Enhanced efficiency of CO-containing hydrogen electroxidation with autonomous oscillations. The Journal of Physical Chemistry C 2013;117(24):12495-501.

[20] Perini N, Batista BC, Angelo AC, Epstein IR, Varela H. Long-lasting oscillations in the electro-oxidation of formic acid on PtSn intermetallic surfaces. ChemPhysChem 2014;15(9):1753-60.

[21] Nagao R, Freitas RG, Silva CD, Varela H, Pereira EC. Oscillatory electro-oxidation of methanol on nanoarchitectured Ptpc/Rh/Pt metallic multilayer. ACS Catalysis 2015;5(2):1045-52.

[22] Lee MJ, Kang JS, Kang YS, Chung DY, Shin H, Ahn C, et al. Understanding the Bifunctional Effect for Removal of CO Poisoning: Blend of Platinum Nanocatalyst and Hydrous Ruthenium Oxide as a Model System. ACS Catalysis 2016.

[23] Hanke-Rauschenbach R, Weinzierl C, Krasnyk M, Rihko-Struckmann L, Lu H, Sundmacher K. Operating behavior and scale-up of an ECPrOx unit for CO removal from reformate for PEM fuel cell application. J Electrochem Soc 2009;156(10):B1267-75.

[24] Heidebrecht P, Hanke-Rauschenbach R, Jörke A, Sundmacher K. On the design of cascades of ECPrOx reactors for deep CO removal from reformate gas. Chemical Engineering Science 2012;67(1):34-43.

[25] Zhang J, Datta R. Sustained potential oscillations in proton exchange membrane fuel cells with PtRu as anode catalyst. J Electrochem Soc 2002;149(11):A1423-31.

[26] Strasser P, Eiswirth M, Ertl G. Oscillatory instabilities during formic acid oxidation on Pt (100), Pt (110) and Pt (111) under potentiostatic control. II. Model calculations. J Chem Phys 1997;107(3):991-1003.

[27] Zhang J, Fehribach JD, Datta R. Mechanistic and bifurcation analysis of anode potential oscillations in PEMFCs with CO in anode feed. J Electrochem Soc 2004;151(5):A689-97.

[28] Hanke-Rauschenbach R, Kirsch S, Kelling R, Weinzierl C, Sundmacher K. Oscillations and pattern formation in a PEM fuel cell with Pt/Ru anode exposed to H2/CO mixtures. J Electrochem Soc 2010;157(11):B1521-8.

[29] Kirsch S, Hanke-Rauschenbach R, Sundmacher K. Analysis of spatio-temporal pattern formation in a PEM fuel cell with Pt/Ru anode exposed to H2/CO mixtures. J Electrochem Soc 2011;158(1):B44-53.

[30] Kadyk T, Kirsch S, Hanke-Rauschenbach R, Sundmacher K. Autonomous potential oscillations at the Pt anode of a polymer electrolyte membrane fuel cell under CO poisoning. Electrochim Acta 2011;56(28):10593-602.

[31] Lopes PP, Batista BC, Saglietti GA, Varela H, Ticianelli EA. Real-time determination of CO2 production and estimation of adsorbate coverage on a proton exchange membrane fuel cell under oscillatory operation. Journal of Solid State Electrochemistry 2013;17(7):1851-9.

[32] Mei D, He Z, Jiang DC, Cai J, Chen Y. Modeling of potential oscillation during galvanostatic electrooxidation of formic acid at platinum electrode. The Journal of Physical Chemistry C 2014;118(12):6335-43.

[33] Chávez F, Vicente L, Perera A. Kinetic oscillations in the catalytic CO oxidation on Pt (100) with adsorbed impurities. J Chem Phys 2000;113(22):10353-60.

[34] Koper MT, Schmidt TJ, Markovic NM, Ross PN. Potential oscillations and S-shaped polarization curve in the continuous electro-oxidation of CO on platinum single-crystal electrodes. The Journal of Physical Chemistry B 2001;105(35):8381-6.

[35] Deibert MC, Williams DL. Voltage Oscillations of the H2-CO System. J Electrochem Soc 1969;116(9):1290-2.

[36] Eiswirth M, Bürger J, Strasser P, Ertl G. Oscillating Langmuir-Hinshelwood mechanisms. J Phys Chem 1996;100(49):19118-23.

[37] Koper MT. Non-linear phenomena in electrochemical systems. Journal of the Chemical Society, Faraday Transactions 1998;94(10):1369-78.

[38] Hanke-Rauschenbach R, Mangold M, Sundmacher K. Nonlinear dynamics of fuel cells: a review. Reviews in Chemical Engineering 2011;27(1-2):23-52.

[39] Sundmacher K, Hanke-Rauschenbach R, Heidebrecht P, Rihko-Struckmann L, Vidaković-Koch T. Some reaction engineering challenges in fuel cells: dynamics integration, renewable fuels, enzymes. Current Opinion in Chemical Engineering 2012;1(3):328-35.

[40] Anderson AB, Albu TV. Catalytic effect of platinum on oxygen reduction an ab initio model including electrode potential dependence. J.Electrochem.Soc. 2000;147(11):4229-38.

[41] Springer T, Rockward T, Zawodzinski T, Gottesfeld S. Model for Polymer Electrolyte Fuel Cell Operation on Reformate Feed: Effects of CO, H; 2 Dilution, and High Fuel Utilization. J.Electrochem.Soc. 2001;148(1):A11-23.

[42] Baschuk J, Li X. Modelling CO poisoning and O2 bleeding in a PEM fuel cell anode. Int J Energy Res 2003;27(12):1095-116.

[43] Zamel N, Li X. Transient analysis of carbon monoxide poisoning and oxygen bleeding in a PEM fuel cell anode catalyst layer. Int J Hydrogen Energy 2008;33(4):1335-44.

[44] Baschuk JJ, Rowe AM, Li X. Modeling and simulation of PEM fuel cells with CO poisoning. Journal of energy resources technology 2003;125(2):94-100.

[45] Shah A, Sui P, Kim G, Ye S. A transient PEMFC model with CO poisoning and mitigation by O2 bleeding and Ru-containing catalyst. J Power Sources 2007;166(1):1-21.

[46] Ju H, Lee K, Um S. Multi-dimensional modeling of CO poisoning effects on proton exchange membrane fuel cells (PEMFCs). Journal of Mechanical Science and Technology 2008;22(5):991-8.

[47] Zhang J, Datta R. Online monitoring of anode outlet CO concentration in PEM fuel cells. Electrochemical and solid-state letters 2003;6(1):A5-8.

[48] Gasteiger HA, Markovic NM, Ross Jr PN. H2 and CO electrooxidation on well-characterized Pt, Ru, and Pt-Ru. 1. Rotating disk electrode studies of the pure gases including temperature effects. J.Phys.Chem. 1995;99(20):8290-301.

[49] Gasteiger HA, Markovic NM, Ross Jr PN. H2 and CO Electrooxidation on Well-Characterized Pt, Ru, and Pt-Ru. 2. Rotating Disk Electrode Studies of CO/H2 Mixtures at 62. degree. C. J.Phys.Chem. 1995;99(45):16757-67.

[50] Gilman S. The mechanism of electrochemical oxidation of carbon monoxide and methanol on platinum. II. The “Reactant-Pair” mechanism for electrochemical oxidation of carbon monoxide and methanol. J Phys Chem 1964;68(1):70-80.

[51] Wang K, Gasteiger H, Markovic N, Ross P. On the reaction pathway for methanol and carbon monoxide electrooxidation on Pt-Sn alloy versus Pt-Ru alloy surfaces. Electrochim Acta 1996;41(16):2587-93.

[52] Koper M, Lukkien J, Jansen A, Van Santen R. Lattice gas model for CO electrooxidation on Pt-Ru bimetallic surfaces. The Journal of Physical Chemistry B 1999;103(26):5522-9.

[53] Bird RB, Stewart WE, Lightfoot EN. Transport phenomena. Wiley, New York, 1960.

[54] Meredith RE, Tobias CW. Conduction in heterogeneous systems. Advances in electrochemistry and electrochemical engineering 1962;2(Part II):15-47.

[55] Multiphysics COMSOL 4.3a, 2013. COMSOL Inc., Burlington, MA.

[56] Multiphysics COMSOL 4.3a Reference Manual, 2013. COMSOL Inc., Burlington, MA.

[57] Yang X, Wang G, Liu Y, Hou X. A comparative analysis of the computational stability for Galerkin finite element and difference schemes of nonlinear advection equation. Int J Inf Syst Sci 2006;2(3):336-42.

[58] Ascher UM, Petzold LR. Computer methods for ordinary differential equations and differential-algebraic equations. SIAM, Philadelphia, 1998.

[59] Gear CW. Simultaneous numerical solution of differential-algebraic equations. Circuit Theory, IEEE Transactions on 1971;18(1):89-95.

[60] Shampine LF. Numerical solution of ordinary differential equations. Chapman-Hall, New York, 1994.

[61] Weddemann A, Thümmler V. Stability analysis of ALE-methods for advection-diffusion problems. Excerpt from the Proceedings of the COMSOL Conference, 2008.

[62] Farrell C, Gardner C, Ternan M. Experimental and modelling studies of CO poisoning in PEM fuel cells. J.Power Sources 2007;171(2):282-93.

[63] Lee S, Mukerjee S, Ticianelli E, McBreen J. Electrocatalysis of CO tolerance in hydrogen oxidation reaction in PEM fuel cells. Electrochim Acta 1999;44(19):3283-93.

[64] Pereira LGS, Paganin VA, Ticianelli EA. Investigation of the CO tolerance mechanism at several Pt-based bimetallic anode electrocatalysts in a PEM fuel cell. Electrochim Acta 2009;54(7):1992-8.

[65] Rocha TA, Ibanhi F, Colmati F, Linares JJ, Paganin VA, Gonzalez ER. Nb as an influential element for increasing the CO tolerance of PEMFC catalysts. J Appl Electrochem 2013;43(8):817-27.

[66] Ju H, Meng H, Wang C. A single-phase, non-isothermal model for PEM fuel cells. Int J Heat Mass Transfer 2005;48(7):1303-15.

[67] Koper M, Jansen A, Van Santen R, Lukkien J, Hilbers P. Monte Carlo simulations of a simple model for the electrocatalytic CO oxidation on platinum. J Chem Phys 1998;109(14):6051-62.

**Table 2.1** Physical, mechanical and electrochemical parameters used in the numerical model.

| **Name of Coefficient** | **Value or Equation** | **Unit** | **Ref.** |
|---|---|---|---|
| Catalyst Layer (CL) Length, $l_c$ | 0.001 | cm | |
| Cell Temperature, T | 353 | K | |
| Anode Pressure, $P_a$ | 1 | atm | |
| Reference Temperature, $T_{ref}$ | 298 | K | [45,66] |
| Reference Pressure, $P_{ref}$ | 1 | atm | [45,66] |
| Anode Relative Humidity, $\phi_a$ | 1 | | |
| Transfer Coefficient, $\alpha$ | 0.5 | | [27] |
| Porosity of Catalyst Layer, $\varepsilon_c$ | 0.6 | | [43] |
| Specific Electroactive Surface Area, $A_v$ | 1,000 | 1/cm | [41,46] |
| Surface Roughness Factor, $\gamma$ | 100 | | [27] |
| Molar Area Density, $C_t$ | $2.2 \times 10^{-9}$ | mol $cm^{-2}$ | [27] |
| Standard Diffusion Coefficient for $H_2$, $D_{H,o}$ | $1.43 \times 10^{-4}$ | $cm^2/s$ | [45] |
| Standard Diffusion Coefficient for CO, $D_{CO,o}$ | $4.12 \times 10^{-5}$ | $cm^2/s$ | [45] |
| Effective Ionic Conductivity, $\sigma_i^{eff}$ | 3 | S/m | [41] |
| Effective Electronic Conductivity, $\sigma_s^{eff}$ | $72{,}700 \times (1-\varepsilon_c)^{1.5}$ | S/m | [42] |
| $H_2$ Electro-oxidation Rate Constant, $k_{h,ox}$ | 4 | A $cm^{-2}$ | [41] |
| $H_2$ Adsorption Rate Constant, $k_{h,a}^*$ | 180 | A $cm^{-2}$ $atm^{-1}$ | [31,41] |
| $H_2$ Desorption Rate Constant, $k_{h,d}$ | 0.5 | atm | [41] |
| CO Adsorption Rate Constant, $k_{co,a}^*$ | 100 | A $cm^{-2}$ $atm^{-1}$ | [30,41] |
| CO Desorption Rate Constant, $k_{co,d}$ | $(1.5 \times 10^{-8}) \times e^{6.8\theta_{co}}$ | atm | [41] |
| OH Adsorption Rate Constant, $k_{w,a}^*$ | $3 \times 10^{-6}$ | A $cm^{-2}$ | [31,67] |
| OH Desorption Rate Constant, $k_{w,d}$ | 2,760 | A $cm^{-2}$ | [30,31] |
| CO Electro-oxidation Rate Constant, $k_{co,ox}$ | $3.6 \times 10^{-5}$ | A $cm^{-2}$ | [31,67] |
| Current Density, J | 0.1 | A $cm^{-2}$ | |

*Fitted parameters during model validation. The numerical values in the corresponding references are considered along with the model validation for parameter fitting.

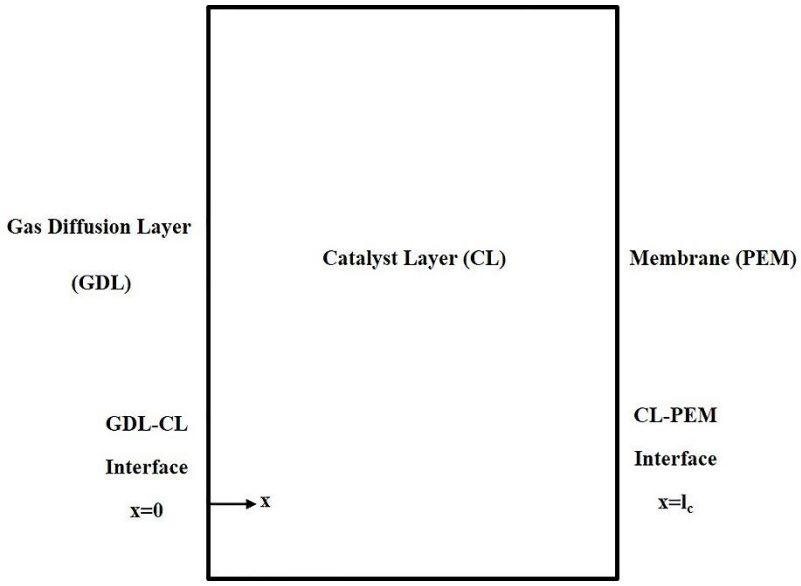


**Fig. 2.1** A schematic view of the domain used in the numerical solution.

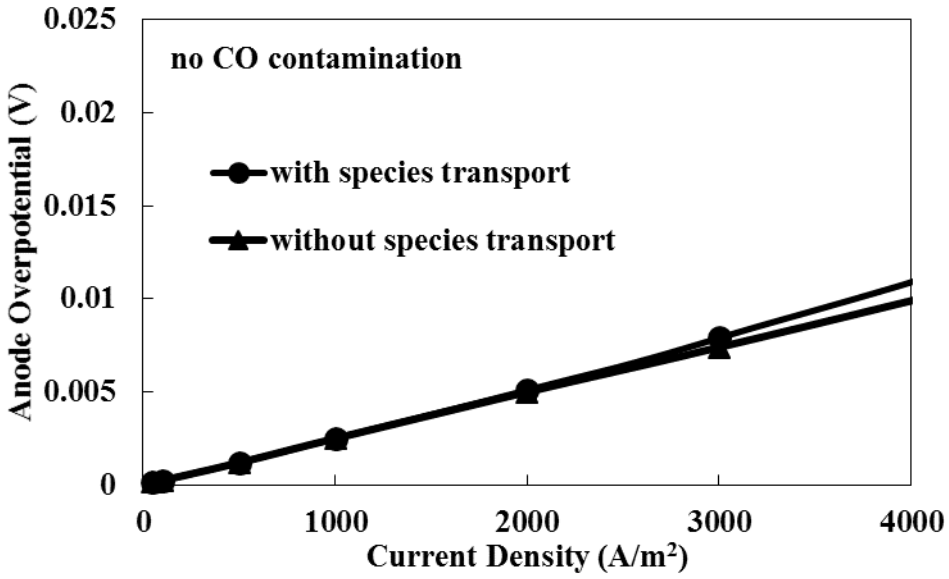


**Fig. 2.2** Anode overpotential vs. current density with (circular points) and without (triangular points) species transport effect/equation; $y_{CO,i}$ = 0 ppm.

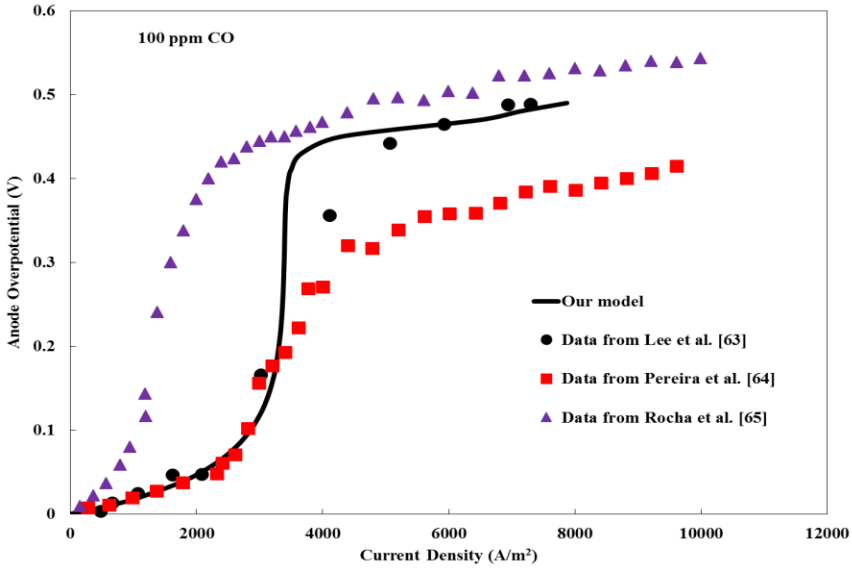


**Fig. 2.3** Validation of the current model with the available experimental data from Lee et al. [63], Pereira et al. [64] and Rocha et al. [65]; cell temperature, T = 358 K (All other parameters are the same as in Table 1); $y_{CO,i}$ = 100 ppm.

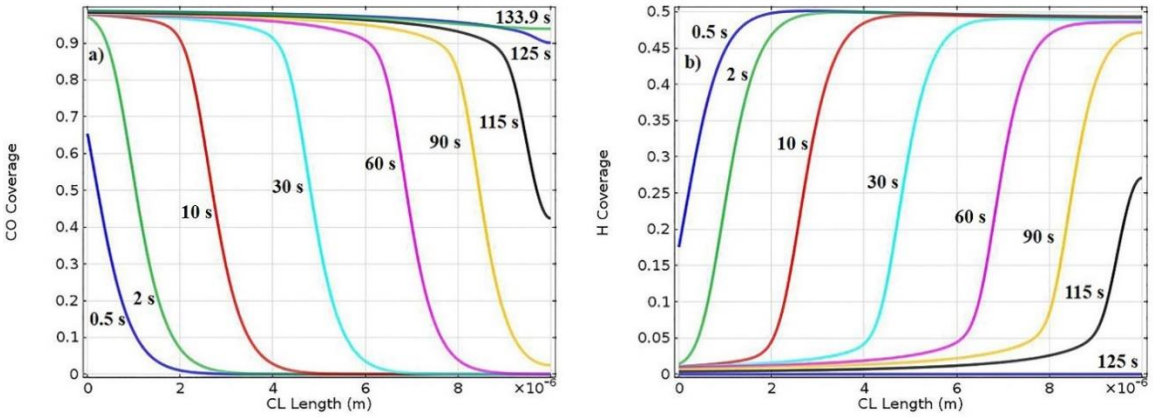


**Fig. 2.4** Transient coverages of adsorbed **a)** carbon monoxide, and **b)** hydrogen along the catalyst layer (CL) length; $y_{CO,i}$ = 1,000 ppm.

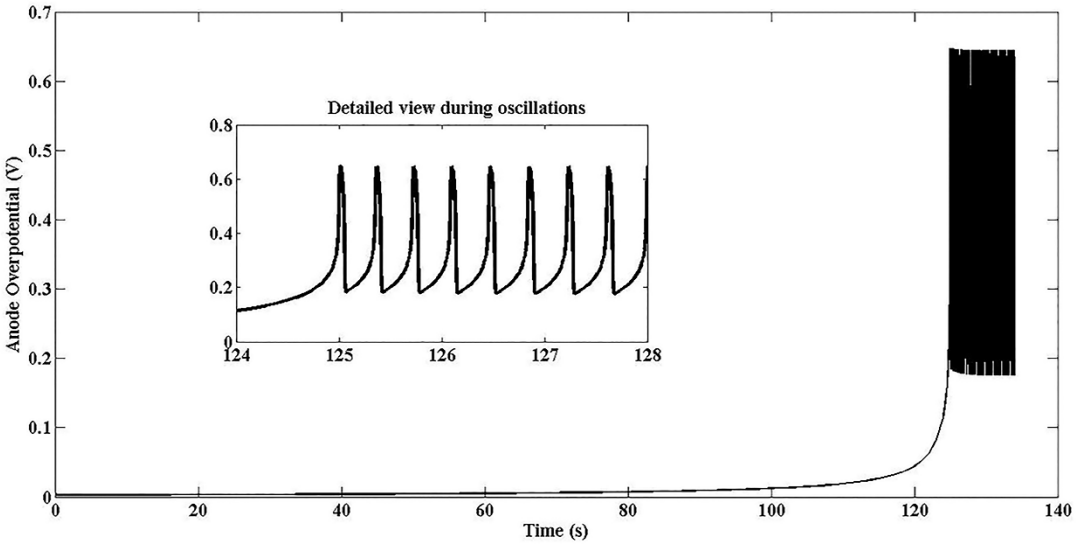


**Fig. 2.5** Anode overpotential vs. time with a detailed view during the oscillations for 1,000 ppm CO contamination.

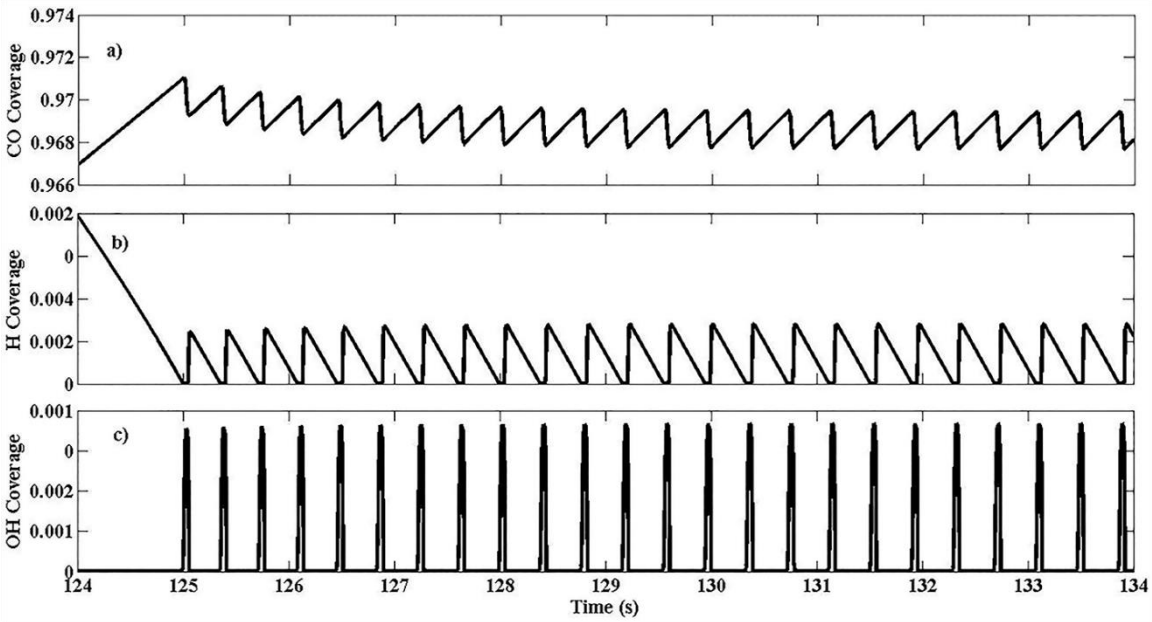


**Fig. 2.6** Averaged coverages (along the CL length) of adsorbed species vs. time during oscillations; **a)** carbon monoxide, **b)** hydrogen, and **c)** hydroxyl coverage; $y_{CO,i}$ = 1,000 ppm.

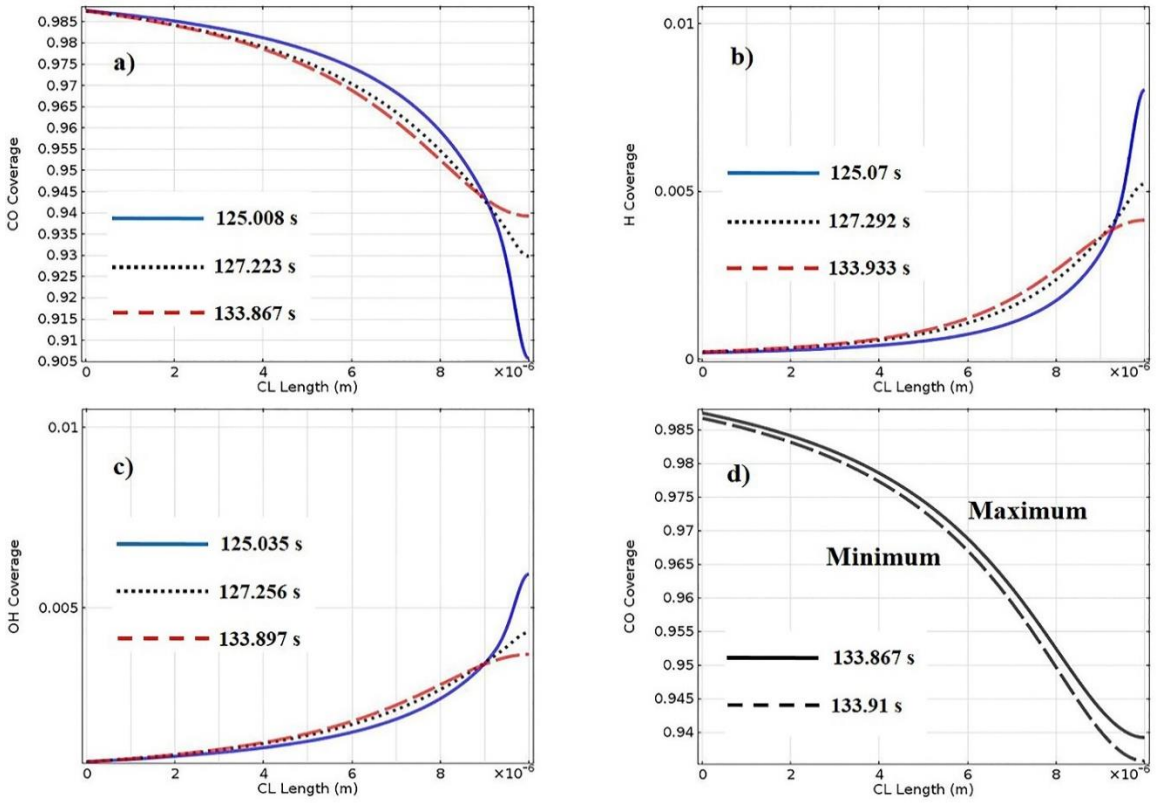


**Fig. 2.7** Maximum point (peak) of oscillations for the transient coverages of adsorbed **a)** carbon monoxide, **b)** hydrogen, **c)** hydroxyl along the CL, and **d)** Maximum and minimum carbon monoxide coverage at steady state along the CL during the oscillations; $y_{CO,i}$ = 1,000 ppm.

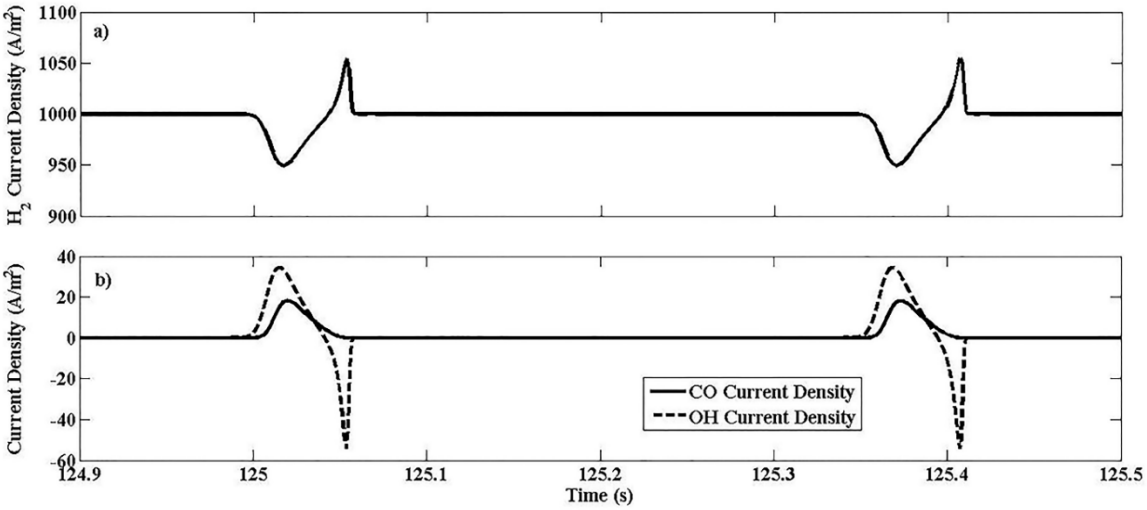


**Fig. 2.8** Generations of current density due to **a)** hydrogen electro-oxidation; reaction (2), **b)** carbon monoxide electro-oxidation; reaction (4) and hydroxyl adsorption; reaction (5) during the oscillations; $y_{CO,i}$ = 1,000 ppm.

# Chapter 3 Removal of CO Poisoning from $H_2$/CO Mixtures in Pt CL with Current Pulsing

## 3.1 Introduction

It is already known that platinum (Pt) sites are covered by CO in the anode catalyst layer [1-4]. CO molecules adsorb strongly on the active sites [5]. Hence, Pt sites, which are otherwise available for $H_2$ electro-oxidation are blocked, reducing the effective number of sites and decreasing cell voltage, i.e. higher anode overpotential. Electro-oxidation of CO is very slow below ~0.5 V on Pt surfaces [6,7], therefore, a significantly reduced cell voltage or performance is seen, even when the anode fuel has very low CO concentrations (10-20 ppm) [8,9].

There have been ongoing demand and efforts to mitigate or reduce the CO poisoning [1,2,10-12]. Most common techniques, which were investigated until now, can be classified as follows: i) Preferential Oxidation (PROX) with air bleeding, ii) Air/Oxygen bleeding into the cell anode, iii) Using Pt-alloys or CO-tolerant anode catalysts, and iv) "Self-oxidation" or Electrochemical Preferential Oxidation (ECPROX). Although the proposed techniques are known to be useful depending upon the applications, they have been proved to be limited with cost and durability issues, complexity, and loss of fuel and performance [1,2,13-16].

Accordingly, an increasing interest has been drawn to another method, current or anode potential pulsing. It is already indicated that adsorbed CO on Pt particles cannot be oxidized below potentials ~0.5 V. It was previously found by Anderson and Albu [17] that water is dissociated to reveal adsorbed hydroxyl (OH) species on Pt above the potential

0.5-0.6 V. Furthermore, Gasteiger et al. [6,7] observed highly active CO electro-oxidation above the range of potential 0.5-0.7 V for the Pt nanoparticles. Hence, it can be concluded that CO poisoning can be altered by achieving the current or the anode overpotential high enough for the CO electro-oxidation with adsorbed OH.

There are several experimental studies [18-27] about pulsing. Carrette et al. [18] indicated 70% performance recovery with current pulsing for 10,000 ppm (1%) CO level at Pt/Ru catalysts. Thomason et al. [19] found that current pulsing method was more effective than "self-oxidation" for 500 ppm CO at the anode feed with Pt/Ru catalyst. Investigation of current pulsing on Pt/Ru alloy catalysts was also performed by Choi et al. [20], Adams et al. [21], and Gardner and Ternan [22] for 500 ppm, 10,000 ppm and 1,000 ppm levels of CO impurities, respectively. Pulsing of anodic voltage was also suggested by Saunders et al. [23] in order to mitigate CO poisoning at the Pt/Ru surface. It was shown in their study [23] that CO effect on the catalyst layer could be reduced from 10,000 ppm to 20 ppm level with pulsing. Same approach was also presented by Wingelaar et al. [24] for non-alloyed Pt catalysts, poisoned with 50 ppm CO. Their work [24] implied that 93% of the output energy could be restored in a PEFC with an anodic pulse of 0.8-0.9 V amplitude for 0.12 s. Majidi and Pickup [25,26] suggested the method of potential cycling in order to improve $CO_2$ yield for ethanol oxidation in a direct ethanol fuel cell (DEFC). Finally, Balasubramanian and Weidner [27] analyzed an electrochemical filter to hold anode potential at 0.7 V for at least 10 s for the removal of CO from reformate. Their results [27] seem feasible with relatively low required potential, however anodic voltage should be maintained at 0.7 V for at least 150 s and 15 s for the complete removal of 1,000 ppm and 10,000 ppm CO, respectively. Pt dissolution and ECSA loss by catalyst sintering are

the main stability issues for frequent repetitive current/voltage pulsing and very low cell voltages [16,28]. Therefore, the duration and the frequency of pulsing need to be optimized carefully.

Although there are considerable experimental studies available in literature, limited number of modeling studies [29-32] can be found about the current/potential pulsing. All of the existing approaches [29-32] are zero-dimensional, and did not take into account the diffusion of species through the anode catalyst layer (CL). Dhanda and Pitsch [29] performed an optimization effort for the characterization of the pulsed current on a Pt electrode assuming CO electro-oxidation with water (not adsorbed OH). Glenn and Saunders [30] applied the similar approach to show the effects of voltage pulsing on Pt/Ru electrode using semi-empirical coefficients. It is revealed from their optimization results [30] that pulsing the anodic potential with 1 V amplitude gives the most efficient outcome for the cleaning of CO from the anode CL. However, it is already known that irreversible "platinum oxide" growth is anticipated above 0.9 V at the Pt surface [33-35], by which the catalyst layer can be damaged permanently. Balasubramanian et al. [31] provided a model for the effect of long-term (>5 s) potential pulsing along the anode CL. Only CO coverage was included, and the kinetics of H and OH coverages were neglected in their study [31]. Farrell et al. [32] investigated the voltage oscillations at Pt/Ru catalysts during CO poisoning, and the effect of current pulsing on the surface coverages of $H_2$, CO and OH. Oscillations at the anode overpotential were the focal point of their research [32]. Besides,

their results [32] introduced the preliminary effects of current pulsing on the CO mechanism rather than the complete mitigation of the CO poisoning in catalyst layer.

In this chapter, the previous model developed in Chapter 2 is further applied for the 10,000 ppm CO poisoning (in $H_2$ fuel). Unlike the results for 1,000 ppm CO in the previous chapter, no oscillations could be detected for 10,000 ppm (1%) CO contamination. When steady-state condition is reached for the overpotential and the coverages, current is pulsed to a higher value to mitigate the negative impacts of CO. In the next sections, the numerical method and the modeling results to observe/mitigate the effect of 1% CO poison on Pt catalyst layer are presented.

### 3.2 Numerical method

Modeling for 10,000 ppm CO poisoning has maximum time steps of 10 ms at the beginning of contamination ($t < 3$ s), 2 ms before the peak overpotential ($3 \text{ s} < t < 12.67$ s), 0.02 ms near the region of peak overpotential ($12.67 \text{ s} < t < 12.7$ s), and 0.1 s until the pulse is applied ($12.7 \text{ s} < t < 50$ s). Thereafter, current pulsing stage is solved for the mitigation of 10,000 ppm CO with maximum time step of 0.05 ms from $t = 50$ s to 50.1 s. All other numerical procedure for the analysis of 1% CO is the same as the one for the 1,000 ppm CO case, which was mentioned in section 2.3.

### 3.3 Results and discussion

The following section explains the results for the poisoning stage of 10,000 ppm CO at the Pt catalyst layer until the steady state. Next, current pulsing technique is applied for the 10,000 ppm level to remove the adsorbed CO from the Pt surface in the section 3.3.2.

### 3.3.1 10,000 ppm CO poisoning

In this part, effects of 10,000 ppm (1%) CO poisoning are presented with Figures 3.1 and 3.2. Figure 3.1 demonstrates transient coverages of adsorbed carbon monoxide and hydrogen with time at the poisoning stage. Similar to the 1,000 ppm CO poison, negligible level of OH coverage ($10^{-10}$) is predicted throughout the CL at the contamination stage of 10,000 ppm CO, until a certain level of anode potential is achieved. On the other hand, GDL interface of the CL is poisoned with 99.8% CO in less than 0.5 s, and 90% of the catalyst layer length is completely covered by adsorbed CO in ~12.7 s, as shown in Figure 3.1a. CO coverage at PEM interface is evaluated to be ~0.79, and the overpotential reaches ~0.73 V at time, t=12.7 s, as indicated in Figure 3.2a. It is seen from Figure 3.2a that there is a 0.11 V drop in the overpotential due to formation of adsorbed OH at this potential. Hence, the high overpotential is enough to overcome the CO diffusion near the CL-PEM interface, and a limited amount of adsorbed CO oxidizes with the available OH species. CO coverage at the right interface drops to ~0.67 along with a steep increment of OH coverage up to ~0.032 at steady state (time >40 s). The oscillative behavior observed with 1,000 ppm CO is not reproduced for the 10,000 ppm case. Anode overpotential reduces to 0.62 V in Figure 3.2a, and remains at this value until the steady state condition is achieved. Even if the peak potential is up to 0.73 V, the production of adsorbed OH within the CL surface is not enough to oxidize sufficient adsorbed CO to lower the potential.

Transient coverages of adsorbed hydrogen with time are presented in Figure 3.1b. The trend in H coverage is similar to the 1,000 ppm case (recall Figure 2.4b). While catalyst layer is initially covered with adsorbed hydrogen at the early stage of poisoning, it is replaced by carbon monoxide and lowered to almost zero in 12.7 s. Unlike the results for

1,000 ppm CO, the level of H coverage remains close to zero in Figure 3.1b, until the steady state.

### 3.3.2 Current pulsing to enable oxidative removal of CO

To enable oxidative removal of CO, after steady state is reached, current density is changed from 0.1 to 2.5 A/cm$^2$ (at t =50 s to t=50.01 s), and held at 2.5 A/cm$^2$ for 50 ms. Results during the pulsing stage are investigated in Figures 3.2-3.4. To begin with, Figure 3.2b shows the anode overpotential for the pulsing step. It is seen that anode overpotential instantaneously increases from 0.62 V to a peak potential of ~0.92 V due to the initial period of pulsing. Next, a gradual decrease in overpotential is observed, as the current is still held at 2.5 A/cm$^2$ until the time, t=50.06 s. At this point of time, the pulse is removed, and it is lowered from 2.5 A/cm$^2$ to 0.1 A/cm$^2$ in 10 ms. Note that current density pulse is demonstrated in Figure 3.3a. After the current starts to decrease, a quick and then a slower reduction occurs in overpotential. When the current density eventually becomes 0.1 A/cm$^2$ at t=50.07 s, a sharp drop in anode overpotential to below 0.01 V is seen in Figure 3.2b. The corresponding drop is originated from the cleaning, i.e. removing, of adsorbed CO from the catalyst layer during the pulsing stage. When the pulsing is completed, overpotential increases over time since the catalyst layer is covered with CO again.

The argument above is additionally supported by Figures 3.3a-b, which show the components of current density, along with the total current density and average coverages during the pulsing. As seen from Figure 3.3b, average CO coverage decreases from almost unity down to ~0.08 from the pulse initiation until time, t=50.06 s, onset of the pulse reduction. Meanwhile, coverage of adsorbed OH becomes higher and reaches up to 0.7, and then it is seen to approach steadily to zero as the current density is lowered to the base

value. H coverage is negligibly small during the pulse stage in Figure 3.3b. However, when pulse is over (50.06 s to 50.07 s), adsorbed OH is converted to water by desorption due to the lower potential. This phenomenon is also evidenced by the negative OH current density shown in Figure 3.3a. Therefore, available Pt sites are occupied by adsorbed H, and H coverage increases to 0.45 between 50.07-50.1 s, (Figure 3.3b).

It has been shown in Figure 3.3b that more than 90 percent of the adsorbed CO can be removed from the catalyst layer with a current pulse. To further probe the effect of pulsing, one-dimensional transient coverages of adsorbed species are shown in Figure 3.4. Figure 3.4a suggests that adsorbed CO can be removed rapidly, more effectively close to the PEM interface at the beginning of pulse. As the current pulse is ended at t = 50.06 s, adsorbed CO can be detected within only 3 μm from the GDL-CL interface. The main reason for the adsorbed CO coverage at the GDL interface (~0.86) even at the end of pulsing is the dominance of CO diffusion over the CO electro-oxidation. The other 70% of catalyst layer length seems to be completely CO-free at the end of pulsing process. OH coverage during the pulse is also shown in Figure 3.4c. Figures 3.4a and 3.4c indicate that adsorbed CO is replaced with OH during the pulse. Furthermore, Figure 3.4b demonstrates the H coverage just after the removal of current pulse (from t=50.06 s to t=50.1 s). It is presented in Figure 3.4b that hydrogen is readily adsorbed on available Pt sites along with the resulting lower overpotential at the base current, 0.1 A/cm$^2$.

### 3.4 Conclusion

One-dimensional transient kinetics of 10,000 ppm CO poisoning at Pt catalyst layer with the fuel of $H_2$/CO mixture have been analyzed numerically. Unlike the 1,000 ppm case, the oscillations are not present with 10,000 ppm (1%) CO. Even when a peak overpotential at

around 0.73 V is predicted at the contamination stage of 10,000 ppm CO level, the overpotential is reduced with the electro-oxidation of a very limited amount of CO, and then is stabilized at ~0.62 V. The proposed logic behind this is the dominance of strong CO diffusion from GDL to PEM interface (due to high CO concentration, 10,000 ppm) over the CO electro-oxidation. Hence, only a limited number of adsorbed CO can be oxidized by the production of OH at the peak overpotential, ~0.73V, and CO coverage remains relatively high with a decrease of only ~0.11 V in overpotential. A steady-state potential is reached without any oscillations for 1% CO in $H_2$.

At the steady state condition (with 1% CO), current density is pulsed from 0.1 to 2.5 A/cm$^2$ for 50 ms to enable oxidative removal of CO. It is found that 92% of adsorbed CO can be removed from the Pt surface with the current pulse. In addition, 70% of the catalyst layer becomes CO-free after the pulsing, however 30% of the catalyst layer near the GDL interface has a considerable coverage, as high as 0.86. The main reason for this situation is that relatively strong CO diffusion near the GDL interface overcomes the faster CO electro-oxidation during pulsing due to the high CO concentration. To conclude, current pulsing is found to be a promising method to remove the adsorbed CO from the catalyst surfaces.

### 3.5 References

[1] Zamel N, Li X. Effect of contaminants on polymer electrolyte membrane fuel cells. Progress in Energy and Combustion Science 2011;37(3):292-329.

[2] Liu Z. Effects of fuel and air impurities on PEFC performance. Polymer Electrolyte Fuel Cells: Science, Applications, and Challenges 2013:427.

[3] Springer T, Rockward T, Zawodzinski T, Gottesfeld S. Model for polymer electrolyte fuel cell operation on reformate feed: Effects of CO, H2 dilution, and high fuel utilization. J Electrochem Soc 2001;148(1):A11-23.

[4] Baschuk J, Li X. Carbon monoxide poisoning of proton exchange membrane fuel cells. Int J Energy Res 2001;25(8):695-713.

[5] Ciureanu M, Wang H. Electrochemical impedance study of electrode-membrane assemblies in PEM fuel cells: I. Electro-oxidation of H2 and H2/CO mixtures on Pt-based gas-diffusion electrodes. J Electrochem Soc 1999;146(11):4031-40.

[6] Gasteiger HA, Markovic NM, Ross Jr PN. H2 and CO electrooxidation on well-characterized Pt, Ru, and Pt-Ru. 1. Rotating disk electrode studies of the pure gases including temperature effects. J Phys Chem 1995;99(20):8290-301.

[7] Gasteiger HA, Markovic NM, Ross Jr PN. H2 and CO electrooxidation on well-characterized Pt, Ru, and Pt-Ru. 2. Rotating disk electrode studies of CO/H2 mixtures at 62 °C. J Phys Chem 1995;99(45):16757-67.

[8] Rodrigues A, Amphlett JC, Mann RF, Peppley B, Roberge PR. Carbon monoxide poisoning of proton-exchange membrane fuel cells. Energy Conversion Engineering Conference, 1997. IECEC-97. Proceedings of the 32nd Intersociety: IEEE 1997:768-73.

[9] Wilkinson P, Thompsett D. in Proceedings of the Second International Symposium on New Materials for Fuel-Cell and Modern Battery Systems. Montreal, Canada 1997:266.

[10] Luengnaruemitchai A, Chawla S, Wanchanthuek R. The catalytic performance of Au/La-CeOx catalyst for PROX reaction in H2 rich stream. Int J Hydrogen Energy 2014;39(30):16953-63.

[11] Luengnaruemitchai A, Srihamat K, Pojanavaraphan C, Wanchanthuek R. Activity of Au/Fe2 O3–TiO2 catalyst for preferential CO oxidation. Int J Hydrogen Energy 2015;40(39):13443-55.

[12] Lee MJ, Kang JS, Kang YS, Chung DY, Shin H, Ahn C, et al. Understanding the bifunctional effect for removal of CO poisoning: Blend of platinum nanocatalyst and hydrous ruthenium oxide as a model system. ACS Catalysis 2016;6(4):2398-407.

[13] Inaba M, Sugishita M, Wada J, Matsuzawa K, Yamada H, Tasaka A. Impacts of air bleeding on membrane degradation in polymer electrolyte fuel cells. J Power Sources 2008;178(2):699-705.

[14] Hanke-Rauschenbach R, Mangold M, Sundmacher K. Nonlinear dynamics of fuel cells: a review. Reviews in Chemical Engineering 2011;27(1-2):23-52.

[15] Sundmacher K, Hanke-Rauschenbach R, Heidebrecht P, Rihko-Struckmann L, Vidaković-Koch T. Some reaction engineering challenges in fuel cells: dynamics integration, renewable fuels, enzymes. Current Opinion in Chemical Engineering 2012;1(3):328-35.

[16] Mehmood A, Scibioh MA, Prabhuram J, An M, Ha HY. A review on durability issues and restoration techniques in long-term operations of direct methanol fuel cells. J Power Sources 2015;297:224-41.

[17] Anderson AB, Albu TV. Catalytic effect of platinum on oxygen reduction an ab initio model including electrode potential dependence. J Electrochem Soc 2000;147(11):4229-38.

[18] Carrette L, Friedrich K, Huber M, Stimming U. Improvement of CO tolerance of proton exchange membrane (PEM) fuel cells by a pulsing technique. Physical Chemistry Chemical Physics 2001;3(3):320-4.

[19] Thomason A, Lalk T, Appleby A. Effect of current pulsing and “self-oxidation” on the CO tolerance of a PEM fuel cell. J Power Sources 2004;135(1):204-11.

[20] Choi W, Enjeti PN, Appleby AJ. An advanced power converter topology to significantly improve the CO tolerance of the PEM fuel cell power systems. Industry Applications Conference, 2004. 39th IAS Annual Meeting. Conference Record of the 2004 IEEE: IEEE 2004;2:1185-91.

[21] Adams W, Blair J, Bullock K, Gardner C. Enhancement of the performance and reliability of CO poisoned PEM fuel cells. J Power Sources 2005;145(1):55-61.

[22] Gardner C, Ternan M. Electrochemical separation of hydrogen from reformate using PEM fuel cell technology. J Power Sources 2007;171(2):835-41.

[23] Saunders J, Glenn B, Myers J, Cucksey C, Mukerjee S, Boggs C, et al. Pulsing for Enhanced CO Mitigation: Single Cell Performance. ECS Transactions 2008;6(25):343-9.

[24] Wingelaar P, Geers M, Duarte J, Hendrix M. CO-tolerant operation of platinum-loaded PEM fuel cells. Industrial Electronics, 2007. ISIE 2007. IEEE International Symposium on: IEEE 2007:2631-6.

[25] Majidi P, Pickup PG. Sinusoidal potential cycling operation of a direct ethanol fuel cell to improving carbon dioxide yields. J Power Sources 2014;268:439-42.

[26] Majidi P, Pickup PG. Improving carbon dioxide yields and cell efficiencies for ethanol oxidation by potential scanning. J Power Sources 2014;269:173-9.

[27] Balasubramanian S, Weidner JW. Analysis of an electrochemical filter for removing carbon monoxide from reformate hydrogen. J Electrochem Soc 2015;162(10):E231-6.

[28] Colón-Mercado HR, Popov BN. Stability of platinum based alloy cathode catalysts in PEM fuel cells. J Power Sources 2006;155(2):253-63.

[29] Dhanda A, Pitsch H. Reduction of CO poisoning in PEM fuel cell by application of optimal pulse control. ECS Transactions 2009;19(31):57-64.

[30] Glenn BC, Saunders JH. Optimal performance from electrochemical devices using control theory at the surface coverage level. J Electrochem Soc 2011;159(2):B165-72.

[31] Balasubramanian S, Lakshmanan B, Hetzke CE, Sethuraman VA, Weidner JW. Quantifying oxidation rates of carbon monoxide on a Pt/C electrode. Electrochim Acta 2011;58:723-8.

[32] Farrell C, Gardner C, Ternan M. Experimental and modelling studies of CO poisoning in PEM fuel cells. J Power Sources 2007;171(2):282-93.

[33] Markovic N, Lucas C, Grgur B, Ross P. Surface electrochemistry of CO and H2/CO mixtures at Pt (100) interface: Electrode kinetics and interfacial structures. The Journal of Physical Chemistry B 1999;103(44):9616-23.

[34] Conway BE. Electrochemical oxide film formation at noble metals as a surface-chemical process. Prog Surf Sci 1995;49(4):331-452.

[35] Huang Y, Zhang J, Kongkanand A, Wagner FT, Li JC, Jorné J. Transient platinum oxide formation and oxygen reduction on carbon-supported platinum and platinum-cobalt alloy electrocatalysts. J Electrochem Soc 2014;161(1):F10-5.

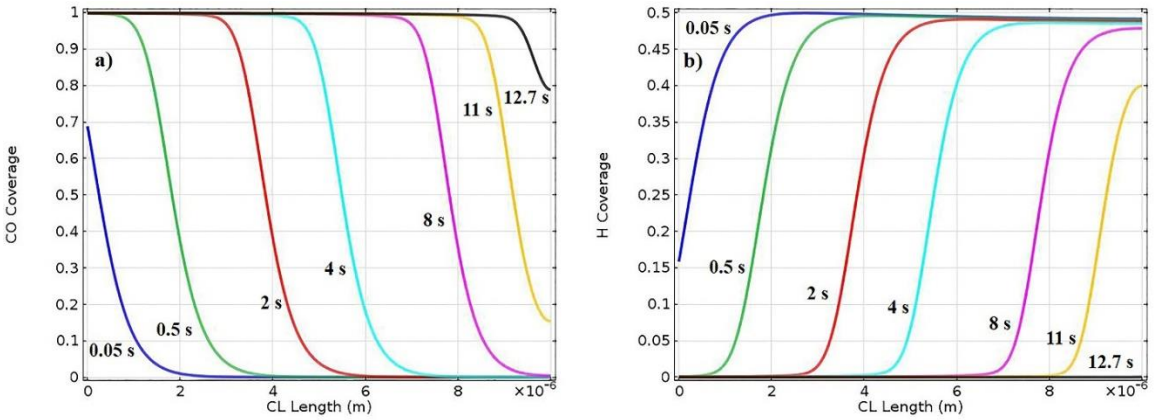


**Fig. 3.1** Transient coverages of adsorbed **a)** carbon monoxide, and **b)** hydrogen along the catalyst layer (CL) length during the contamination stage; $y_{CO,i}$ = 10,000 ppm.

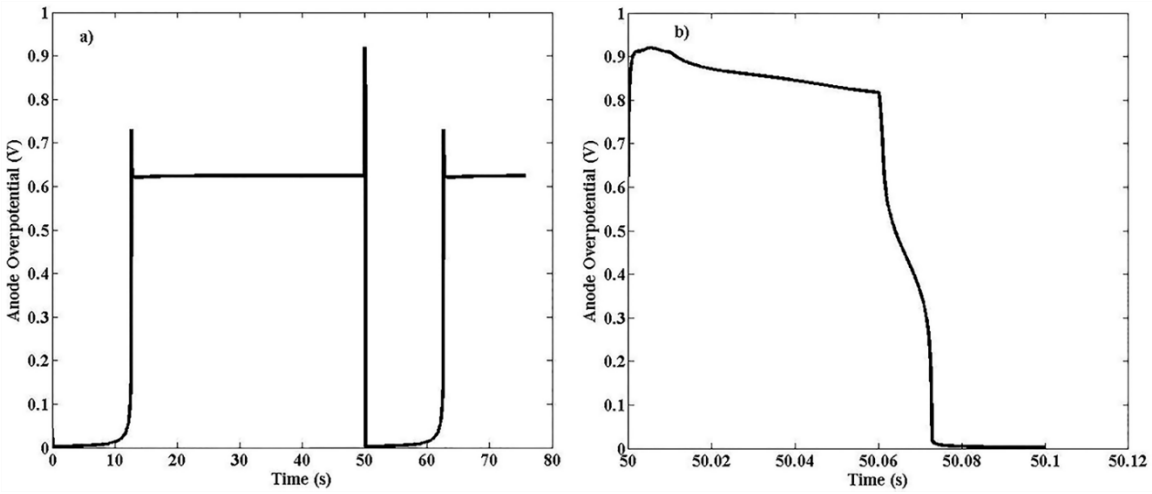


**Figure 3.2** Anode overpotential vs. time **a)** for the complete solution, and **b)** during the application of current pulse for 10,000 ppm CO contamination (Note: Current is pulsed from time = 50 s to 50.07 s).

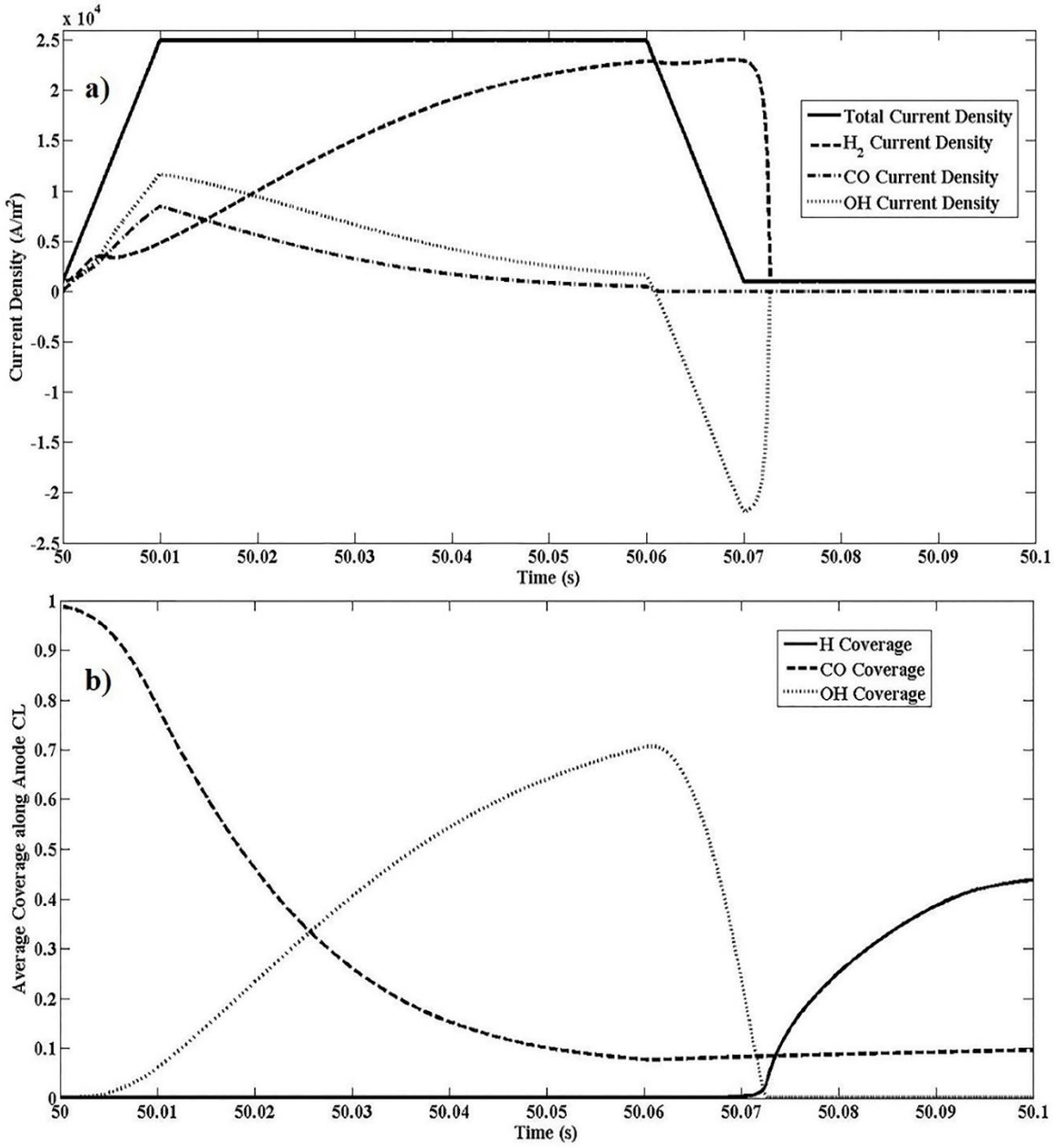


**Figure 3.3** Detailed explanation of the current pulsing step and mechanism with **a)** Current density generations due to reactions (2), (4) and (5), and total current density, and **b)** Averaged coverages along the catalyst layer; $y_{CO,i}$ = 10,000 ppm.

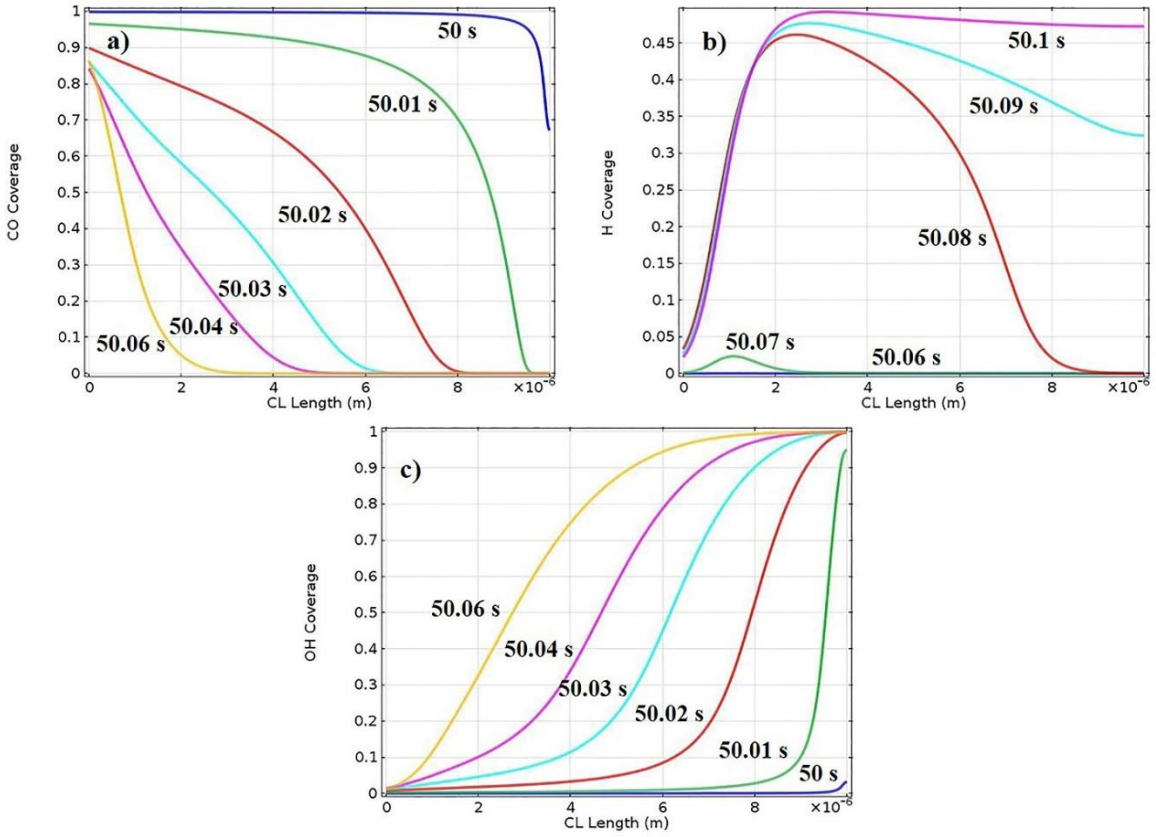


**Figure 3.4** Transient coverages of adsorbed species along the CL, **a)** carbon monoxide coverage during the pulsing process, **b)** hydrogen coverage just after the pulse removal, **c)** hydroxyl coverage during the pulsing process; $y_{CO,i}$ = 10,000 pp

# Chapter 4 Screening Tests for Several Cleansing Agents during their Injection into PEFC Cathode Inlet and the Observation of PEFC Performance Loss and Recovery

## 4.1 Introduction

Due to the higher demand for emission-free and environmentally friendly power production, fuel cells are considered to be an alternative source of clean and renewable energy. Among the various types of fuel cells, polymer electrolyte fuel cells (PEFCs) are a promising candidate for the energy production owing to their low operation temperature, zero-emission potential, high efficiency in power and smaller space requirements [1,2].

Although PEFCs possess many advantages as a source of renewable energy, there are still significant challenges in commercial applications. Durability issues due to the presence of impurities are one of the major concerns, which may enter through the anode/cathode feed and may also originate from the system components (bipolar plates, sealing gaskets, coolants, etc.) [3]. Those impurities lead to a degradation in long-term PEFC performance, causing permanent damage on the membrane and catalyst layer structure [1,3-8].

There are significant challenges about storing and providing “pure” hydrogen as a fuel [9]. For this reason, hydrogen is commonly generated from the primary fuel sources, such as natural gas [10]. During their delivery to the fuel cell stations, these fuel sources may get contaminated with compressor oil or lubricants, originating from the pipeline and delivery infrastructure. Unfortunately, oil and lubricants may affect the fuel cell performance detrimentally, and they may not be easily removed from the fuel source [11-14].

Foreign cationic impurities within the polymer electrolyte membrane (PEM) are also known to affect the fuel cell performance and efficiency [3,8]. Metallic cations, such as $K^+$, $Na^+$, $Ca^{2+}$, $Ni^{2+}$, $Cu^{2+}$, $Cr^{3+}$, $Al^{3+}$ and $Fe^{3+}$, may originate either from the air feed in aerosol form or from the system components by corrosion or leaching [3-5]. Chemical and mechanical degradation of the polymer electrolyte membrane (PEM) and blockage of void regions in the porous components are the negative impacts of metallic cations during PEFC operation [1,3-6,15-23]. Certain efforts have been reported in literature to mitigate the poisoning effect of metallic cations [24-26]. Nevertheless, no studies are available for prevention of cationic impurities with the avoidance of material corrosion, and regular maintenance/cleaning of system equipment in fuel cells. Thus, hardware cleanliness can be a significant issue for fuel cell vehicles.

Regular maintenance of the fuel pipeline and metallic components is essential for the removal of oil/lubricant contamination and prevention of cationic impurities. The cleaning of this equipment can be performed by using commercially available cleansing agents, owing to their lower cost and availability. However, these cleansing agents may also be a source of contaminant due to their chemical composition. A proper chemical solution should be selected for the maintenance that does not cause a permanent negative effect on PEFC operation. The selected cleanser should have no effect on PEFC durability and performance, or its negative effect should be rapidly recoverable. Therefore, research on the effect of common cleaning agents on PEFCs is needed to determine an appropriate agent.

In order to address and solve the issues mentioned above, this chapter introduces the first experimental study on the effect of different cleansing agents on the PEFC

performance. Seven cleansers are selected among over sixty commercial agents through a systematic down-selection process. Next, impacts of these cleansing agents on the PEFC performance are assessed with screening tests (current-hold tests and diagnostic measurements). Following the screening tests, a proper cleansing agent, which has a minimum and recoverable effect on the performance is considered.

## 4.2 Experimental

### 4.2.1 Contaminant down-selection

Selection process is initiated with a list of all cleansing agents recommended by fuel cell providers (Fuel Cell & Hydrogen Energy Association) and the members of SAE Fuel Cell Standards Committee [27]. Over sixty cleanser products are considered, and they are classified into four groups according to their chemical compositions in the Safety Data Sheets (SDS): i) cations, ii) organics, iii) citrates and iv) amines. As a second criterion, the products need to be readily available nationally through retail stores along with lower costs. In the third stage, possible safety and toxicity issues are reviewed through NFPA 704 ratings [28] and SDS for each product. Finally, seven commercial cleansing agents are selected considering the availability of the test stations, required time to complete the experiments and analyze the post-test results. Selected samples are presented in Table 4.1 along with their chemical composition and solubility.

### 4.2.2 Fuel cell setup

Commercially available fuel cell components are used in all of the experiments. GORE$^{TM}$ PRIMEA$^{®}$ Membrane Electrode Assemblies (MEA) (W.L. Gore & Associates Inc., Elkton, MD) are used as the catalyst coated membranes (CCMs) with anode and cathode catalyst

layers of 0.4 mg/cm$^2$ Pt loading each. The active area of the CCM is 25 cm$^2$. Anode/cathode aluminum end plates, gold-plated current collectors and bipolar plates are purchased from Fuel Cell Technologies (Albuquerque, NM). Bipolar plates have single and triple serpentine flow channels at anode and cathode sides, respectively. In addition, Freudenberg H2315-C4 (Freudenberg FCCT SE& Co. KG, Germany) gas diffusion layers (GDLs) are considered as anode and cathode GDLs in the PEFC assemblies.

The schematic view of the experimental setup, which is the same setup as our prior work [29], can be seen in Figure 4.1. Polarization curves and the performance data at current-hold tests are measured by the fuel cell test stand (Teledyne MEDUSA RD, TELEDYNE Energy Systems, Inc., Hunt Valley, MD) by using the electronic load box Scribner 890CL (Scribner Associates, Inc., Southern Pines, NC). Cross-over, cyclic voltammetry (CV) and electrochemical impedance spectroscopy (EIS) scans are measured with a potentiostat (Solartron 1287). The flow rate of the cleanser solution is controlled by an HPLC pump (Series III Pump, Scientific Systems Inc., State College, PA). After the cleanser solution passes through the HPLC, it is injected into the cathode inlet through a micro-flow nebulizer (ES-2005, PFA-400, Elemental Scientific Inc., Omaha, NE).

Ultra-high purity hydrogen ($H_2$) is supplied as the anode feed in all experiments. Cathode inlet is fed with ultra-zero grade air and ultra-high purity nitrogen ($N_2$) during current-hold tests and CV operations, respectively. Note that Airgas, Inc. is the provider of the gas cylinders.

### 4.2.3 Diagnostic measurements

Operating conditions for diagnostic tests are summarized in Table 4.2. Hydrogen ($H_2$) cross-over, cathode CV, polarization scans and electrochemical impedance spectroscopy (EIS) are measured before and after the contaminant exposure in order to accurately monitor the performance loss. $H_2$ cross-over analysis are performed with scan rate of 2 mV/s and linear sweep voltammetry from 0 V to 0.4 V. Cathode CV scans are operated at the same conditions as $H_2$ cross-over (Table 4.2), and applied within a range of 0-0.8 V at a scan rate of 20 mV/s.

Electrochemically active surface area (ECSA) in $cm^2$ Pt/g Pt is calculated after each cathode CV scan. In order to find the ECSA, charge density, required for atomic hydrogen desorption, ($Q_{des}$) is determined by integrating the area under the $H_2$ desorption peak. Next, the ECSA is found with the following relation [30]:

$$ECSA = \frac{Q_{des}}{m_{pt} Q_{des,ref}} \quad (1)$$

where $Q_{des,ref}$ is the reference charge density required to remove a monolayer of proton on Pt, and is equal to 0.21 $mC/cm^2$ Pt [30]. In addition, $m_{pt}$ is the Pt loading of the cathode catalyst layer, specified as 0.4 $mg/cm^2$.

Table 4.2 indicates that EIS measurements are performed at the same conditions as current-hold tests, which are the main stage of the cleanser testing. The details of experimental procedure and current-hold tests are to be presented in the next section.

### 4.2.4 Experimental procedure and current-hold tests

All of the cells are pre-conditioned to ensure the stable performance before the main stage of testing. Therefore, before the current-hold tests, cells are run at constant cell voltage, 0.6 V, for 12-16 hours at the cell temperature of 80 °C with 100/75% anode/cathode relative humidity (RH). During this testing, $H_2$ and air are provided with the stoichiometry of 2/2 into the anode and cathode inlets, respectively. When a stable performance is clearly observed in the data, pre-conditioning is stopped. At this point, polarization curve, cathode CV and $H_2$ cross-over measurements are recorded as the beginning of test (BOT) condition of the PEFC.

At the next stage, parameters are brought to the current-hold test settings (Table 4.2). Note the high cathode relative humidity, compared to the anode side, in our testing. This ensures that there is a concentration gradient of water from cathode to anode side to move the cleanser solution through the GDL. Higher cathode back pressure (15 psig vs 1.5 psig) is used with the same idea. Additionally, high flow rate of air (1.66 slpm air in Table 4.2) could make the transport of solution carrying the cleanser easier. In this research, our main goal is to detect the performance degradation of the cell due to the cleanser injection into the cathode inlet. In this way, high flow rate of hydrogen (1.75 slpm) at the anode side could minimize the anode polarization losses.

Current-hold experiments are initiated with the baseline condition for 24-48 hours, i.e. no contamination into the fuel cell. Beginning of test (BOT) EIS measurements are performed at the start of baseline test. When the cell performance is seen to be stable at the end of baseline, EIS is again measured to observe the condition just before the contaminant injection. Next, cleanser solution is fed through the nebulizer into the cathode inlet, and

the cell performance and internal resistance are monitored for 24 hours or until the cell voltage drops below the critical level, ~0.3 V. EIS measurement is repeated at this point as the end of the contamination. Then, the injection of contaminant is stopped and recovery is performed at constant current for 24 hours or until a stable fuel cell performance is reached.

Volume percentage of cleanser solutions can be seen in Table 4.3. As noted in this table, samples F and G are injected into the cathode inlet in pure form without mixing with DI water. This condition leads to different cathode relative humidities (recall Table 4.2) during the injection of samples F and G, which are separately calculated and given in the next section.

When the current-hold tests are completed, polarization, EIS, $H_2$ cross-over and cathode CV scans are again applied and recorded as the end of test (EOT) results for each PEFC. Operating conditions for the complete testing procedure are given in Table 4.2.

### 4.3 Results and discussion

Testing results of the cells are summarized in Table 4.3. It is evident that the cells tested with samples F and G are the only ones which can be fully recovered after the exposure of the contaminants. There is no sodium or potassium compound in samples F and G, in contrast to other cleansing agents as in Table 4.1. Hence, one of the reasons in the performance decrease by the contamination of samples A-E may be due to the replacement of protons in PEM with sodium ($Na^+$) and potassium ($K^+$) ions and mass transport losses [19-21,23]. It can also be discussed that $K^+$ and $Na^+$ ions may easily enter the membrane

in our experiments since most cleansers act also as a surfactant [26,31] (see Table 4.1), enabling the transport of the cleaning solution across the hydrophobic gas diffusion media.

In the following sections, screening tests (diagnostics and current-hold measurements) are shown to describe the effects of seven samples on the fuel cell performance. Results from the screening tests for each sample are compared and discussed in detail. It is concluded that sample G, as in Figure 4.2, has the most reasonable and fully recoverable performance loss.

### 4.3.1 Current-hold tests

Figure 4.3 shows the time history profiles during the current-hold tests for the cleansers. In these figures, sections I, II and III represent the baseline, contaminant injection and recovery, respectively. In section I, 130 µl/min of DI water (samples A-E) or only dry air (samples F and G) is fed into the cathode inlet for 24-48 h. Once the performance is stabilized, baseline test is stopped. Next, 130 µl/min of cleanser solution (samples A-E) or 10-250 µl/min of pure cleansers (samples F and G) is injected from the HPLC pump through the nebulizer in section II. Following the exposure of the cleanser, 130 µl/min of DI water or only dry air is again fed into the cathode inlet for 24 h (section III) to recover the performance loss.

In Figure 4.3, similar behavior in cell voltage and resistance can be observed during the injection of samples A and B (section II). Both samples cause a steady decrease in cell voltage, along with an increase in resistance. The important difference is the higher voltage decay rate due to sample A (smp A) exposure than the one during the injection of sample

B (smp B) (Table 4.3). Figure 4.3 also demonstrates that performance losses due to samples A and B can only be partially recovered in section III.

Note that 5% and 0.5% solutions of sample C are, in order, named as C(1) and C(2). Figure 4.3 shows that 5% solution of sample C, C(1), leads to very high cell voltage decay rate (Table 4.3) in section II, such that C(1) could only be exposed for 20 min. Hence, the contaminant injection is immediately turned off, and the performance is almost fully recovered with DI water, as in Figure 4.3 (smp C(1)). Then, a new cell is tested with 0.5 % solution of the same sample, C(2), to examine the long-term effect. As sample C(2) is injected into the cathode inlet for 24 h (section II), voltage decay rate decreases with time (Table 4.3). Meanwhile, cell resistance is raised from 75 to 100 mΩ.cm2 due to the contamination in Figure 4.3 (smp C(2)). There is, however, only partial recovery in cell voltage and no recovery in resistance in section III after the injection of 0.5% sample C. Section III for smp C(2) also reveals a small but continuous decay in cell voltage, even if the DI water is further supplied into the cathode inlet. Therefore, a permanent damage is discovered in the PEFC with 24 h exposure of 0.5% solution of sample C.

Time history profiles for the cells exposed to samples D and E are also given in Figure 4.3. While sample D is injected as a 5% cleanser solution in Figure 4.3 (smp D), 0.5% cleanser solution (Table 4.3) is determined for sample E (smp E in Figure 4.3) since it has a high percentage of sodium content (Table 4.1). Hence, lower concentration of sample E is considered to ensure 24 h exposure of this sample. As seen from Figure 4.3, injections of samples D and E (sections II) reveal similar results to each other. These samples cause, respectively, 0.12 and 0.095 V of voltage drops with the decay rates of 3.5 and 2.2 mV/h after 24 h of contamination (Table 4.3). Then, neither cell voltage nor

resistance can be restored with DI water supply in sections III of smp D and E in Figure 4.3. Thus, 24 h exposures of samples D and E have irreversible effects on cell performance.

As discussed previously with Tables 4.1-4.3, samples F and G are not mixed with water, in contrast are directly injected into the cathode inlet during contamination. Additionally, it has been confirmed with calculations that flow rate of these samples through nebulizer does not significantly affect the cathode relative humidity. The main plan is, first, to test the effect of samples F and G at a flow rate of 10 µL/min. Next, target flow rate would be set to a larger value depending upon the performance loss and recovery. Figure 4.3 (smp F) presents the current-hold test results for sample F. Cathode relative humidities are indicated in this figure for the cases of dry air (section I), 10 µl/min of sample F (section II), and dry air (section III) through nebulizer into cathode inlet. Figure 4.3 shows that 10 µL/min of sample F causes a negative step change of ~70 mV in voltage at the beginning of section II. Then, cell voltage stabilizes at around 0.5 V with some fluctuations after 15 h of exposure. Interestingly, Figure 4.3 shows no appreciable increase of resistance with the sample F cleanser. Once the cleanser injection is stopped, cell voltage is immediately restored back to the base value (section III for smp F). Higher flow rates of sample F are not investigated since 10 µL/min of this sample causes a significant voltage loss during contamination.

Figure 4.3 also presents the screening of sample G (smp G) on the time history profile. Sections I, II and III for smp G holds, respectively, for dry air, 250 µl/min of sample G, and dry air through the nebulizer into cathode inlet. Note that 10 and 50 µl/min of sample G are also tested before switching to 250 µl/min, however they are not included in the current figure since 10 and 50 µl/min of this sample caused less severe performance

decrease than the test of sample F. It is seen from Figure 4.3 that sample G also leads to a step decrease (~0.22 V) in voltage, similar to the sample F testing (smp F). Voltage is reduced to 0.4 V in first 20 min, and then remains constant in section II of smp G (Figure 4.3). Besides, cell resistance is almost not affected by sample G injection. Finally, cell performance is fully recovered in section III (smp G in Figure 4.3).

### 4.3.2 Polarization (I-V) tests

Figure 4.4 shows the results of polarization scans at the beginning of test (BOT) and the end of test (EOT) for samples of cleansers A-E. It is obvious that samples A, B, D and E exhibit detrimental effects on the I-V scan of the cells. At EOT results of these samples, current density cannot exceed 1 A/cm$^2$ on I-V curves to maintain the cell voltage more than 0.35 V. Interestingly, 5 % sample C, C(1), seems to produce very small negative outcome after 20 min exposure at the current-hold test (Figure 4.3). However, Figure 4.4 shows that 0.5% of this sample (smp C(2)) with 24 h of exposure leads to a considerable degradation on polarization curve. Polarization scans for samples F and G, not shown here, do not reveal any change or decrease between BOT and EOT. In other words, impacts of samples F and G are completely removed at EOT.

### 4.3.3 Electrochemical impedance spectroscopy (EIS) measurements

EIS is measured at 1 A/cm$^2$ during current-hold tests, and its results are given in Figure 4.5. Impedance spectra are collected at BOT, beginning of contamination, end of contamination and EOT. Note that left intercept of the data points along x-axis is the ohmic resistance, while the right intercept is the sum of ohmic, ionic and mass transfer resistance. Both ohmic and diffusion resistances are increased due to the long-term (>7 hours)

exposures of samples A-E, as demonstrated in Figure 4.5 (smp A, B, C(2), D and E). Increased resistance can only be partially mitigated for sample A. Besides, resistance remains unchanged after the recovery period for samples B and C (2). Furthermore, Figure 4.5 (smp D and E) shows that situation gets even worse for samples D and E with larger resistances after the injection of DI water at EOT. While the impedance increase after the 24 hours exposure of 0.5% sample C (smp C(2)) could not be reversed, 20 min. (5%) exposure of the same sample, C(1) in Figure 4.5, indicated more than 90% recovery with DI water flush. On the other hand, EIS scans for samples F and G reveal complete recovery at EOT. EIS results for sample F are not included in Figure 4.5 since no effect on impedance is seen even during the contamination period. Neither sample F nor G has an impact on ohmic resistance. The main difference between samples F and G is that while sample G has a distinct effect on mass transfer resistance at the end of contamination (smp G in Figure 4.5), no explicit effect can be observed for sample F. This difference may be attributed to the lower flow rate of sample F during the exposure. Hence, 10 µl/min of 2-propanol has no clear effect on resistance on the impedance spectrum. The significant performance decrease for smp F in Figure 4.3, which is discussed earlier, may be due to the reduction of ECSA during the direct injection of this sample.

### 4.3.4 Cathode cyclic voltammetry (CV) results

Discussion of screening tests are concluded with cathode CV scans at BOT and EOT for samples (smp) A, B, C(2) and D in Figure 4.6. Samples C(1), and E-G are not considered in the current figure since there is no obvious impact on the cathode CVs between BOT and EOT for these samples. ECSA values for each sample test are also listed in Table 4.4. It is indicated that injection of 5% sample C with 20 min exposure, C(1), and samples E-G

lead to less than 20% ECSA loss on the PEFC. In contrast, cleansers A, B, C(2) and D provoke a noticeable decrease on the active area, in addition to their negative effects on the cell voltage and resistance. Surprisingly, sample E causes no appreciable decrease in ECSA (~10% in Table 4.4), although the results above (Figures 4.3-4.5) clearly demonstrate that exposure of cleanser E promotes a permanent decay on the fuel cell performance. It is also given in Table 4.4 that 14.9 and 10.3% ECSA losses have been detected at the end of the tests for the recoverable samples F and G, respectively. Both ECSA losses due to samples F and G can be considered to be allowable compared to the results for cleansers A-D.

## 4.4 Conclusion

Impacts of seven different cleansing agents on the PEFC performance have been discussed during their injection into the cathode inlet. Current-hold tests are performed for each cleansing agent, and performance losses at the end of contaminant injection are attempted to be recovered for each sample of cleanser. The major points as a result of the current study can be organized as follows:

i. Screening tests indicate that effects of samples F (2-propanol) and G (naphtha) on the fuel cell performance are fully recoverable at the tested concentrations and compositions. It should be noted that naphtha has a widely varying composition for different commercial brands.

ii. Although the performance loss due to sample F (2-propanol) exposure can be fully recovered, it causes a detrimental decrease in cell voltage even with 10 µl/min flow rate. Moreover, our earlier studies [26] indicate that 5-15% 2-propanol leads to the breakage of the bond between the catalyst layer and membrane; therefore resulting in irrecoverable performance loss during long-term operation of a PEFC.

iii. Sample G, or naphtha, is considered to be the best candidate among the seven cleansers at the end of the screening tests since PEFC can still operate at ~0.4V at constant current (1 A/cm$^2$) even with 250 µl/min of sample G contamination.

iv. There is a step change (decrease) in cell voltage during the injections of samples F and G. This condition may be due to either the change in the local hydrophobicity of GDL or the localized cooling during vaporization.

An important point, which should be considered thoroughly, is the sulfur content (up to 1.5%) in sample G (naphtha), according to certain suppliers [32]. Sulfur is known to be a critical impurity, which causes a serious performance loss in PEFCs [5]. For this reason, it should be justified that the naphtha to be used for the system cleaning is completely free of sulfur.

The present study is intended to serve as a basis for the selection of the proper cleanser to be used for fuel pipeline and hardware maintenance/cleaning in the fuel cell industry. The most promising candidate (sample G) in our study is mainly composed of alkanes and cycloalkanes (see Table 4.1 and Refs. [32,34]). In addition, sample F which also exhibits fully recoverable effect basically includes isopropanol in its chemical composition. In contrast, all other samples include some metallic components, e.g. sodium and potassium, and their results show non-recoverable performance degradation after the exposure. Next chapter is going to provide the in-depth analysis of sample G (naphtha) exposure and its impacts on PEFC performance.

## 4.5 References

[1] Wu J, Yuan XZ, Martin JJ, Wang H, Zhang J, Shen J, et al. A review of PEM fuel cell durability: degradation mechanisms and mitigation strategies. J Power Sources 2008;184(1):104-19.

[2] EG&G technical Services, Inc. Fuel cell handbook. 7th ed. U.S. Department of Energy; November 2004.

[3] Zamel N, Li X. Effect of contaminants on polymer electrolyte membrane fuel cells. Progress in Energy and Combustion Science 2011;37(3):292-329.

[4] Collier A, Wang H, Yuan XZ, Zhang J, Wilkinson DP. Degradation of polymer electrolyte membranes. Int J Hydrogen Energy 2006;31(13):1838-54.

[5] Cheng X, Shi Z, Glass N, Zhang L, Zhang J, Song D, et al. A review of PEM hydrogen fuel cell contamination: Impacts, mechanisms, and mitigation. J Power Sources 2007;165(2):739-56.

[6] Borup R, Meyers J, Pivovar B, Kim YS, Mukundan R, Garland N, et al. Scientific aspects of polymer electrolyte fuel cell durability and degradation. Chem Rev 2007;107(10):3904-51.

[7] St-Pierre J. PEMFC contamination model: competitive adsorption followed by an electrochemical reaction. J Electrochem Soc 2009;156(3):B291-300.

[8] U.S. Department of Energy. Fuel cell technologies office multi-year research, development and demonstration plan, section 3.4 - fuel cells. June 2016. http://energy.gov/sites/prod/files/2016/06/f32/fcto_myrdd_fuel_cells_0.pdf.

[9] Aceves SM, Berry GD. Thermodynamics of insulated pressure vessels for vehicular hydrogen storage. Journal of Energy Resources Technology 1998;120(2):137-42.

[10] Brown LF. A comparative study of fuels for on-board hydrogen production for fuel-cell-powered automobiles. Int J Hydrogen Energy 2001;26(4):381-97.

[11] USDRIVE. Hydrogen delivery technical team roadmap. June 2013. http://www1.eere.energy.gov/vehiclesandfuels/pdfs/program/hdtt_roadmap_june2013.pdf.

[12] Melaina MW, Antonia O, Penev M. Blending hydrogen into natural gas pipeline networks: a review of key issues. US: National Renewable Energy Laboratory; March 2013. http://www.nrel.gov/docs/fy13osti/51995.pdf.

[13] Ainscough C, Randolph K, Sutherland E. 2014 hydrogen transmission and distribution workshop summary report. US: National Renewable Energy Laboratory; July 2014. http://energy.gov/sites/prod/files/2014/07/f17/fcto_2014_h2_trans_dist_wkshp_summary_report.pdf.

[14] U.S. Department of Energy. Fuel cell technologies office multi-year research, development and demonstration plan, section 3.2 - hydrogen delivery. August 2015. http://energy.gov/sites/prod/files/2015/08/f25/fcto_myrdd_delivery.pdf.

[15] Wang H, Turner JA. The influence of metal ions on the conductivity of Nafion 112 in polymer electrolyte membrane fuel cell. J Power Sources 2008;183(2):576-80.

[16] Kienitz B, Baskaran H, Zawodzinski T. Modeling the steady-state effects of cationic contamination on polymer electrolyte membranes. Electrochim Acta 2009;54(6):1671-9.

[17] Serincan MF, Pasaogullari U, Molter T. Modeling the cation transport in an operating polymer electrolyte fuel cell (PEFC). Int J Hydrogen Energy 2010;35(11):5539-51.

[18] Li H, Tsay K, Wang H, Shen J, Wu S, Zhang J, et al. Durability of PEM fuel cell cathode in the presence of $Fe^{3+}$ and $Al^{3+}$. J Power Sources 2010;195(24):8089-93.

[19] Kienitz B, Pivovar B, Zawodzinski T, Garzon FH. Cationic contamination effects on polymer electrolyte membrane fuel cell performance. J Electrochem Soc 2011;158(9):B1175-83.

[20] Jia R, Han B, Levi K, Hasegawa T, Ye J, Dauskardt RH. Effect of cation contamination and hydrated pressure loading on the mechanical properties of proton exchange membranes. J Power Sources 2011;196(8):3803-9.

[21] Uddin MA, Pasaogullari U. Computational modeling of foreign cation contamination in PEFCs. J Electrochem Soc 2014;161(10):F1081-8.

[22] Wang X, Qi J, Ozdemir O, Uddin A, Pasaogullari U, Bonville LJ, et al. $Ca^{2+}$ as an air impurity in polymer electrolyte membrane fuel cells. J Electrochem Soc 2014;161(10):F1006-14.

[23] Qi J, Wang X, Ozdemir MO, Uddin MA, Bonville L, Pasaogullari U, et al. Effect of cationic contaminants on polymer electrolyte fuel cell performance. J Power Sources 2015;286:18-24.

[24] Trogadas P, Parrondo J, Ramani V. Degradation mitigation in polymer electrolyte membranes using cerium oxide as a regenerative free-radical scavenger. Electrochemical and Solid-State Letters 2008;11(7):B113-6.

[25] Coms FD, Liu H, Owejan JE. Mitigation of perfluorosulfonic acid membrane chemical degradation using cerium and manganese ions. ECS Transactions 2008;16(2):1735-47.

[26] Park J, Uddin MA, Ganesan S, Pasaogullari U, Bonville LJ, Molter T. Effects on wetting agents in cationic contamination and mitigation in PEFCs. ECS Transactions 2015;66(24):91-100.

[27] Collins WP, St-Pierre J, Rocheleau R. Monthly technical progress report to Hawaii National Energy Institute (HNEI), University of Hawaii for the project title "The Effect of Airborne Contaminants on Fuel Cell Performance and Durability". June 2015.

[28] NFPA. 704, 2012, Standard System for the Identification of the Hazards of Materials for Emergency Response (2012 edition). National Fire Protection Association; 2012.

[29] Uddin MA, Wang X, Qi J, Ozdemir MO, Pasaogullari U, Bonville L, et al. Effect of chloride on PEFCs in presence of various cations. J Electrochem Soc 2015;162(4):F373-9.

[30] Fournier J, Faubert G, Tilquin J, Guay D, Dodelet J. High-performance, low Pt content catalysts for the electroreduction of oxygen in polymer-electrolyte fuel cells. J Electrochem Soc 1997;144(1):145-54.

[31] Uddin MA, Park J, Bonville L, Pasaogullari U. Effect of hydrophobicity of gas diffusion layer in calcium cation contamination in polymer electrolyte fuel cells. Int J Hydrogen Energy 2016;41(33):14909-16.

[32] TESORO Naphtha; SDS No. 888100004450 [Online]; Tesoro Refining & Marketing Co.: San Antonio, TX, October 6, 2014; https://tsocorpsite.files.wordpress.com/2015/07/naphtha.pdf.

[33] Crown Industrial Series VM&P Naphtha; SDS No. CX.VMT [Online]; Packaging Service Co., Inc.: Pearland, TX, September 2, 2015; http://www.packserv.com/products/crown/.

[34] CITGO Special Naphtholite 66/3; SDS No. 19021 [Online]; CITGO Petroleum Co.: Lemont, IL, November 1, 2017; http://www.docs.citgo.com/msds_pi/19021.pdf.

**Table 4.1** List of the cleansers and their components.

| Sample Name | Chemical Components and weight percentage (if available) | | Soluble in Water? (Y/N) |
|---|---|---|---|
| A | Water | ≥78 | Y |
| | Triethanolamine | ≤10 | |
| | Ethoxylated Alcohol | ≤5 | |
| | Propylene Glycol Butyl Ether | ≤5 | |
| | Tetrapotassium Pyrophosphate | ≤1 | |
| | Potassium Silicate | ≤1 | |
| | Colorant | ≤1 | |
| B | Water, Sodium Lauryl Sulfate, Sodium Laureth Sulfate, PPG-26, PEG-8 Propylheptyl Ether, Phenoxyethanol, Methylisothiazolinone, Lauramine oxide, Sodium Chloride, Fragrance | | Y |
| C | Citrus Terpenes | 1-5 | Y |
| | Dipropylene Glycol Monobutyl Ether; Glycol Ether DPnB; 1-(2-butoxy-1-methylethoxy) propan-2-ol | 1-5 | |
| | Diethylene Glycol Butyl Ether; 2-(2-butoxyethoxy)-ethanol | 1-5 | |
| | Fatty Acids, tall oil | 1-5 | |
| | Sulfonic Acids, C14-16-alkane hydroxyl and C14-16 alkane, sodium salts | 1-5 | |
| | Alcohols, C12-16, ethoxylated | 1-5 | |
| D | Benzene Sulfonic Acid, C10-16-alkyl Derivs | 1-5 | Y |
| | Sodium Metasilicate (disodium salt) | 1-5 | |
| E | Tetrasodium ETDA | 0-5 | Y |
| | Sodium Metasilicate | 0-5 | |
| F | 2-Propanol | >99 | Y |
| G[a] | Light Aliphatic and Low Boiling Point Naphtha | 100 | N |

[a] Taken from the safety data sheet (SDS) of the tested sample's supplier [33]. More detailed composition of sample G (hydrocarbons, alkanes and cycloalkanes) can also be obtained from the SDSs of other suppliers [32,34].

**Table 4.2** Operating parameters for the screening tests and diagnostic measurements.

| **Current-hold Test and Electrochemical Impedance Spectroscopy (EIS) Scans** | |
|---|---|
| Cell temperature | 80 °C |
| Anode Relative Humidity | 25% |
| Cathode Relative Humidity | 125% (samples A-E)<br>104-105% (sample F)<br>102-105% (sample G) |
| Anode Back Pressure | 1.5 psig |
| Cathode Back Pressure | 15 psig |
| Anode Flow Rate | 1.75 l/min $H_2$ |
| Cathode Flow Rate | 1.66 l/min Air (0.4 l/min from nebulizer) |
| Current Density | 1 A/cm$^2$ |
| DI Water and Cleanser Flow Rate from HPLC Pump (samples A-E) [a] | 130 µl/min |
| DI Water Flow Rate from HPLC Pump (samples F and G) [b] | - (no DI water) |
| Cleanser Flow Rate from HPLC Pump (samples F and G) [c] | 10, 50 and 250 µl/min |
| **Polarization Scans** | |
| Cell temperature | 80 °C |
| Anode Relative Humidity | 100% |
| Cathode Relative Humidity | 75% |
| Anode Back Pressure | 0 psig |
| Cathode Back Pressure | 0 psig |
| Anode Stoichiometry | 2 (Minimum flow rate; 0.2 l/min $H_2$) |
| Cathode Stoichiometry | 2 (Minimum flow rate; 0.2 l/min Air) |
| **$H_2$ Cross-over Tests & Cyclic Voltammetry (CV) Scans** | |
| Cell temperature | 25 °C |
| Anode Relative Humidity | 100% |
| Cathode Relative Humidity | 100% |
| Anode Back Pressure | 0 psig |
| Cathode Back Pressure | 0 psig |
| Anode Flow Rate | 0.25 l/min $H_2$ |
| Cathode Flow Rate | 0.25 l/min $N_2$ |

[a] DI water is injected during baseline and recovery, cleanser is provided during contamination.

[b] No DI water is injected from HPLC pump through nebulizer during baseline and recovery tests of samples F and G, with which cathode relative humidity is ensured to be close to the one at contamination stage.

[c] Samples F and G are initially tested with 10 µl/min flow rate of cleanser through nebulizer. Next, flow rate may be increased to 50 and 250 µl/min depending on the severity of performance loss.

**Table 4.3** Performance summary of the cells exposed to the cleanser injection.

| Sample | Volume Percentage of Cleanser in DI Water Solution (%) | Duration of exposure | Decay Rate during exposure | Total Voltage Drop during Exposure (mV) | Recoverable? (Y/N/Partial) |
|---|---|---|---|---|---|
| A | 5 | 7 hours (high decay rate observed) | **34 mV/h** | 238 | Partial |
| B | 5 | 24 hours | **13.8 mV/h** | 330 | Partial |
| C(1)[a] | 5 | 20 minutes (high decay rate observed) | **1380 mV/h** | 460 | Partial |
| C(2)[a] | 0.5 | 24 hours | **19.8 mV/h** in first 5 hours<br>**1.01 mV/h** in last 5 hours<br>(decreasing decay rate) | 137 | Partial |
| D | 5 | 24 hours | **48 mV/h**, sharp drop in first 50 min.<br>**3.52 mV/h** in next 23 hours<br>(constant decay rate) | 122 | N |
| E | 0.5 | 24 hours | **9.18 mV/h** in first 5 hours<br>**2.20 mV/h** in last 5 hours<br>(decreasing decay rate) | 95 | N |
| F[b] | Pure (-) | 24 hours | **4200 mV/h**, sharp drop in first 1 min.<br>**~2.33 mV/h** in next 15 hours<br>(then performance is stabilized) | 105 | Y |
| G[b] | Insoluble (-) | 24 hours | **651 mV/h**, sharp drop, in first 20 min.<br>(then performance is stabilized) | 217 | Y |

[a] C(1) and C(2) are representing sample C with the difference of only volume percentage of cleanser solution.

[b] Owing to their recoverable impact on fuel cell and since sample G is insoluble in water, samples F and G are directly (purely) injected into the cathode inlet without mixing with water to observe the maximum effect during exposure.

**Table 4.4** Percentage ECSA loss of the cells exposed to the cleanser injection.

| **SAMPLE** | **Percentage ECSA loss (%) from BOT to EOT** |
|---|---|
| A | 34.4 |
| B | 37.4 |
| C (1) (20 min. exposure of 5% sample C in DI water) | 15.5 |
| C (2) (24 h exposure of 0.5% sample C in DI water) | 28.3 |
| D | 21.0 |
| E | 9.8 |
| F | 14.9 |
| G | 10.3 |

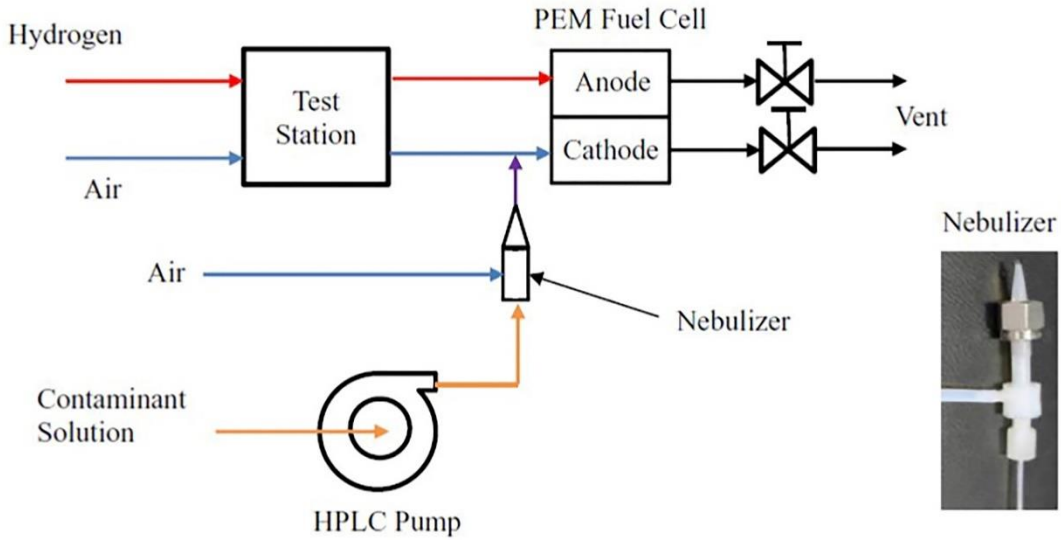


**Fig. 4.1** Schematic view of the experimental setup and a representative photo for the nebulizer used in the current-hold tests. Figure is taken from our prior work, Ref. [29]. (Note: Contaminant solution is the cleanser solution)

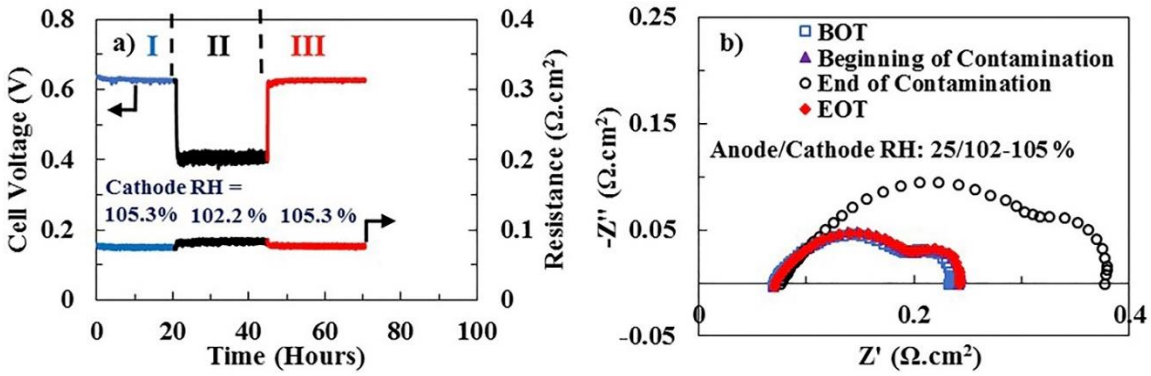


**Fig. 4.2 a)** Cell performance curve (current-hold test) and **b)** EIS data for sample G. Anode and cathode relative humidities (RH) are indicated in the figure. Other operating parameters are listed in Table 4.2. Note: Polarization and cathode CV tests are not shown since there is no change between BOT and EOT. (I: baseline, II: contaminant injection, III: recovery).

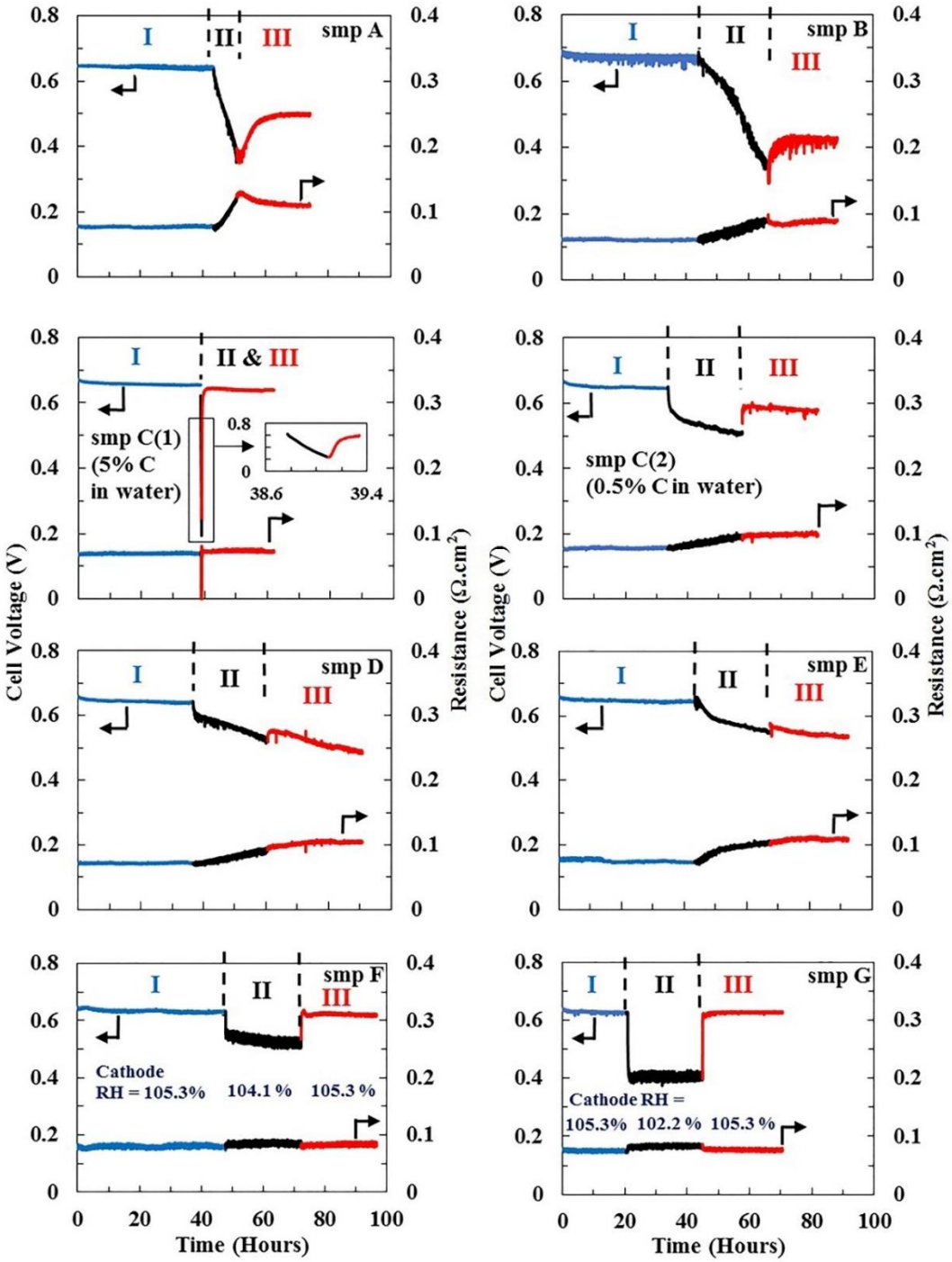


**Fig. 4.3** Cell performance during current-hold tests. Note: Section II for sample C(1) (5% sample C exposure) is only for 20 min due to very fast performance decrease. Cathode relative humidities (RH) for the tests of samples F and G are indicated in the figure. Other operating parameters are listed in Table 4.2. (I: baseline, II: contaminant injection, III: recovery, smp: sample).

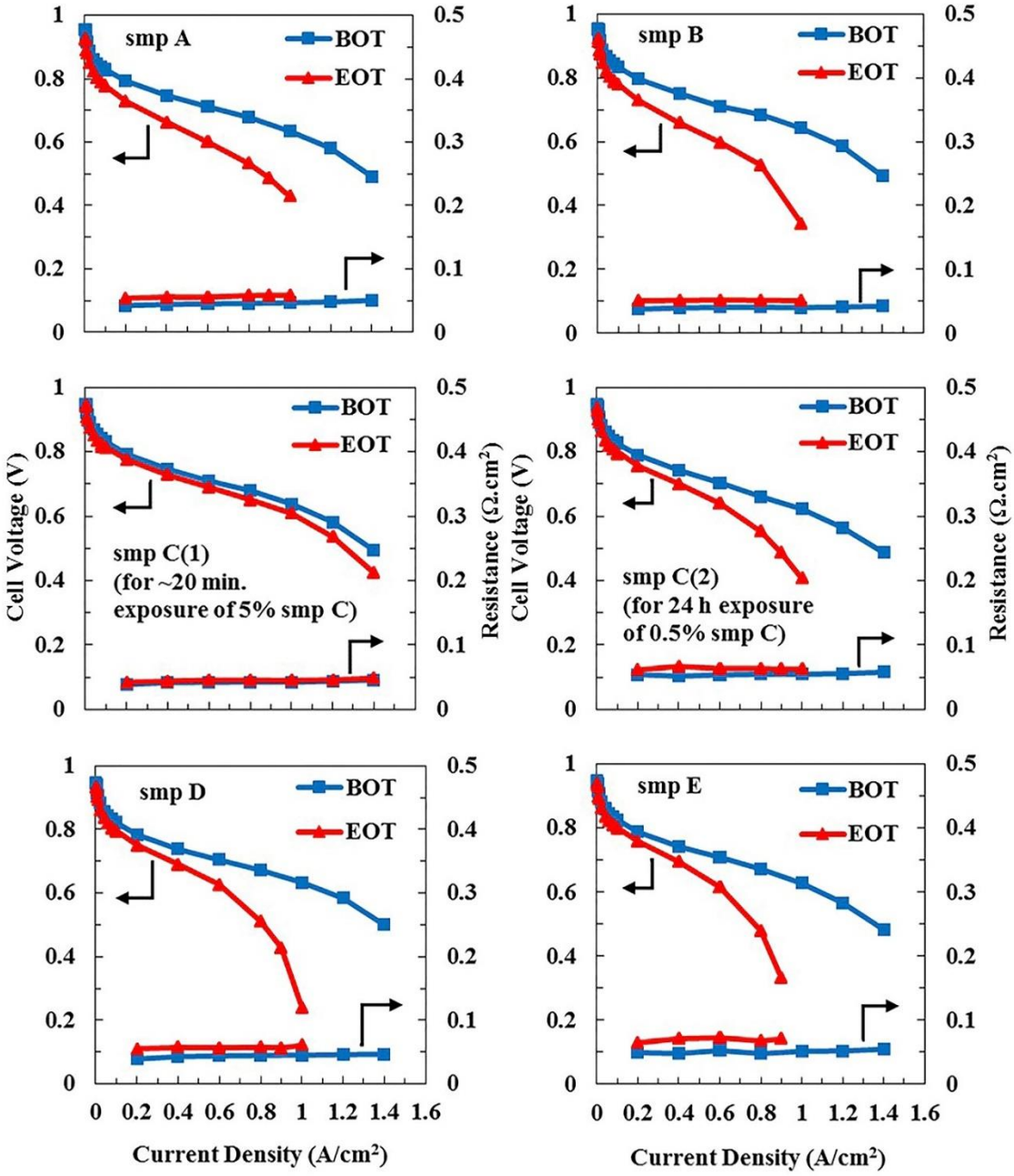


**Fig. 4.4** Polarization curves at BOT and EOT. Operating parameters are listed in Table 4.2. (smp: sample).

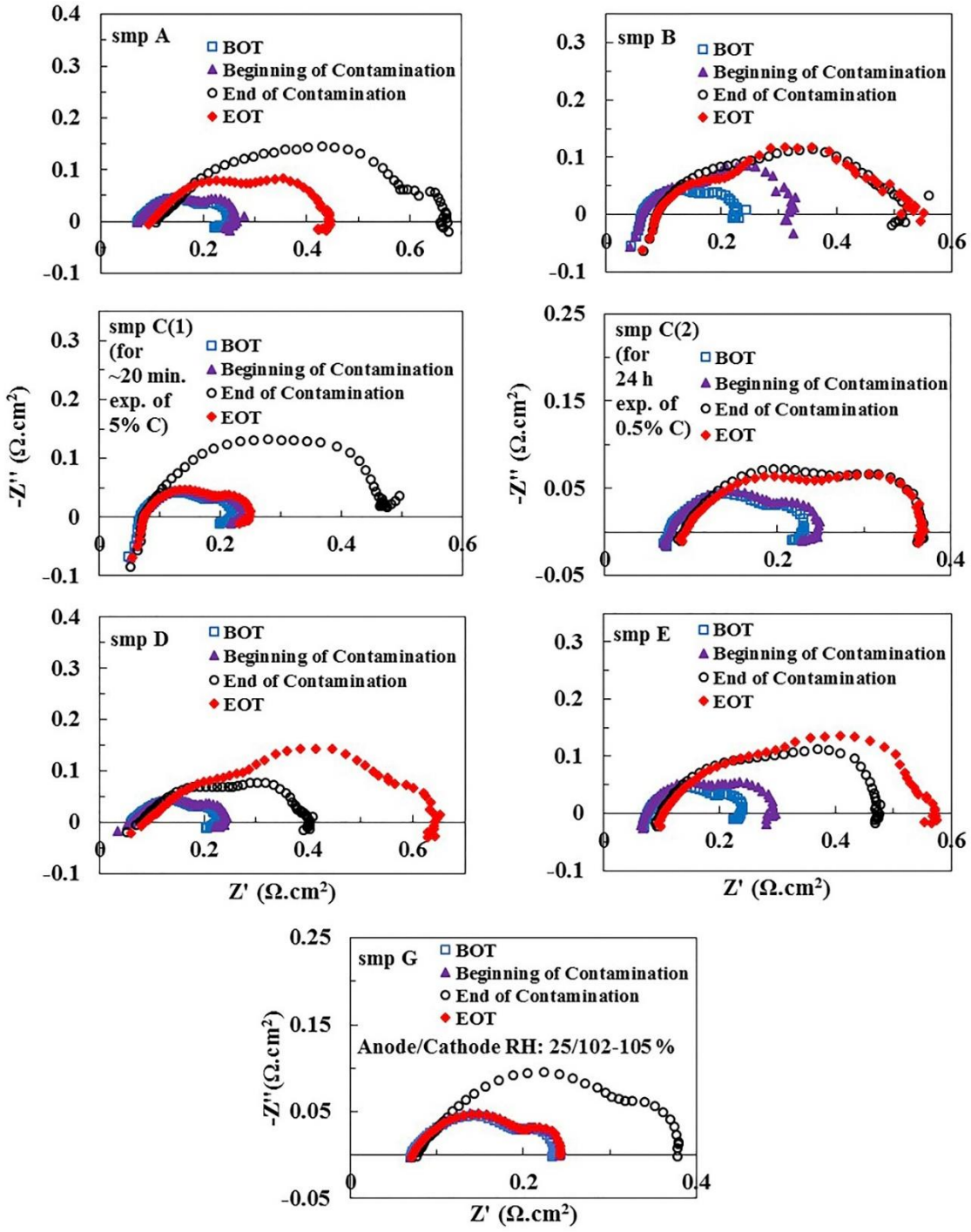


**Fig. 4.5** EIS measured at BOT, beginning of contamination, end of contamination and EOT. Anode and cathode relative humidities (RH) for sample G testing are indicated in the figure. Other operating parameters are listed in Table 4.2. (smp: sample).

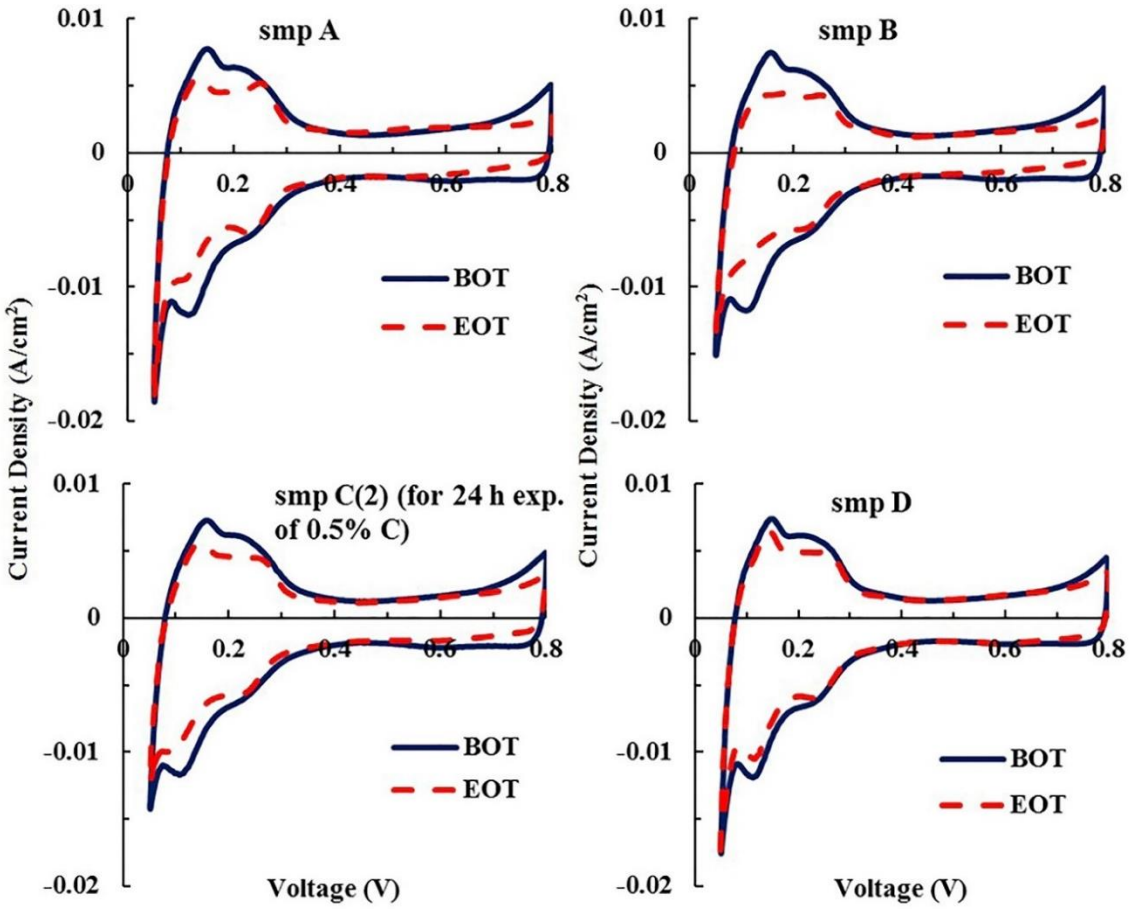


**Fig. 4.6** Cathode CVs at BOT and EOT. Operating parameters are listed in Table 4.2. (smp: sample).

# Chapter 5 Detailed Investigation of Naphtha as a Selected Cleansing Agent and the Study on its Effects on PEFC Performance

## 5.1 Introduction

Once the screening for each sample is completed in Chapter 4, it is concluded that sample G, or known as naphtha (recall Table 4.1), is the best candidate for the maintenance of fuel cells with minimal impact on the performance. Selected cleansing agent in Chapter 4 is to be analyzed and discussed in detailed. Chapter 5 describes the detailed investigation of sample G exposure with equivalent circuit model fitted for the EIS data before and after the contamination, and at EOT. Additionally, binary gas diffusion analysis of the cathode gas and cathode CV results with and without sample G are presented.

## 5.2 Results and discussion

### 5.2.1 Detailed analysis on EIS data with equivalent electrical circuit model

Electrochemical impedance spectra are measured at “Beginning of Contamination”, “End of Contamination” and EOT for sample G, as previously presented in Figure 4.5. To obtain detailed information on the individual losses (solution, charge transfer, and mass transfer) that are prone to performance decrease, simple electrical circuits are fitted to the experimental data. Figures 5.1a and 5.1b are, respectively, the electrochemical spectra and the associated electrical circuit model for the cell, which is used for sample G testing. In Figure 5.1b, the conventional double-layer capacitance is replaced by a constant phase element (CPE), Q, because the capacitance caused by the double-layer charging is distributed along the length of the pores in the porous electrode [1,2].

The diameter of the kinetic loop (high-frequency semicircle) in Figure 5.1a, $R_{ct}$, is a measure of the charge transfer resistance of the oxygen reduction reaction (ORR). This characteristic single loop is a fairly good indicator of the properties of the cathode, particularly the catalyst layer. At the "Beginning of Contamination" and EOT, the first semi-circle loop is fitted with simple Randles circuit ($Q_{ad} = R_{ad} \approx 0$ in Figure 5.1b) [3-5], where the CPE ($Q_{ct}$) and resistance ($R_{ct}$) due to charge transfer are in parallel. For the curve fit of the "End of Contamination", additional resistance ($R_{ad}$) and CPE ($Q_{ad}$) are connected in series with $R_{ct}$ [6,7]. The resistance $R_{ad}$ could originate from the temporary adsorption of naphtha, or a reaction intermediate on the active Pt sites [6,7]. The first semicircle or the total polarization loss is drastically enhanced at the end of sample G exposure (Figure 5.1a), probably due to the addition of resistance ($R_{ad}$) and the adsorption of contaminant. Once the sample G injection is stopped, the EIS spectrum at EOT fits with "Beginning of Contamination" results. Therefore, this study confirms the effect of naphtha on ORR is temporary and recoverable. Besides, since the naphtha is made up of simple hydrocarbons (Table 4.1), some intermediate products may form during the ORR process and attach to the Pt surface.

The second semicircle (Figure 5.1a) is originated from the mass transfer effect in all cases. The mass transfer regions for both "Beginning of Contamination" and EOT are close enough. However, the second semi-circle develops significantly at the end of sample G injection, which indicates sample G not only affects the ORR reaction sites by adsorption, it also blocks the reactant transport.

In order to verify the existence of adsorption terms, $Q_{ad}$ and $R_{ad}$, Figure 5.2 gives the comparison of fitted curves for the "End of Contamination" EIS using the circuit in

Figure 5.1b with and without neglecting the adsorption. The dashed line in Figure 5.2 represents the circuit without the adsorption effect ($Q_{ad}$ = $R_{ad}$ = 0), and demonstrates a rough curve fit with almost a single semicircle. However, the continuous line, which considers the adsorption resistance ($R_{ad}$) and CPE ($Q_{ad}$), reveals a better fitting to EIS data. In other words, inclusion of the adsorption terms approximates a curve fit of two semicircles (continuous line in Figure 5.2), providing a better explanation to EIS data at the end of naphtha injection.

Figure 5.3 shows the fitted curves for the EIS data of sample G testing with the given equivalent circuit model in Figure 5.1b. The high-frequency intercept ($R_{ohm}$) of the impedance arc on the real axis represents the total ohmic resistance of the cell, which is the sum of the contributions from contact resistances between components and ohmic resistances of the cell components such as the membrane, catalyst layer, gas diffusion layer, and bipolar plates. The low-frequency intercept on the real axis indicates the sum of total ohmic ($R_{ohm}$), charge transfer ($R_{ct}$), mass transfer ($R_{mt}$), and adsorption ($R_{ad}$) resistances. It is shown in Figure 5.3 that there is a slight increase in ohmic resistance value at the "End of Contamination" which could be due to temporary block of electron transport at the catalyst layer by adsorption of organic moiety. There is also an increase in the right intercept of the impedance curve at the end of sample G exposure due to an increase in mass transfer and adsorption resistances in the same figure. On the other hand, both "Beginning of Contamination" and EOT do not show any significant difference at high- and low-frequency intercepts since the performance loss due to sample G (naphtha) is fully recoverable.

The resulting parameters, resistances and CPEs, for the fitted curves (Figure 5.3) are presented in Table 5.1. As evidenced from this table, the injection of sample G (naphtha) causes the inclusion of the adsorption resistance, $R_{ad}$ = ~0.1 $\Omega.cm^2$, a noticeable increase (almost twice) in mass transfer resistance ($R_{mt}$), and a slight rise in ohmic resistance ($R_{ohm}$). It should be recalled that the jump in ohmic resistance from ~70 to ~80 $m\Omega.cm^2$ is already observed just after the sample G exposure during the screening results (Figure 4.3). In contrast to its impact on other resistances, contamination with sample G does not alter the charge transfer resistance ($R_{ct}$). This proves our earlier discussion that total polarization losses (Figure 5.1a) are increased as a result of the adsorption of sample G (naphtha), or an intermediate product (from the surface reactions of its components), on the Pt sites. Meanwhile, there is not a significant change in parameters between "Beginning of Contamination" and EOT except a very limited growth in mass transfer resistance ($R_{mt}$).

### 5.2.2 Study for the effect of naphtha on cathode mass transport

#### *5.2.2.1 Effect on limiting current density*

To further investigate and verify the degradation in reactant transport during contamination of sample G, a separate polarization (I-V) study is performed, shown in Figure 5.4. The basic aim of the experiments in this figure is to be able to determine the limiting current density of the PEFC with and without sample G exposure through nebulizer. In this case, operating conditions, which are presented in Figure 5.4, are different from the regular procedure for the polarization scans in Table 4.2. Current-hold test settings are mainly used for this case since the maximum current density is desired to be high enough to detect the decrease in limiting current density due to sample G more clearly. Meanwhile, limiting

current density can be easily observed, if there is a sharp increase in mass transfer losses after a certain point of cell current density on the I-V curve. For this reason, 10% oxygen (in $N_2$) is used as the cathode gas instead of the air, keeping the stoichiometry at the cathode side same as the current-hold test settings (~4 at 1 A/cm$^2$) with the total cathode gas flow rate of 3.35 slpm (Figure 5.4). A severe drop in limiting current density (from 1.3 to 0.55 A/cm$^2$) can be seen with the sample G (naphtha) exposure in Figure 5.4. This condition supports the increase in mass transfer resistance (Table 5.1) for EIS curve at the end of contamination, and also the vital effect of sample G (naphtha) on the cathode mass transport.

#### *5.2.2.2 Analytical study for the evaluation of binary gas diffusion coefficient at cathode with and without naphtha*

The negative influence of sample G (naphtha) on the species transport can also be assessed by a simple binary diffusion analysis for the cathode gas. The main idea is to calculate the binary diffusion coefficient of oxygen ($O_2$) with nitrogen ($N_2$) ($D_{O_2\text{-}N_2}$), and also with sample G, or naphtha, ($D_{O_2\text{-Naphtha}}$). To begin with, the equation (1) gives the diffusion coefficients, $D_{AB}$ in cm$^2$/s, for the binary and nonpolar gas mixtures (A and B) [8,9]:

$$D_{AB} = 2.745.10^{-4}\left(\frac{T}{\sqrt{T_{c,A}T_{c,B}}}\right)^{1.823}\frac{(P_{c,A}P_{c,B})^{1/3}(T_{c,A}T_{c,B})^{5/12}\left(\frac{1}{M_A}+\frac{1}{M_B}\right)^{1/2}}{P_{cathode}} \quad (1)$$

where $T_c$ and $P_c$ are the critical temperature (K) and pressure (atm) of the species, M is the molecular weight (g/mol), T is the temperature (K) and $P_{cathode}$ is the total pressure (atm). Moreover, critical properties and molecular weight of naphtha can be evaluated with the following empirical relation [10,11]:

$$X = a[\exp(bT_b + cS + dT_bS)](T_b)^e S^f \quad (2)$$

where X is a physical property, $T_b$ is the average boiling point (K), and S is the specific gravity (at 16 °C) of naphtha. In equation (2), a-f are the constant parameters for different physical properties to be calculated. Critical properties and molecular weights for $O_2$, $N_2$ and sample G are summarized in Table 5.2. It should be mentioned that specific gravity at 20 °C is used in equation (2), instead of 16 °C, since the thermo-physical properties of naphtha differ for various brands and are difficult to obtain accurately.

Diffusion coefficients for the gas pairs $O_2$-$N_2$ and $O_2$-Naphtha are calculated to be $D_{O_2\text{-}N_2}$=0.139 $cm^2/s$ and $D_{O_2\text{-Naphtha}}$ = 0.0461 $cm^2/s$ from equation (1), respectively. Although there is not an exact data for the diffusion coefficient of oxygen with naphtha in literature, calculated value for oxygen with nitrogen, $D_{O_2\text{-}N_2}$, can be verified since it is close to the existing data from earlier studies [12-16]. Thus, our calculations clearly indicate that sample G exposure decreases the mass transport of reactants by 3 times, which also explains the decrease in limiting current density (Figure 5.4) and increase in mass transfer resistance at the "End of Contamination" (Table 5.1).

### 5.2.3 Comparison of cathode CV results with and without naphtha injection

It is previously hypothesized (Figure 5.3 and Table 5.1) that sample G covers the available Pt sites by adsorption and leads to an additional resistance ($R_{ad}$) during EIS measurements. To further prove this phenomenon, cathode CV scan including the effect of sample G without recovery is investigated, as a post-test in Figure 5.5. In this test, cathode CV is first measured before sample G exposure, which is the CV result at "EOT". Next, sample G is injected through nebulizer into the cathode inlet for 2 hours with anode/cathode flow rates

of 0.6/0.6 slpm $H_2/N_2$ (0.4 slpm $N_2$ from nebulizer) and fully humidified anode/cathode (no back pressure) at 25 °C. At the end of 2 hours, sample G injection is stopped and cathode CV is again measured with the operating conditions given in Figure 5.5. There is ~27% decrease in ECSA after the sample G injection, such that it verifies the contaminant adsorption onto Pt sites at the end of sample G exposure. Subsequently, cell is recovered with $H_2$/air anode/cathode flow at current-hold test condition (Table 4.2). Following the recovery, cathode ECSA returns back to the base value (EOT) before exposure, as in Figure 5.5.

## 5.3 Conclusion

Detailed analytical analysis for sample G (naphtha) exposure on EIS measurements and binary gas diffusion is performed after the earlier discussion of screening tests in Chapter 4. It is proven that adsorption of sample G, or an intermediate product due to the surface reactions of its components, onto the Pt sites and the increase in mass transfer resistance are the principle reasons for the performance decrease during the contaminant injection.

## 5.4 References

[1] Wang X, Hsing I, Leng Y, Yue P. Model interpretation of electrochemical impedance spectroscopy and polarization behavior of $H_2$/CO mixture oxidation in polymer electrolyte fuel cells. Electrochim Acta 2001;46(28):4397-405.

[2] Ciureanu M, Roberge R. Electrochemical impedance study of PEM fuel cells. Experimental diagnostics and modeling of air cathodes. The Journal of Physical Chemistry B 2001;105(17):3531-9.

[3] Yuan XZ, Song C, Wang H, Zhang JJ. Electrochemical impedance spectroscopy in PEM fuel cells: fundamentals and applications. London: Springer Science & Business Media; 2010.

[4] Zhang W, Maruta T, Shironita S, Umeda M. Anode and cathode degradation in a PEFC single cell investigated by electrochemical impedance spectroscopy. Electrochim Acta 2014;131:245-9.

[5] Zhang W, Shironita S, Umeda M. Electrochemical impedance spectroscopy investigation on the ionomer degradation modeling of the anode using a porous microelectrode. Int J Hydrogen Energy 2016;41(15):6526-33.

[6] Jiang R, Kunz HR, Fenton JM. Electrochemical oxidation of $H_2$ and $H_2$/CO mixtures in higher temperature ($T_{cell}$ > 100°C) proton exchange membrane fuel cells: electrochemical impedance spectroscopy. J Electrochem Soc 2005;152(7):A1329-40.

[7] Nakajima H, Konomi T, Kitahara T, Tachibana H. Electrochemical impedance parameters for the diagnosis of a polymer electrolyte fuel cell poisoned by carbon monoxide in reformed hydrogen fuel. Journal of Fuel Cell Science and Technology 2008;5(4):041013.

[8] Chen NH, Othmer DF. New generalized equation for gas diffusion coefficient. J Chem Eng Data 1962;7(1):37-41.

[9] Bird RB, Stewart WE, Lightfoot EN. Transport phenomena. 2nd ed. New York: Wiley; 2002.

[10] Riazi MR, Daubert TE. Characterization parameters for petroleum fractions. Ind Eng Chem Res 1987;26:755-9.

[11] Riazi MR. Characterization and properties of petroleum fractions. 1st ed. ASTM International; 2005.

[12] Wilke CR. Diffusional properties of multicomponent gases. Chem Eng Prog 1950;46(2):95-104.

[13] Welty JR, Wicks CE, Rorrer GL, Wilson RE. Fundamentals of momentum, heat, and mass transfer. 5th ed. New York: Wiley; 2009.

[14] Um S, Wang CY. Three-dimensional analysis of transport and electrochemical reactions in polymer electrolyte fuel cells. J Power Sources 2004;125(1):40-51.

[15] Wang Y, Wang C. Transient analysis of polymer electrolyte fuel cells. Electrochim Acta 2005;50(6):1307-15.

[16] Ju H, Meng H, Wang C. A single-phase, non-isothermal model for PEM fuel cells. Int J Heat Mass Transfer 2005;48(7):1303-15.

[17] Crown Industrial Series VM&P Naphtha; SDS No. CX.VMT [Online]; Packaging Service Co., Inc.: Pearland, TX, September 2, 2015; http://www.packserv.com/products/crown/.

**Table 5.1** Parameters from the results of fitting EIS data for sample G (naphtha) test.

| Name of the Circuit Element | Beginning of Contamination | End of Contamination | EOT |
|---|---|---|---|
| $R_{ohm}$, ohmic resistance ($\Omega.cm^2$) | 0.0725 | 0.08045 | 0.0725 |
| $R_{ct}$, charge transfer resistance ($\Omega.cm^2$) | 0.13175 | 0.13175 | 0.13175 |
| $R_{mt}$, mass transfer resistance ($\Omega.cm^2$) | 0.04045 | 0.07135 | 0.041125 |
| $R_{ad}$, adsorption resistance due to Naphtha injection ($\Omega.cm^2$) | ~0 | 0.099075 | ~0 |
| $Q_{ct}$, CPE due to the charge transfer ($F/cm^2.s^{(a_{ct}-1)}$) | 0.04264 | 0.018464 | 0.04336 |
| $a_{ct}$ [a] | 0.7756 | 0.8491 | 0.7681 |
| $Q_{mt}$, CPE due to the mass transfer ($F/cm^2.s^{(a_{mt}-1)}$) | 0.8404 | 0.4336 | 0.7792 |
| $a_{mt}$ [a] | 1 | 1 | 1 |
| $Q_{ad}$, CPE due to the adsorption of contaminant ($F/cm^2.s^{(a_{ad}-1)}$) | ~0 | 0.014632 | ~0 |
| $a_{ad}$ [a] | N/A | 1 | N/A |

[a] "a = 1" means the CPE is a pure (ideal) capacitor, and "a = 0" means it is a pure inductor ($0 < a < 1$).

**Table 5.2** Critical properties and molecular weights for the cathode gas components.

| Component Name | Critical Temperature (K) | Critical pressure (atm) | Molecular weight (g/mol) |
|---|---|---|---|
| $O_2$ | 154.6 | 49.8 | 32 |
| $N_2$ | 126.2 | 33.6 | 28.01 |
| Sample G [a] | 589.7 [b] | 26.6 [c] | 118 [d] |

[a] Average boiling point and specific gravity at 20 °C for sample G, naphtha, are $T_b$ = ~405.65 K and S = 0.752 from Ref [17].

[b] Calculated from eq. (2); the constants are a = 9.5233, b = $-9.314.10^{-4}$, c = -0.544442, d = $6.4791.10^{-4}$, e = 0.81067, f = 0.53691 [10,11].

[c] From eq. (2); a = $3.1958.10^{5}$, b = $-8.505.10^{-3}$, c = -4.8014, d = $5.749.10^{-3}$, e = -0.4844, f = 4.0846 [10,11].

[d] From eq. (2); a = 1032.1, b = $9.78.10^{-4}$, c = -9.53384, d = $2.0.10^{-3}$, e = 0.97476, f = 6.51274 [10,11].

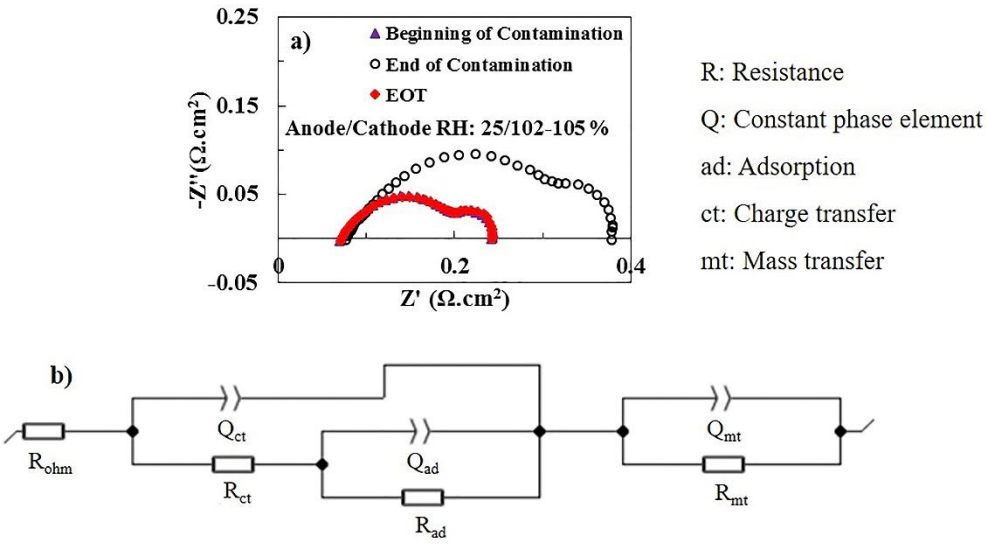


**Fig. 5.1 a)** EIS data and **b)** associated electrical circuit model for sample G testing. Resistance, R, and CPE, Q, due to the contaminant adsorption is zero for the "Beginning of Contamination" and EOT (i.e., $R_{ad} = Q_{ad} \approx 0$ without sample G, or naphtha, injection).

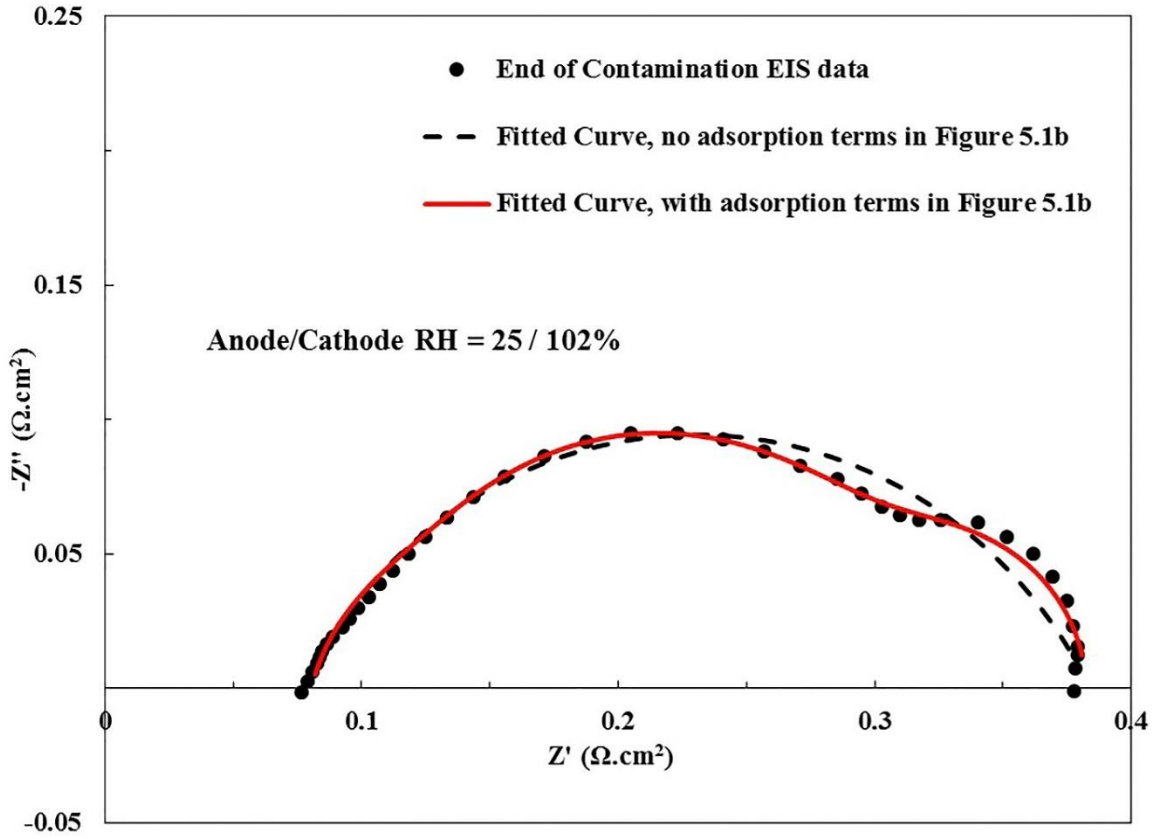


**Fig. 5.2** Comparison of curve fitting results during sample G (naphtha) injection using the circuit in Figure 5.1b with (continuous line) and without (dashed line) including the adsorption resistance ($R_{ad}$) and CPE ($Q_{ad}$).

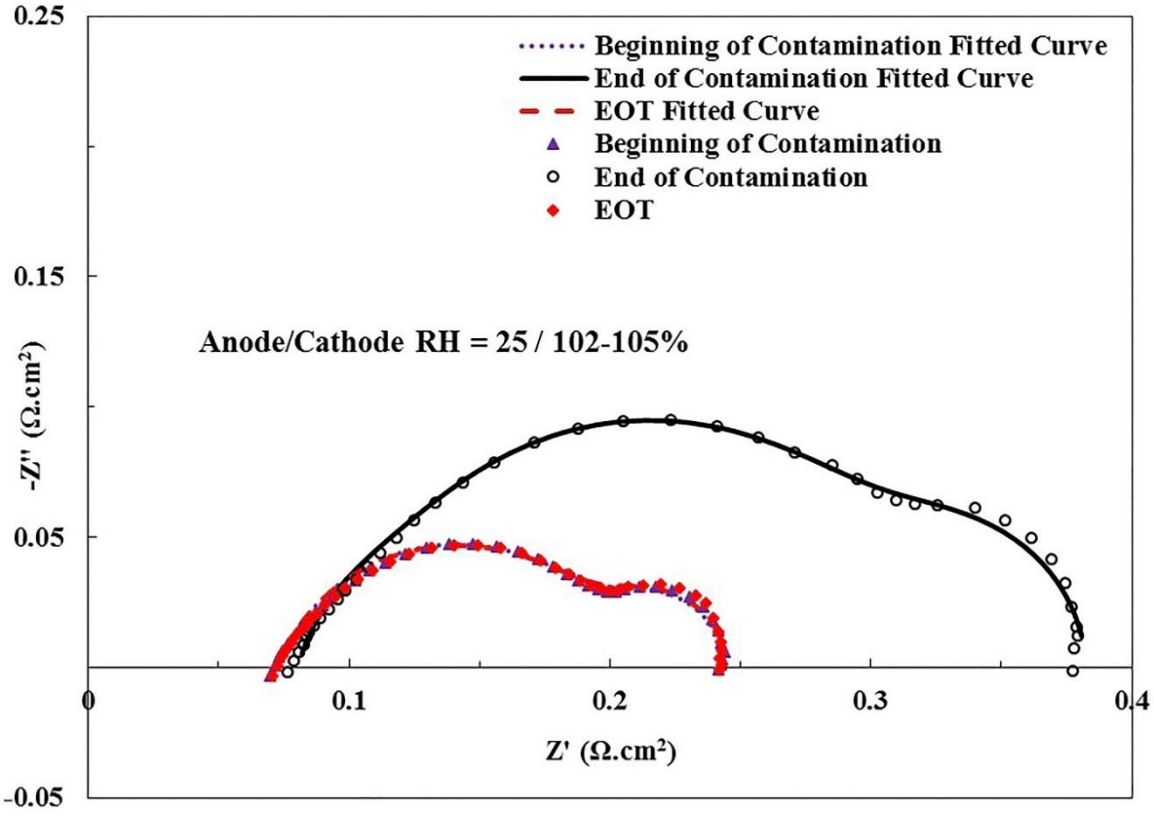


**Fig. 5.3** EIS data and fitted curves at "Beginning of Contamination", "End of Contamination" (during naphtha injection) and EOT for sample G (naphtha) testing. Electrical circuit model in Figure 5.1b is used for the evaluation of fitted curves.

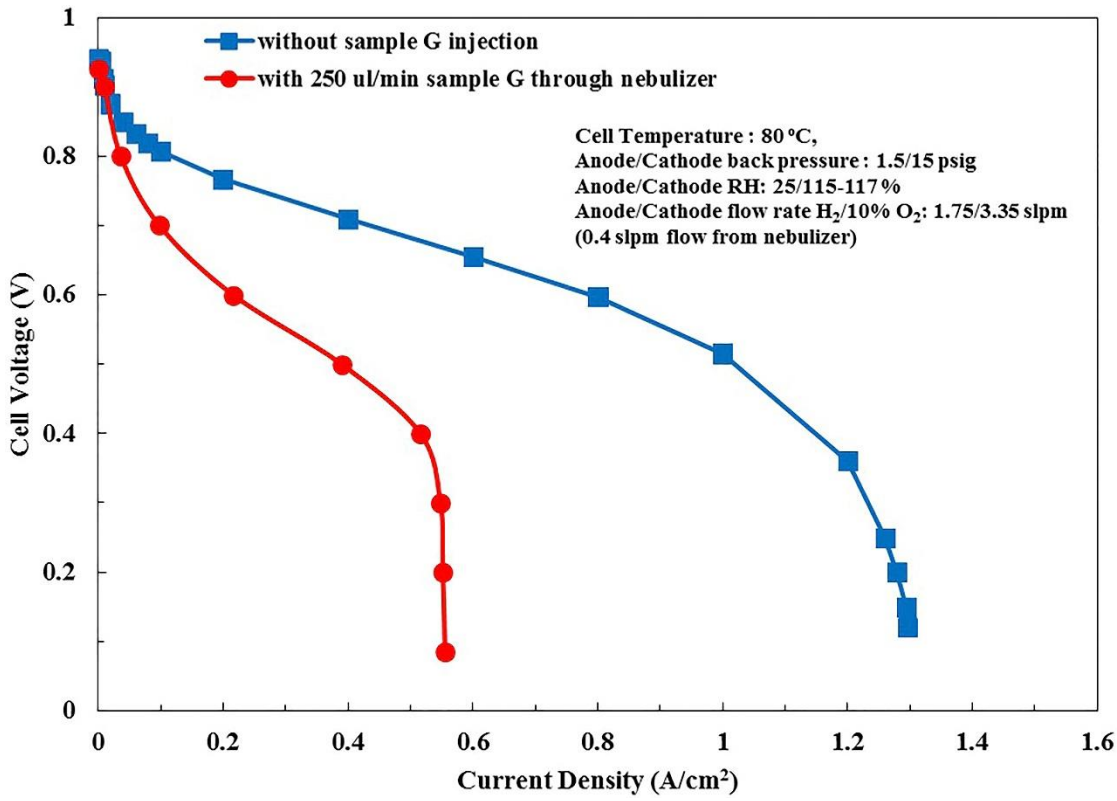


**Fig. 5.4** Polarization study to observe the limiting current density with and without contamination of sample G (naphtha). Measurements are performed with $H_2$ and 10% $O_2$ (in $O_2/N_2$) through anode and cathode inlets, respectively. Operating parameters are given in the figure.

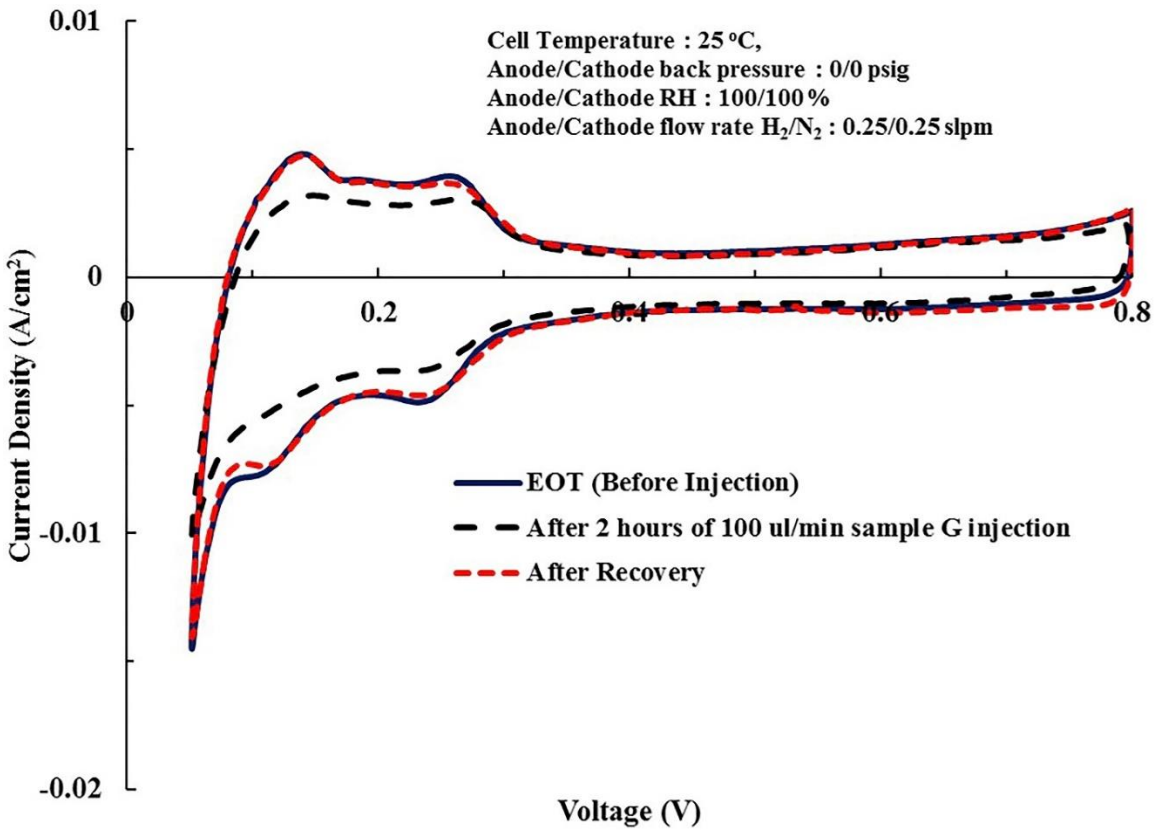


**Fig. 5.5** Cathode CV curves to determine the effect of sample G (naphtha) injection over electrochemical active surface area (ECSA). Operating parameters are given in the figure. Note: Sample G is injected into the cathode inlet with 0.6/0.6 slpm $H_2/N_2$ flow (with 0.4 slpm $N_2$ through the nebulizer) at the temperature, relative humidity (RH) and back pressure given in the figure. Recovery is performed at the current-hold testing condition

## Chapter 6 Conclusions and Future Work

Impurity effects and the strategies to remove or mitigate their negative impacts on polymer electrolyte fuel cell (PEFC) operation are explored in this research. Thus, durability and performance of fuel cell systems are believed to be improved with the detailed understanding about the poisoning and mitigation mechanisms of impurities.

Carbon monoxide (CO), as a common contaminant at PEFC anode, is studied in chapters 2 and 3. A one-dimensional transient model is developed to demonstrate the CO poisoning in Pt catalyst layer (CL), considering the surface coverages of adsorbed hydrogen ($H_2$), CO and hydroxyl (OH). In this model, species adsorption/desorption on Pt surface and electro-oxidation of CO and OH are taken into account, along with the diffusion of $H_2$ and CO within the CL thickness. For the first time, emphasis is given on the OH kinetics in the CL and its influence on the $H_2$/CO adsorption and CO electro-oxidation. Note that formation of OH species on Pt surface is justified due to the high level of CO concentration (up to 0.1-1% CO), which leads to high overpotential.

Transient model for 1,000 ppm CO poisoning (in $H_2$) is presented on a Pt catalyst layer in chapter 2. Oscillatory behavior in surface coverages of adsorbed species and cell voltage is observed, and examined in detail across the length of the CL. The one-dimensional transient model has provided comprehensive understanding of the oscillations in cell voltage and surface coverages with taking into account species diffusion and adsorbed OH kinetics throughout the CL thickness. It is concluded that oscillations are driven by the adsorbed OH molecules on Pt sites, reaction of adsorbed CO with OH, and the species diffusion from gas diffusion layer (GDL) to membrane interface. Detailed and

better understanding of the performance oscillations due to CO poisoning benefits the fuel cell technology with more reliable operation.

In chapter 3, the proposed 1-D model in chapter 2 is applied for the investigation of 10,000 ppm CO (1% CO in $H_2$) contamination in Pt CL. Unlike the 1,000 ppm CO case, there are no oscillations during the poisoning stage of 1% CO. In the latter case (1%), CO concentration is high enough, therefore fast CO diffusion from GDL to membrane interface dominates over the CO electro-oxidation with adsorbed OH. Hence, only a limited amount of adsorbed CO can be oxidized on Pt sites, and overpotential cannot be reduced enough to trigger the oscillations. After the steady state condition is reached for 10,000 ppm CO poisoning, current density is pulsed from 0.1 to 2.5 A/cm$^2$ for 50 ms to enable oxidative removal of CO. With the current pulsing technique, 92% of the adsorbed CO is removed from the Pt surface, and 70% of the CL thickness is achieved to CO-free. Removal of high concentration CO in the fuel stream increases the durability and efficiency of a PEFC stack in a long-term operation. In addition, proposed technique, current pulsing, may be a cost-effective method and easy to be performed.

Chapters 4 and 5 are focused on the removal/prevention of organic and metallic contaminants, which originate from PEFC system or balance of plant (BOP) components. The proposed method in this study is to use commercially available cleansing agents (cleansers) for the regular maintenance/cleaning of fuel cell system and BOP components to prevent corrosion of components and the resulting contamination. However, it is believed that those available cleansers may also be a source of contaminant owing to their chemical composition. The study on the effect of the cleansing agents at PEFC cathode side would be useful for the selection of the proper cleanser. Therefore, it benefits the

researchers and the fuel cell industry with more effective maintenance of the components to achieve impurity-free mechanisms and power stations.

For this reason, several cleansers are down-selected in chapter 4. The possible effects of the selected samples on the PEFC performance are observed during their injection into the cathode inlet. It is also determined whether the negative impacts of the selected cleansers can be recovered in chapter 4. As a result of screening tests, one sample (naphtha) is considered as the best candidate with minimal and fully recoverable impact on the fuel cell performance.

In-depth investigation of the best sample of cleanser (from chapter 4), naphtha (sample G), is introduced in chapter 5. Measured electrochemical impedance spectra for this sample are explained with the fitted curves and equivalent electrical circuit models. In addition, an analysis on cathode side gas diffusion is performed. Limiting current densities of fuel cell and binary diffusion coefficients at cathode gas are determined with and without naphtha injection. Results from chapter 5 indicate that naphtha, or an intermediate product due to the surface reactions, are attached onto the catalyst surface and decrease the available Pt sites for oxygen reduction reaction (ORR). Moreover, mass transfer is also deteriorated at cathode gas during the naphtha injection.

As a recommended future work, CO modeling in chapters 2-3 can be further extended and modified to be used for low Pt-loaded catalyst layers (0.1 mg Pt/cm$^2$ Pt or lower) and Pt-alloy electrocatalysts. In this case, specific electro-active surface area ($A_v$), and reaction rate constants for CO electro-oxidation ($k_{co,ox}$) and OH adsorption ($k_{w,a}$ and $k_{w,d}$) in Table 2.1 need to be modified accordingly. Furthermore, 2-D and 3-D modeling domains may be considered in the future studies, including additional components such as

GDL and membrane. Therefore, more detailed results on oscillations due to $H_2$/CO mixtures, high concentration (0.1% or higher) CO poisoning in PEFCs and mitigation by current pulsing may be obtained.

Screening tests for the cleansing agents in chapter 4 may be repeated with the injection of the contaminants into the anode inlet, instead of the cathode. Hence, the possible effects of the cleansers on the fuel cell performance during their injection into the anode may be reported, and compared with the results in this thesis. Having the impacts of the samples of cleansers for their both anode and cathode side tests in the future, one can have a complete understanding about the screening of available cleansers in PEFC environment. Moreover, separate components of naphtha (Table 4.1) and their individual effects on fuel cell operation may be analyzed in order to extend the study in chapter 5. In this way, the possible intermediate products due to the surface reactions may also be investigated to clarify the cell voltage drop during naphtha injection.